Master's Thesis

Metallizitätstrends in Kugelsternhaufen

Metallicity Trends in Globular Clusters

prepared by

Merten Nikolay Dahlkemper

from Itzehoe

at the Institute for Astrophysics

Thesis period:	14th February 2019 until 14th August 2019
First Referee:	Prof. Dr. Stefan Dreizler
Second Referee:	Dr. Frederic V. Hessmann

Abstract

Der Integralfeldspektrograph MUSE am Very Large Telescope wird verwendet, um 25 Kugelsternhaufen auf Effekte von atomarer Diffuson zu untersuchen.

Hierzu werden mehrer Hundert bis zu einigen Tausend Sterne pro Haufen auf ihre Metallizität hin analysiert. In jedem der untersuchten Haufen werden Metallizitätstrends zwischen Hauptreihenabknickpunkt und rotem Riesenast und auch – für Haufen mit genügend Daten – auf der Hauptreihe gefunden.

Die Metallizitätstrends werden mit MIST Isochronen verglichen, welche die Ergebnisse des stellaren Entwicklungscodes MESA nutzen. Die beobachteten Trends befinden sich in guter Übereinstimmung mit den Modellen, wobei jedoch die Trends durch die Modelle systematisch überschätzt werden.

Stichwrter: Astrophysik, Kugelsternhaufen, stellare Entwicklung, atomare Diffusion, Integralfeldspektroskopie

Abstract

The integral field spectrograph MUSE at the Very Large Telescope is used in order to examine 25 Galactic globular clusters for effects of atomic diffusion.

In order to do so several hundred up to a few thousand stars per globular cluster are analysed for their metallicity. Trends in metallicity between the main sequence turn off and the red giant branch and – for clusters with sufficient data – also on the main sequence are found in every analysed cluster.

The metallicity trends are compared with MIST isochrones which make use of the stellar evolution code MESA. The observed trends are qualitatively in good agreement with the models, yet they are systematically overestimated.

Keywords: astrophysics, globular clusters, stellar evolution, atomic diffusion, integral field spectroscopy

Contents

Nomenclature

Abbreviations

Abbreviation	Meaning
ACS	Advanced Camera for Surveys
AD	atomic diffusion
AGB	asymptotic giant branch
CMD	color-magnitude diagram
GC	globular cluster
HB	horizontal branch
HST	Hubble Space Telescope
IFS	integral field spectroscopy
IFU	integral field unit
LTE	local thermodynamic equilibrium
MESA	Modules for Experiments in Stellar Astrophysics
MIST	MESA Isochrones and Stellar Tracks
MOS	multi-object spectroscopy
MS	main sequence
MSTO	main sequence turnoff
MUSE	Multi Unit Spectroscopic Explorer
NGC	New General Catalogue
NLTE	non-LTE
PSF	point-spread function
RGB	red giant branch
SGB	subgiant branch
SNR	signal-to-noise ratio
VLT	Very Large Telescope
WFC	Wide-Field Chanel

1. Introduction

The German astronomer and lens maker Joseph von Fraunhofer took the first spectrum of the Sun in the early 1800s. Since then astronomers measure properties of stars not only from the integrated intensity of light arriving at the Earth (photometrically) but also from its spectra (spectroscopically). About 50 years later, the physicist Kirchhoff and the chemist Bunsen connected the features of the spectrum with the chemical composition of the light source. The upcoming of atomic physics in the 1920s allowed astrophysicists to study stellar parameters in detail. Unfortunately, most of the light is scattered on the stellar surface, where all the information the light carries from inside the star get lost. If we want to get information about the interior of a star from its light, we need indirect methods like comparing light from similar stars and analysing the differences in spectra assuming that these differences are due to effects inside the star which alter the surface.

It has been known for more than 100 years that mixing processes inside stars play a significant role by altering the surface abundances of stars (Chapman, 1917). In 1991 anomalies in the abundance of single elements in a variety of stars were explained by effects of *atomic diffusion* (Tutukov, 1991). In 1998, abundance anomalies were investigated for the first time in star clusters (King et al., 1998; Boesgaard et al., 1998), which are a great laboratory for exploring stellar interiors and stellar evolution. This is not only because of their sheer size of about 10^4 - 10^6 stars, but also because it is assumed that all stars of one cluster formed from the same molecular cloud and therefore all the differences in evolutionary states are only due to their initial masses (Carroll and Ostlie, 2014, p. 520 f.).

For a long time, individual stars in globular clusters could only be analysed spectroscopically in their outskirts since the stellar density inside clusters is very high, so in a conventional long-slit spectrograph spectra of several stars are blended. This has changed with *multi-object spectroscopy (MOS)* and *integral field spectroscopy (IFS)* which combine high spatial resolution with spectral information.

The scope of this work is to use data from the IFS *MUSE* (Bacon et al., 2010),

which is a second generation instrument on the *Very Large Telescope (VLT)* at Paranal Observatory in Chile, in order to investigate 25 Galactic globular clusters for trends in their surface metallicity and infer the effectiveness of atomic diffusion inside stars with a variety of initial metallicities.

This thesis is structured as follows. In this Chapter I give some motivation why to study globular clusters and why MUSE is the ideal instrument for this purpose. In Chapter 2 I give some theoretical foundations of mixing processes inside a star and how they are numerically treated. In Chapter 3 I give an overview of the studies of abundance trends in star clusters which have been carried out in the past. In Chapter 4 I explain the data and methods used in this work, the results are shown in Chapter 5. Chapter 6 concludes this work by discussing the results and giving an outlook of what can be done on this field in the future. Chapter 7 summarizes this work. In the appendices A and B additional plots and tables are shown.

1.1. Globular clusters

Globular clusters (GCs) are collections of ten thousands up to a million stars which are believed to have been formed in a single molecular cloud about 10 to 13 billion years ago. In the Milky Way there are currently 157 globular clusters known (Harris, 2010),

Globular clusters are interesting objects to study for several reasons. First, due to the high star density stellar encounters are more likely which result in exotic objects. Second, globular clusters are old and believed to be chemically very homogeneous objects which is why they can reveal information about the evolution of the universe as well as of single stellar evolution, although the assumption of chemical homogeneity has been challenged in recent years with the discovery of multiple populations in globular clusters (Ashman and Zepf, 2008; Freeman and Norris, 1981).

1.1.1. The Color-Magnitude Diagram of a Globular Cluster

A common tool to study globular clusters photometrically is the color-magnitude diagram (CMD), which is the observational analogon to the Hertzsprung-Russel diagram, where color is the equivalence of effective temperature and magnitude is the equivalence of luminosity.

Since GCs contain stars of similar age and chemical composition, they only differ

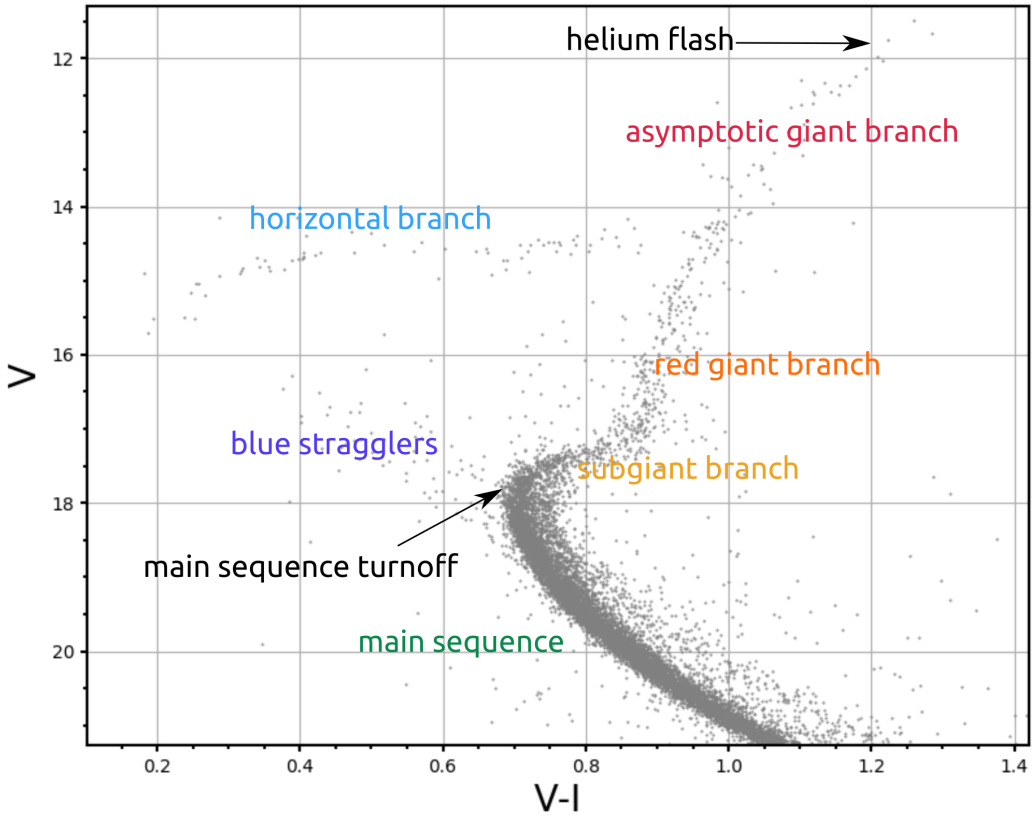

Figure 1.1.: Color-magnitude diagram of the globular cluster NGC 3201 with annotations of the different parts which are described in this section. The x-axis denotes the the differences of two photometric filters, which is the measure for color. The y-axis denotes the relative magnitude in a specific photometric filter. The meaning of the letters V and I is explained in Sectin 4.1.3. The data are taken from the HUGS survey (Fontana et al., 2014).

in mass. Stars of higher mass evolve faster than lower-mass stars, therefore higher-mass stars are in a later evolution stage. Therefore thee evolution stages are visible in the CMD of a GC and CMDs of different GCs look qualitatively the same. An example of such a CMD is shown in Figure 1.1.

For the largest part of their life a star is on an evolution stage called *main sequence* (MS) which spans from the cool and faint to the hot and bright corner of the CMD. During this evolution stage, nuclear fusion of hydrogen to helium in the core takes place. Since the mass range of the stars inside a globular cluster is continuous, the precise shape of the main sequence in the CMD is determined mainly by the stars' chemical composition. Most clusters have a very clearly defined main sequence which means that the stars all have basically the same chemical composition.

The most prominent feature in the CMD of a globular cluster is the *main sequence turnoff* (MSTO) where a star leaves the main sequence. The MSTO is very sharp in most of the clusters which is another hint for most of the stars having the same age. Therefore the location of the MSTO is a very good measure for the age of the cluster. As the MSTO of globular clusters occurs at much fainter positions than in stellar populations in the solar neighbourhood it can be safely assumed that globular clusters are very old objects. Indeed, age estimates are between 10 and 15 billion years. The first estimates even challenged cosmological age estimations of the universe since the GC ages exceeded the age of the universe.

After a star leaves the main sequence because it ran out of hydrogen inside the core the fusion process inside the shell sets in. During this phase the star produces more energy than while core burning on the main sequence, therefore the luminosity of the star rises while the envelope of the star expands and the effective temperature decreases and therefore the star moves towards redder colors in the CMD. This phase of decreasing temperature is called *subgiant branch* (SGB). While the temperature decreases, the energy transport gets more efficient, therefore the luminosity rises strongly. This phase, where the star climbs almost vertically in the CMD, is called *red giant branch* (RGB). At the tip of the RGB the helium core ignites in the *helium core flash*, before the luminosity decreases again and the temperature increases. The detailed evolution at this point is dependent from the initial mass of the star; stars with $M \gtrsim 1.8 M_\odot$ have a so called *horizontal branch* (HB) evolution, lower mass stars evolve directly into the *asymptotic giant branch* (AGB), during which the energy is produced by helium fusion in the shell. After the AGB phase the temperature increases rapidly before the star forms a planetary nebula and evolves into a white

dwarf which is the very faint final evolutionary stage of stars with $M \lesssim 10 M_{\odot}$.

Some features in CMDs of globular clusters can not be entirely explained by the stages of stellar evolution, for example the presence of stars which seem to be on the MS, but on the blue side of the MSTO. These are called blue straggler stars and were first observed by Sandage (1953). The formation process of them is not yet fully understood but might be related to binaries (e.g. Stryker, 1993).

The assumption that a globular cluster consists of a single stellar population, i.e. stars of the same age and same initial chemical composition, has been challenged with the observation of *multiple populations*, for example by the split of the main sequence in the cluster ω Centauri. The feature of multiple populations was initially thought to be only present in some peculiar globular clusters, later it were assumed to be a feature of rather massive clusters while today it is accepted that multiple populations in globular clusters are a universal feature, even though it is not fully understood how they were formed. An overview of the history of multiple population observations is given by Gratton et al. (2012). A more recent review, focusing on theories trying to explain the formation of multiple populations and concluding that by now no theory can fully explain this mystery, is given by Bastian and Lardo (2018).

1.1.2. History of Globular Cluster Observations

Globular Clusters have been observed for more than 300 years since the first GC – M 22 – was discovered by Abraham Ihle in 1665 (Schultz, 1866). However, it was not until 100 years later, in 1764, with the development of better telescopes, that single stars in these clusters could be resolved. The first one to do so was Charles Messier (Académie des sciences (France), 1771). The term *globular cluster* was coined by William Herschel who more than doubled the number of known globular clusters from 34 to 70 when publishing his *Catalogue of a Second Thousand of New Nebulae and Clusters of Stars* (Herschel, 1789). He was also the first to be able to resolve all of these "nebulae" into single stars. The number of known Galactic globular clusters steadily increased until Harris (2010) has listed a total of 157 GCs in the Milky Way, which are spherically distributed around the Galactic center. However, it is expected, that there are about 180-200 GCs in total in the Milky Way. Examining this distribution in detail together with distance measurements, Shapley (1918) came to the conclusion that the dimensions of the Milky Way were much greater than previously been thought, although he overestimated the size by

a factor of roughly two. Besides our galaxy it seems like all bright galaxies as well as many dwarf galaxies are surrounded by globular clusters.

The greatest challenge in studying the details of GCs is the large stellar density of these objects. Since several thousand stars are crowded on a projected area of about $1\,\mathrm{arcmin}^2$, the spatial resolution of an instrument observing it has to be less than 1", which has been achievable for photometric studies, while spectroscopic studies using classical long-slit or multi-object spectroscopy were limited to observing the outermost or very bright stars, where it can not be told for sure if a single star or a blend of several stars is observed. Also, the spectroscopic studies focusing on very bright stars were biased towards giant stars and were missing out the large majority of fainter main sequence stars.

1.2. The MUSE Instrument

1.2.1. The Integral Field Spectrograph MUSE

The problems mentioned above are addressed by *integral field spectroscopy*, which both gives spatial and spectral information of the observed objects. There are basically three concepts in building an integral field spectrograph (IFS), where each has its advantages and disadvantages regarding e.g. spatial or spectral resolution. They all have in common that the field of view is reformatted and fed into a classical spectrograph. The part of the integral field spectrograph which reformats the image is called *integral field unit* (IFU).

The first concept is known under the term *image-slicer* and uses segmented mirrors which send light from different parts of the image in different directions. There, it is captured by another set of mirrors and redirected towards the spectrograph. The disadvantage of this concept is its relatively small field of view and the difficulty in building advanced image-slicers with low amounts of light loss. The second concept uses an array of lenslets to split the image. In this concept, the spatial resolution is typically larger and the spectral resolution lower than in the image-slicer concept. The third concept uses optical fibres placed in the image plane which transfer the light to the spectrograph. This concept is rather flexible and allows for relatively high spectral resolution whereas the spatial resolution is the lowest of the three concepts (Eisenhauer and Raab, 2015; Husser, 2012).

The *Multi Unit Spectroscopic Explorer (MUSE)* (Bacon et al., 2010, Fig 1.2) is an

integral field spectrograph which is mounted on one of the two Nasmyth platforms of Unit Telescope 4 ("Yepun") of the Very Large Telescope at Paranal Observatory in Chile.

MUSE actually consists of 24 identical IFUs which make use of the image-slicer concept. The relatively large field of view of $1' \times 1'$ is first pre-sliced into 24 slices, where each feeds one IFU which is equipped with a spectrograph and a 4k× 4k CCD.

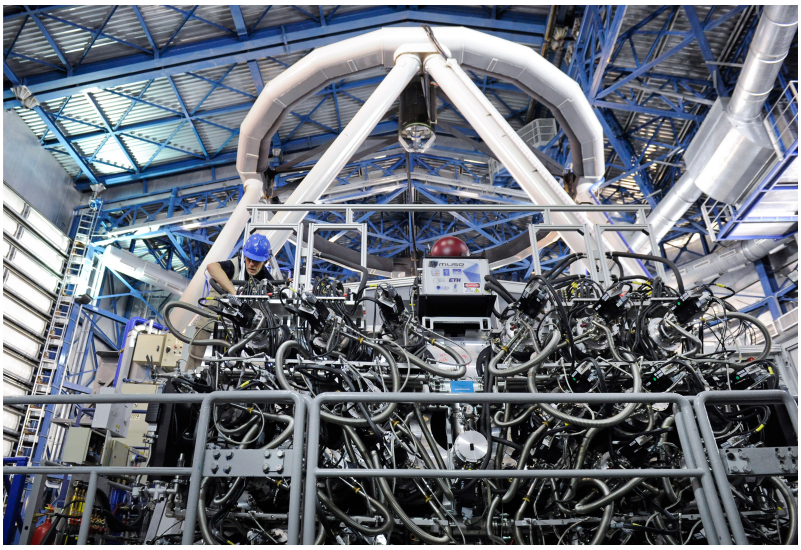

Figure 1.2.: A picture of the MUSE instrument at the Nasmyth focus of the VLT. The 24 single IFUs and especially their cooling systems are visible. Credit: ESO, CC-BY 4.0

The spatial resolution of the MUSE instrument is 0.2" and it works in a wavelength range between 4750 Å and 9350 Å with a spectral resolution between $R = \frac{\lambda}{\Delta\lambda} = 1700$ at the blue end and $R = 3500$ at the red end of the spectral range. There has been a very recent proposal to build a follow-up instrument of MUSE, called BlueMUSE which extends the capabilities of MUSE into a bluer wavelength range (Richard et al., 2019).

1.2.2. A Stellar Census in Globular Clusters with MUSE

In the ongoing observation programme of MUSE 27 Galactic globular clusters as well as 2 globular clusters in the Large Magellanic Cloud have been observed. Figure 1.3 shows 25 of the Galactic globular clusters. These observations have pushed forward the limits in globular cluster research. Huge efforts have been made in understanding cluster dynamics as well as their chemistry (Kamann et al., 2018; Husser et al., 2016). Other results include the finding of a stellar mass black hole (Giesers et al., 2018) and a nova remnant (Göttgens et al., 2019) inside a globular cluster, both being amongst the first observations of one of those objects inside a globular cluster.

Figure 1.3.: Mosaic of all observed Galactic globular clusters, created from reduced MUSE data. The figure is taken from Kamann et al. (2018).

2. Theoretical Foundations

In this chapter some of the fundamental processes which determine the inner structure of stars are summarised. A complete treatment of stellar interiors would go far beyond the scope of this work; here, only a glimpse of what is most important for investigating several mixing processes inside stars summarised using the term *atomic diffusion* (AD can be given. In order to do this, first the mixing processes present in stars are summed up before the overall inner structure of stars is explained. In the end a stellar evolution code, MESA, is introduced, which is used to model stellar interiors.

2.1. Mixing processes inside stars

The material inside a star is mixed by different processes which alter the initial composition. The most important effect is convection which describes energy transport by matter transport. It appears where the *Ledoux criterion* is fulfilled, i.e. the sum of the radiative temperature gradient and the gradient in chemical potential are larger than the adiabatic temperature gradient, so that material rises or sinks down due to pressure difference. In stellar interiors there are three conditions which can be met in order for the respective region to be convective. First, an increasing opacity, which generally happens when temperature decreases, leads to a high radiative temperature gradient. This occurs in the cooler outer layers. Second, the energy generation rate can be highly sensitive to temperature. This occurs in the cores of heavy stars ($M_* \gtrsim 1.3 M_\odot$) where the H-burning is dominated by the CNO-cycle instead of the less temperature sensitive pp-chain. Third, in ionisation zones the adiabatic temperature gradient goes to zero which is why these zones in the outer layers also become convective. (Salaris and Cassisi, 2017)

Convection can be treated by hydrodynamical simulations, which is very costly. For this reason convection is often described using the *mixing length theory*. In a basic picture the theory is equivalent to molecular heat transfer where the analog

to molecules are the convective elements and the analog to the mean free path is the *mixing length* l_m. After one mixing length the convective element dillutes. The advantage of this theory is that the only free parameter is l_m which is usually assumed to be in the order of the pressure scale height H_P. To be more precise, the parameter which is needed is the *mixing length parameter* α_{MLT}, defined by

$$l_m = \alpha_{\mathrm{MLT}} H_P. \tag{2.1}$$

α_{MLT} is assumed to be of the order of 1. More reasonable values are obtained by comparison of the effective temperature or radius of stellar models with observed stars or hydrodynamical simulations. From this method values between 1.5 and 2.0 are obtained. (Kippenhahn, 2013, chapter 7)

The time scale for convective motion t_{conv} can be estimated by

$$t_{\mathrm{conv}} = \frac{l_m}{v_{\mathrm{conv}}}, \tag{2.2}$$

where v_{conv} is the average velocity of a gas bubble. For the Sun one obtains with $l_m \approx R_\odot/5 \approx 1.4 \times 10^8\,\mathrm{m}$ and $v_{\mathrm{conv}} \approx 50\,\mathrm{m\,s^{-1}}$ a time scale $t_{\mathrm{conv}} \approx 2.8 \times 10^6\,\mathrm{s} \approx 30\,\mathrm{d}$ (Carroll and Ostlie, 2014, pp. 407, 419). During this time the material inside the convective zone is completely mixed.

Other transport mechanisms are referred to using the term *atomic diffusion* (AD). The most important mechanisms are the two competing mechanisms *radiative levitation* and *gravitational settling*. These processes are mass dependent, i.e. different atomic species are accelerated differently which leads to different concentrations of atomic species in different layers. The time scale of gravitational settling t_{gs} can be estimated by

$$t_{\mathrm{gs}} = \frac{H_P}{g t_{\mathrm{D}}}, \tag{2.3}$$

where H_P is the pressure scale height, g the gravitational acceleration and t_{D} the diffusion time scale. As H_P is proportional to $1/g$ the time scale is proportional to $1/g^2$. Therefore it is highly dependent on the depth and the evolutionary state. At the surface of a main sequence star the time scale of elements being affected by gravitational settling is several years while in compact objects like white dwarfs it is several days and in neutron stars it is around 10^{-9} seconds (Michaud et al., 2015). Due to this effect the spectrum of a white dwarf theoretically appears as a

pure hydrogen spectrum despite the fact that these stars have used up almost their entire hydrogen. All the hydrogen which is left is on a very thin layer at the surface while all the other elements are stratified below. That is a prominent and extreme example of the effects of AD.

Radiative levitation describes the effect of the net photon momentum outwards and counteracts gravitational settling by introducing additional acceleration g_{rad} which differs for every atomic species. This effect makes for some elements to be pushed into the convective zone from below resulting in increasing abundance while other elements are less affected by this effect and sink below the convective layers. The larger the convective zone gets, the more is this effect erased. Since the calculation of the size of this additional effect is very costly, many stellar model calculations neglect it.

Many other effects introduce additional mixing terms to the governing equations as well. Those effects include rotation, magnetic fields, mass loss and accretion.

A more in-depth-analysis of the effects mentioned in this section can be found in Michaud et al. (2015) or Salaris and Cassisi (2017).

2.2. The inner structure of stars

The inner structure of stars is dependent on their initial mass, its initial metallicity as well as its age, since the fusion processes differ in efficiency depending on pressure and temperature.

The overall structure of a star is mainly governed by hydrostatic pressure from the inside which balances gravity. In the core the fusion processes take place. These fusion processes produce the energy which is radiated away by the star. There are two competing processes inside the star to transport the energy from the core to the surface: *radiation* and *convection*. The radiation is the dominating process if the radiation pressure dominates over the hydrostatic pressure.

Stars which are more massive than $0.35 M_{\odot}$ have a *radiative zone* above the core in which the energy is transported mainly or only by radiation and not by matter transport. Above the radiative zone there is the *convective zone* in which the energy transport is mostly by convection, i.e. matter transport. The ratio between the radius of the convection zone and the stellar radius is larger in lower mass stars, as cooler stars tend to have a higher opacity in the outer layers: Stars with $M_{*} \lesssim 0.35 M_{\odot}$ are fully convective (Reiners and Basri, 2009), in the Sun the fraction is

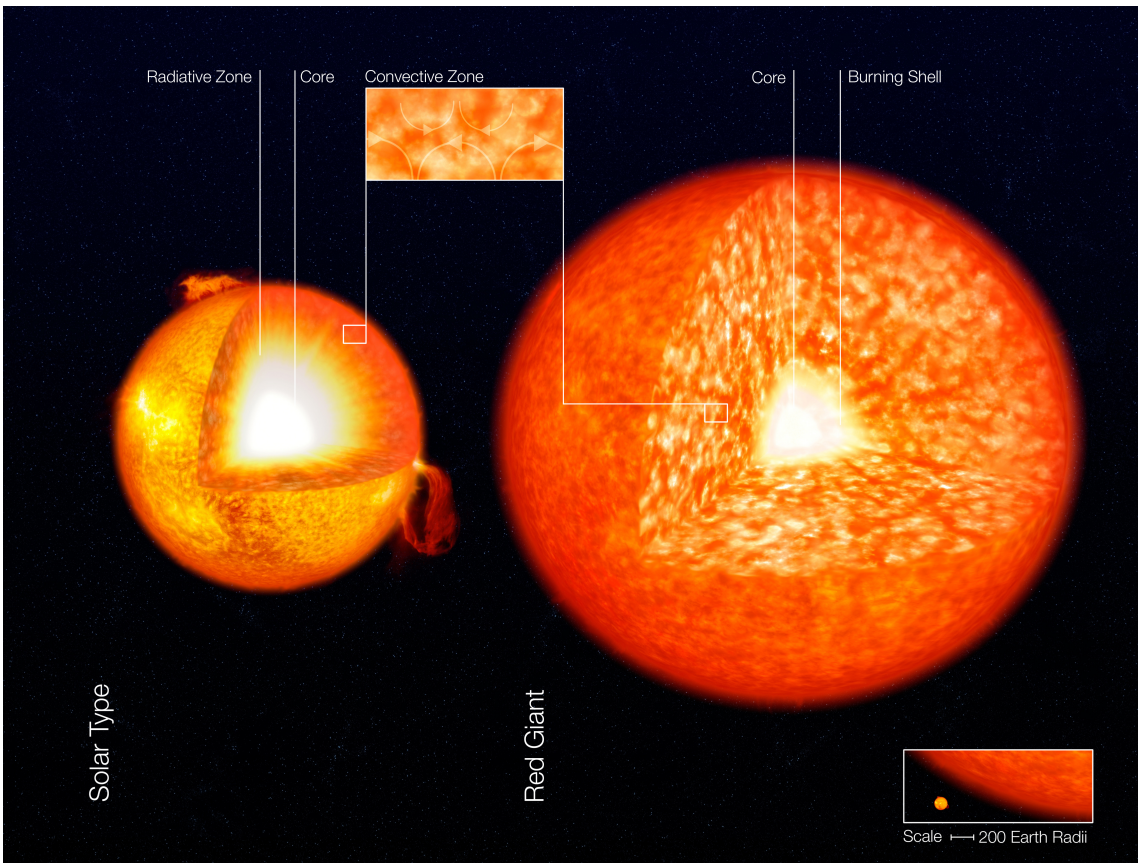

Figure 2.1.: Illustration of the inner structure of a solar type star (left) and a red giant (right). Illustration: ESO, CC-BY 4.0

around 28 % (Carroll and Ostlie, 2014, p. 324) and stars of spectral type O or B have almost no convection zone.

After the stars leave the main sequence, the effective temperature decreases (cf. Section 1.1.1) and the opacity in the photosphere increases. Due to this reason the depth of the convection zone increases again during the SGB phase (cf. Fig. 2.1).

The surface of a star is a few hundred to thousand kilometres thick and is called *photosphere*. This is the volume where the optical depth drops below 2/3. That means, most of the light coming from the stellar interior is scattered for the last time in this area. This light carries information in the form of the stellar spectrum. From the features of this spectrum many properties of the star can be inferred: the continuum shape reveals the effective temperature (T_{eff}), the line widths and depths of distinctive lines reveal the surface gravity (g) as well as the chemical composition, while shifts of the spectrum are explained by a blue- or redshift due to the radial velocity of the star which in turn can give hints towards the star being a binary

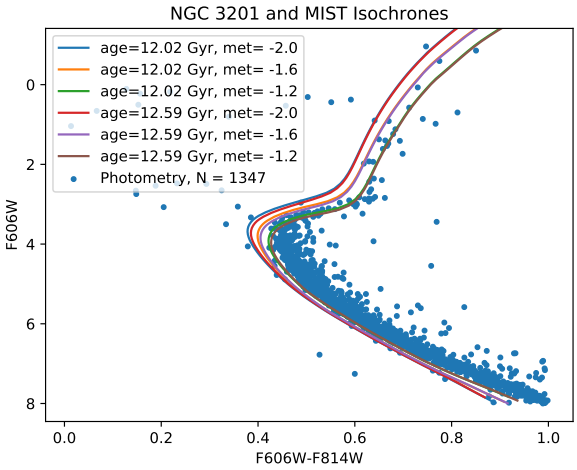

Figure 2.2.: CMD of the globular cluster NGC 3201 together with MIST isochrones of different ages and metallicities [2]. The literature value for the metallicity of the cluster is [Fe/H] $= -1,59$ (Harris, 2010).

system or reveals if the star belongs to the cluster.

Due to the high optical density below the surface the light loses any information about processes going on in this area. Any information from there can only be retrieved by indirect methods like asteroseismology or the comparison of stars of the same population.

2.3. Modeling stellar evolution

The effects described in Section 2.1 are modelled by *stellar evolution codes*. Those codes use the fully coupled structure and composition equations which govern the inner structure of stars. A modern stellar evolution code is the MESA code[1] which is described by Paxton et al. (2011, 2013, 2015, 2018). This code can model a wide range of stars from very low-mass to massive stars.

One feature of the MESA code is its ability to include particle diffusion and gravitational settling. Other effects like radiative levitation were later introduced.

The *MIST* project[2] uses the MESA code in order to compute *isochrones* (Dotter, 2016; Choi et al., 2016). Isochrones are paths in the color-magnitude diagram where stars of different mass having the same age and initial metallicity are found.

[1] `mesa.sourceforge.net`
[2] *MESA Isochrones and Stellar Tracks*, `http://waps.cfa.harvard.edu/MIST/index.html`

Figure 2.2 shows six isochrones for different metallicities and ages. Since it is assumed that all stars inside a globular cluster were formed from the same molecular cloud they all share the same age and initial metallicity. Therefore these parameters can be inferred from fitting isochrones to the CMD of the cluster.

Dotter et al. (2017) use MIST Isochrones in order to analyse the effects of AD described in section 2.1 on the variations in metallicity between young and evolved stars. The results of that study are summarised in this section.

Next to the aforementioned mixing processes convection, radiative levitation and gravitational settling, two additional processes are included in that study. The effect of *overshoot mixing* accounts for the fact that the motion of convective elements doesn't stop at the boundary between radiative and convective zone, but it extends into the stable regions. This behaviour is addressed by introducing free parameters into the equations which are calibrated on observations of eclipsing binaries and open clusters. The term *turbulent mixing* summarizes additional mixing effects which counteract diffusion effects by introducing an additional term in the chemical evolution equations. This term is not directly connected to a specific physical mechanism. The parameters describing this term are calibrated by studies like the ones described in Chapter 3 (Salaris and Cassisi, 2017).

Their efficiency is controlled by free parameters. The resulting effect can be seen in Figure 2.3. The zone where mixing is efficient is extended below the region where convection occurs according to mixing length theory. Besides, it can be seen that the convection zone is less deep in the metal poor star despite the fact that its initial mass is less and therefore the convection zone should be deeper at the same metallicity. The resulting effect can be seen in the left panel in Figure 2.4. Here it is visible that the observed metallicity deviation between MSTO and RGB is larger for lower metallicities which is a consequence from deeper convection zones in more metal rich stars. Another feature that can be seen from this plot is that stars which reach the MSTO earlier have a larger metallicity spread which is a consequence from the fact that more massive stars which evolve faster and therefore reach the MSTO earlier have shallower convection zones than low-mass stars. On the RGB the metallicity is slightly enhanced due to the so called *first dredge-up*. In this phase the surface convection zone reaches the core burning region and brings material from the core where hydrogen burning has reduced the amount of hydrogen up to the surface. The resulting effect is a slight decrease in hydrogen relative to other elements and therefore increase of metallicity at the surface. In the right

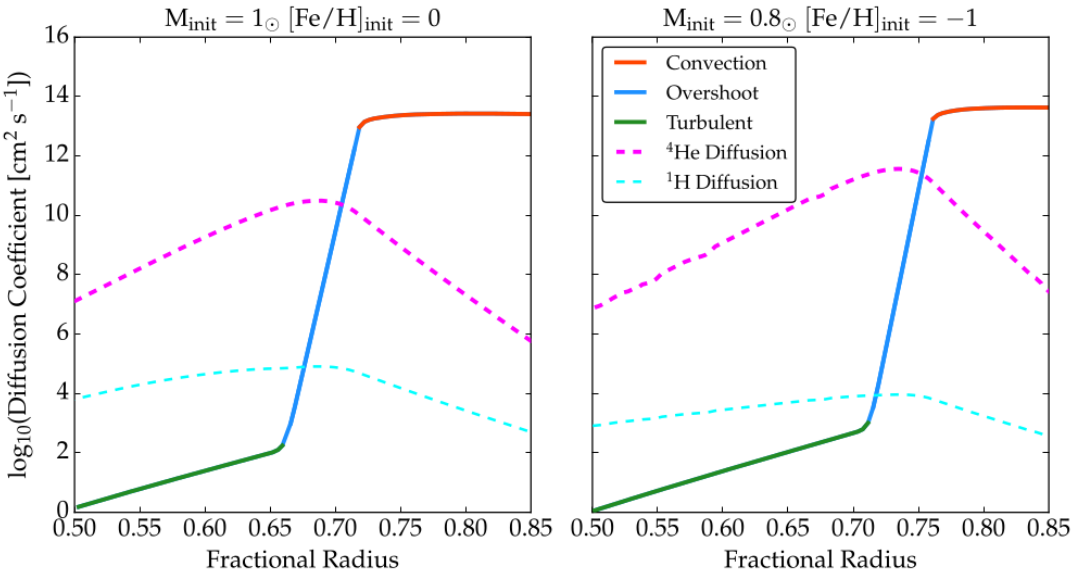

Figure 2.3.: Diffusion coefficient profiles at the base of the convective zone. The diffusion coefficient is a measure for the mixing efficiency. The profiles are taken near the end of core-H-burning, i.e. the main sequence-turnoff. The left panel shows a star with solar mass and solar metallicity, in the right with lower mass and metallicity. The different colored solid lines show the most dominant contribution to the diffusion coefficient. The dashed lines show the results for atomic diffusion for hydrogen and helium, respectively. The figure is taken from Dotter et al. (2017).

panel of the same figure this trend gets even more visible. Stars with masses below $\approx 0.35 M_{\odot}$ have no metallicity spread since they are fully convective. In higher-mass stars the metallicity spread increases with increasing mass and age until stars reach the MSTO after which the spread rapidly decreases. Therefore the effect of atomic diffusion is strongest at the MSTO.

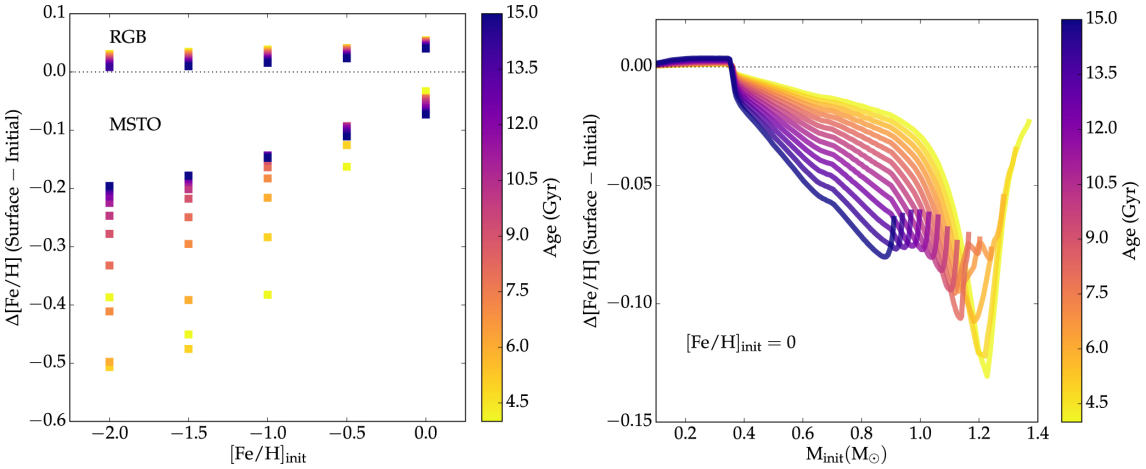

Figure 2.4.: Deviations from surface metallicity with respect to initial metallicity. In the left panel this spread is shown for different metallicities (on the x-axis) as well as for different ages (color coded) on the main sequence turnoff (MSTO) and the red giant branch (RGB). In the right panel the same spread is shown as a function of mass for different ages. The figures are taken from Dotter et al. (2017).

3. Previous studies on Atomic Diffusion in Stellar Clusters

In Section 2.3 it was shown how the analysis of atomic diffusion is theoretically treated, nevertheless it needs comparison with observations in order to confirm the models or put constraints on the used parameters like the ones for modelling turbulent or overshoot mixing as mentioned earlier.

There have been several studies on atomic diffusion in star clusters in the past, namely in the open cluster M67 (Gao et al., 2018; Bertelli Motta et al., 2018) and the globular clusters NGC 6341 (M92) (Boesgaard et al., 1998; King et al., 1998), NGC 6397 (Korn et al., 2007; Nordlander et al., 2012; Husser et al., 2016), NGC 6752 (Gruyters et al., 2013, 2014), NGC 6121 (M4) (Mucciarelli et al., 2011), and NGC 7099 (M30) (Gruyters et al., 2016), which are summarized in this section. These studies are mostly multi-object- and high resolution spectroscopy studies based on samples of a dozen up to a few hundred stars.

3.1. M 92

The first cluster for which atomic diffusion effects were observed was the globular cluster M 92, which is the most metal poor globular cluster known in the Milky Way with an overall metallicity of -2.31 dex (Harris, 2010). Boesgaard et al. (1998) and King et al. (1998) analysed 6 subgiants with the HIRES spectrograph[1] at the Keck Observatory with a spectral resolution of $R = \lambda/\Delta\lambda = 45000$. The studies used *non-LTE* (NLTE) corrections for the Li abundances, i.e. in the calculation of model atmospheres used for the spectrum fit deviations from the usual assumption of local thermodynamic equilibrium (LTE) were taken into account. This analysis introduced very small corrections by about 0.02 dex.

[1]Technical details of the HIRES spectrograph are given in `https://www2.keck.hawaii.edu/inst/hires/`

These studies found a spread in [Fe/H] of 0.15 dex between one of the analysed subgiants and two others. However, King et al. (1998) claim that there might be problems with determining stellar properties, so it is in question if this is definitively the first evidence of atomic diffusion in globular clusters.

3.2. NGC 6397

The first systematic studies of abundance trends were done in the globular cluster NGC 6397. Two studies were carried out, one with 18 stars between the main sequence turnoff and the red giant branch which were observed with the *FLAMES/UVES* spectrograph[2] on the VLT at a high resolution of $R = 47000$ (Korn et al., 2007; Nordlander et al., 2012), another one was carried out using the multi-object spectrograph *FLAMES/GIRAFFE*[2] where 116 stars of the same cluster were observed (Lind et al., 2008). The studies used NLTE corrections in order to calculate stellar spectra. While the GIRAFFE study covers more stars, the stars of the UVES study cover a larger range in the CMD.

NGC 6397 has an initial metallicity of -2.02 dex (Harris, 2010). The UVES study found a deviation of about 0.15 dex in iron abundance between stars at the main sequence turnoff and red giant branch. These deviations are compared to stellar evolution models where three models are used which differ in efficiency of turbulent mixing. The left panel in Fig. 3.1 shows abundance trends in four different atomic species (Mg, Ca, Fe, and Ti) which are in good agreement with one of the applied atomic diffusion models which refers to a medium turbulence efficiency in all of the four analysed elements. The GIRAFFE study found a difference in iron abundance of 0.13 dex betweeen turnoff and the coolest RGB star.

NGC 6397 was also the first cluster which was analysed in detail with the integral field spectrograph MUSE. Part of this analysis was an investigation of the metallicity trends (Husser et al., 2016). This analysis on a sample of 12307 stars supported previous high resolution studies by finding a deviation between metallicity on turnoff and RGB of about 0.2 dex (Fig. 3.1, right panel). The study was made without taking into account NLTE effects, however it was compared with measured metallicities with applied NLTE corrections. The corrected metallicities were higher by about 0.06-0.08 dex, but this effect only shifts metallicities for all the stars and

[2] For technical details of the FLAMES spectrographs UVES and GIRAFFE see the ESO website `https://www.eso.org/sci/facilities/paranal/instruments/flames/overview.html`.

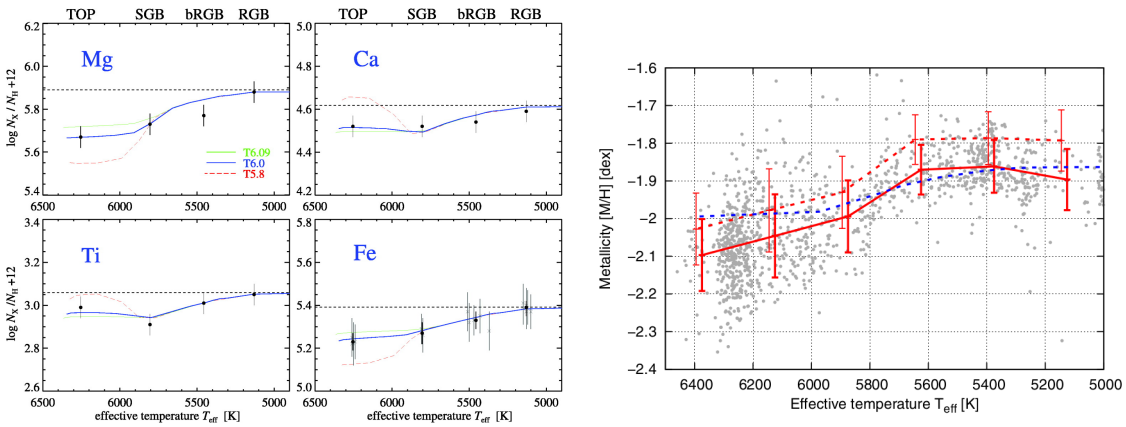

Figure 3.1.: Abundance trends in the globular cluster NGC 6397. The left plot shows the results of the UVES study (Korn et al., 2007), the right one those of the MUSE study (Husser et al., 2016). The figures are taken from the mentioned publications.

therefore does not weaken the trend.

3.3. NGC 6752

The globular cluster NGC 6752 has a medium metallicity of -1.54 dex (Harris, 2010). Two studies were carried out, one with the FlAMES/UVES (Gruyters et al., 2013) and one with the FLAMES/GIRAFFE spectrograph (Gruyters et al., 2014). The UVES study included 16 stars between MSTO and the tip of the RGB while the GIRAFFE study included 194 stars on the SGB and the lower RGB. The studies also used a NLTE analysis in order to calculate synthetic spectra which were used for spectrum fitting.

The results of both of these studies are shown in Fig. 3.2. They show clear trends in all of the four analysed elements Mg, Ca, Fe, and Ti. These trends are in good agreement with the models. The best fitting model for this cluster is that with the most efficient turbulent mixing.

3.4. M 30

For the very metal-poor ($\lfloor$Fe/H$\rfloor$ =-2.27 dex, Harris, 2010) globular cluster M 30 (NGC 7099) one study using the FLAMES/GIRAFFE spectrograph was carried out with 144 stars (Gruyters et al., 2016). Again, a NLTE analysis were used in this

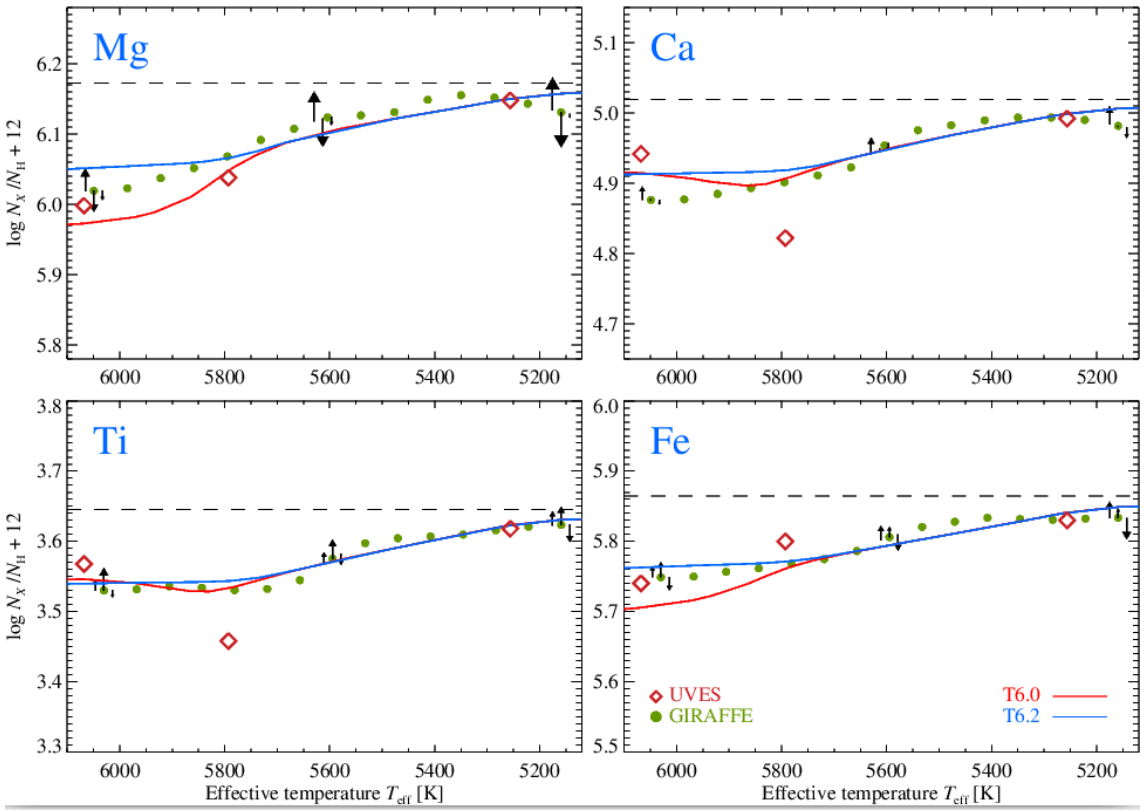

Figure 3.2.: Abundance trends in the globular cluster NGC 6752. This plot shows the results from the UVES study as well as those from the GIRAFFE study. The figure is taken from (Gruyters et al., 2014).

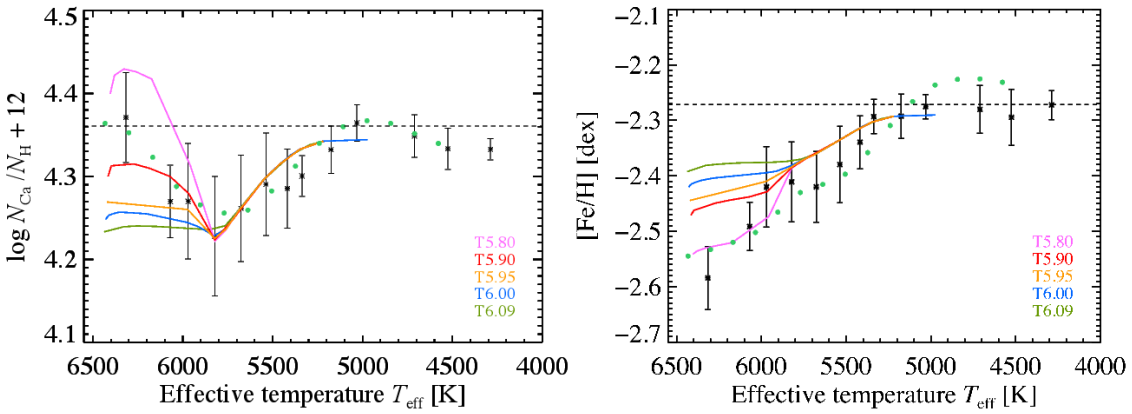

Figure 3.3.: Abundance trends in globular cluster M 30. The metallicities are plotted together with models for atomic diffusion which differ in efficiency of atomic diffusion. The figure is taken from (Gruyters et al., 2016).

study.

This study found abundance trends in calcium and iron of about 0.2 dex between main sequence turnoff and red giant branch (Fig. 3.3). The results agree very well with the model with less efficient turbulent mixing.

3.5. M 67

The open cluster M 67 has a population of stars which is very similar to the sun in terms of metallicity and age. Three studies were recently carried out which found abundance trends in this cluster (Gao et al., 2018; Bertelli Motta et al., 2018; Souto et al., 2018). These studies were part of larger surveys, namely the GALAH survey[3], the GAIA-ESO survey[4], and the APOGEE survey[5].

The stars used in the respective studies are marked in the color magnitude diagram of the cluster in Fig. 3.4. This study also analyses stars on the upper main sequence. The GALAH study uses a NLTE analysis in order to determine abundances and compared this to results of a LTE analysis. The effects of the NLTE analysis on abundances of different elements are shown in Fig. 3.5. For all elements except Oxygen the abundance on the giant branch tends to be lower than in an LTE analysis while at the turnoff there is no difference or even vice versa. This leads

[3] https://galah-survey.org/
[4] https://www.gaia-eso.eu/
[5] https://www.sdss.org/dr12/irspec/

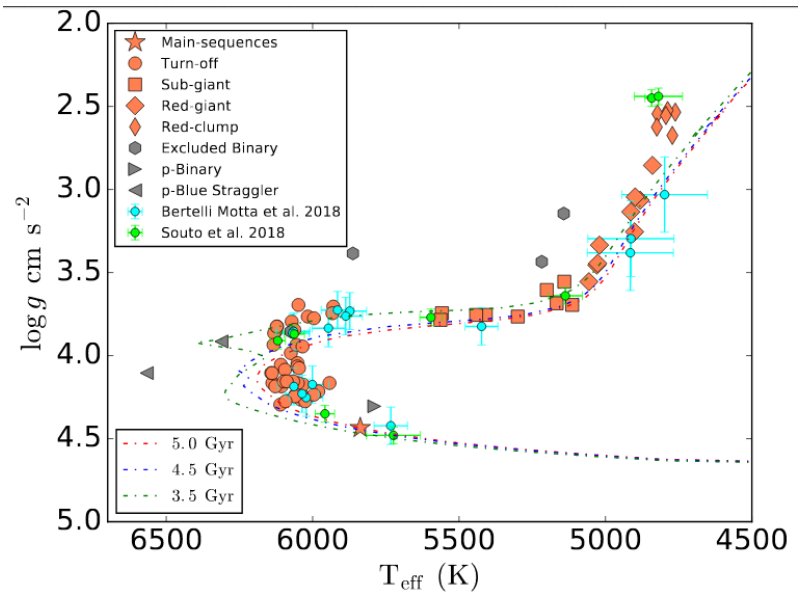

Figure 3.4.: The color magnitude diagram of the open cluster M 67. In this figure the stars from the GALAH study (Gao et al., 2018), the APOGEE study (Souto et al., 2018) and the GAIA-ESO study (Bertelli Motta et al., 2018) are marked. The figure is taken from (Gao et al., 2018).

to mitigation of the positive abundance trends between turnoff and giant branch in the NLTE analysis. The trend observed in M 67 is shown in Fig. 3.6 in six different elements for the three aforementioned studies together with abundance trends derived from MIST isochrones (cf. Section 2.3) of three different ages and solar metallicity.

The trends are much weaker than in the aforementioned globular clusters and can only be observed up to the subgiant branch, afterwards the abundances are lower than predicted.

3.6. Conclusion and Relevance for the present study

The theoretical results from Section 2.3 predicted that the variations should be weaker in younger and more metal-rich populations, therefore the results from these studies qualitatively confirm the predictions of simulations.

The results of these studies also suggest that a higher metallicity causes a higher efficiency of turbulent mixing.

None of these studies has taken into account stars which are much below the MSTO, therefore effects of AD on the main sequence can not be constrained by these

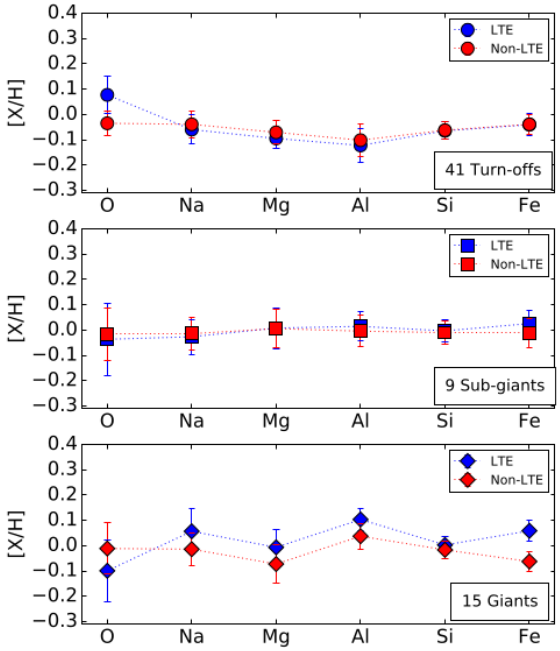

Figure 3.5.: Effects of deviations from the LTE assumption on abundances in stars of different evolutionary stage. The abundances of single elements with LTE (blue) and non-LTE (red) are plotted relative to solar abundance. The figure is taken from (Gao et al., 2018).

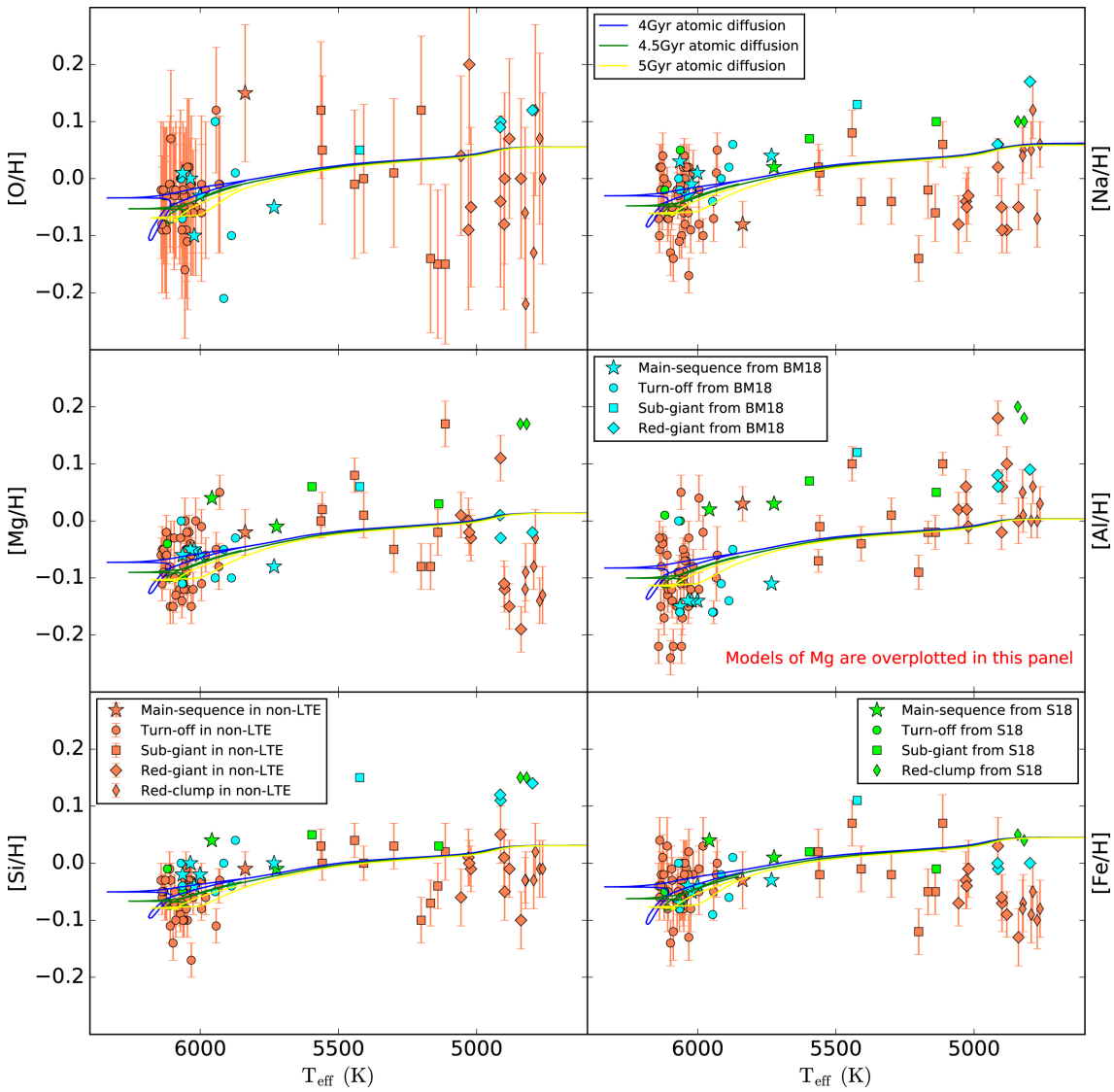

Figure 3.6.: Abundance trends in the open cluster M 67. The trends for six different elements are plotted. Blue symbols refer to data from GAIA-ESO survey (Bertelli Motta et al., 2018), green refer to data from APOGEE survey (Souto et al., 2018) and orange symbols refer to data from GALAH survey (Gao et al., 2018). The results from the latter study are obtained using a non-LTE analysis. Overplotted are isochrones used by Dotter et al. (2017) for solar metallicity and different ages. The figure is taken from Gao et al. (2018).

studies. Also, due to the small sample numbers no continuous trends in metallicity can be observed and so the precise shape of the profiles can not be constrained as a whole. In Figure 3.1 the difference between a high resolution and a MUSE study is directly visible. For this reason we use the MUSE instrument in order to perform studies on clusters without preselecting stars.

4. Analysing Metallicity Trends with MUSE

In this chapter the data and the methods which are used in this work are explained. The goal is to examine the globular clusters from the MUSE survey (Section 1.2.2) for trends in their metallicity along the CMD. In order to do so, both spectroscopic data from the MUSE instrument as well as photometric data, e.g. from the Hubble Space Telescope (HST) are needed. Besides, methods in order to group ("bin") the data are used to make use of the large amount of stars in the survey which is the advantage of integral field over classical or multi-object spectrographs.

4.1. The used data

This work is based on spectroscopic data obtained with the MUSE instrument (cf. Section 1.2.1) as well as on photometric data obtained with the HST. In this section it is summarized how these data are processed. As processing MUSE data was not directly part of this work, this section is mostly based on previous works except for Section 4.1.3.

4.1.1. Observations and Data Reduction

The results presented in this work are part of a survey of 27 Galactic globular clusters which are selected to be within a distance of 15 kpc, massive and well visible from Paranal Observatory (Kamann et al., 2018).

Table 4.1 shows which clusters were observed how often and how many spectra from how many stars were obtained. The two clusters NGC 6397 and NGC 6522 have been observed with MUSE but are not part of this work yet. There are more spectra than stars in the survey, since many stars were observed multiple times due to overlap between the pointings and repeated observations.

Table 4.1.: Summary of Observations. One pointing is a field of view at a specific position in the night sky. There are always several exposures of one single pointing in order to combine those exposures and thus improving the SNR. The values for [Fe/H] and E_{B-V} are taken from Harris (2010).

Name	[Fe/H]	E_{B-V}	Pointings	Exposures	Stars	Spectra
NGC 104	-0.72	0.04	10	392	48385	337161
NGC 1851	-1.18	0.02	4	103	19424	74107
NGC 1904	-1.60	0.01	4	75	12445	39260
NGC 2808	-1.14	0.22	5	52	25972	45941
NGC 3201	-1.59	0.24	6	197	6750	69560
NGC 362	-1.26	0.05	6	39	15044	28683
NGC 5139	-1.53	0.12	12	371	77617	433897
NGC 5286	-1.69	0.24	1	12	13417	18854
NGC 5904	-1.29	0.03	6	53	27839	54833
NGC 6093	-1.75	0.18	4	32	17926	23748
NGC 6121	-1.16	0.35	2	6	1684	1266
NGC 6218	-1.37	0.19	4	36	8897	23200
NGC 6254	-1.56	0.28	8	44	23288	30265
NGC 6266	-1.18	0.47	4	40	23262	40796
NGC 6293	-1.99	0.36	1	7	4486	2796
NGC 6388	-0.55	0.37	4	45	26731	49835
NGC 6441	-0.46	0.47	4	51	26627	47398
NGC 6541	-1.81	0.14	5	40	18497	38503
NGC 6624	-0.44	0.28	1	7	6733	8605
NGC 6656	-1.70	0.34	4	40	19917	37820
NGC 6681	-1.62	0.07	1	6	7084	8383
NGC 6752	-1.54	0.04	8	61	20169	31791
NGC 7078	-2.37	0.10	4	33	32006	42720
NGC 7089	-1.65	0.06	4	48	25684	51201
NGC 7099	-2.27	0.03	4	48	15692	39584

The reduction of the data was done using the standard MUSE pipeline described by Weilbacher et al. (2012). First, the basic reduction steps like bias subtraction, flat-fielding and wavelength calibration are performed for each of the 24 IFUs separately, where the outcome is one *pixel table* for each IFU. These data are further processed by performing flux calibration. In the end, one pixel table is obtained which contains information about the flux and uncertainty, wavelength and spatial position inside the field of view for every pixel. Pixel tables of individual exposures of each pointing are combined afterwards into a single *datacube* with two spatial dimensions of length 300 pixels and one wavelength dimension with an approximate length of 3750 pixels.

4.1.2. Extraction and Analysis of Spectra

The method how to extract single source spectra from those data cubes is described in detail by Kamann et al. (2013) and briefly summarised here. This method uses an existing source catalogue of HST data by Anderson et al. (2008) as well as an initial guess for the point-spread function (PSF) of the MUSE instrument. These inputs are used to create a mock MUSE image which is cross-correlated against the data cube in order to obtain an initial guess for the coordinate transformation. After that, the signal-to-noise ratio (SNR) and density of sources is estimated and those sources are excluded for which no meaningful spectrum can be extracted, i.e. sources with an SNR smaller than 5 and where the source density exceeds 0.4 brighter sources per resolution element. The remaining sources are then iteratively analysed on every wavelength slice in order to obtain a final PSF model for the whole data cube. The final spectra are then extracted using this new PSF model. This procedure also estimates the background and removes the sky lines.

The method how atmospheric parameters are obtained from stellar spectra is following a method described by Husser et al. (2016). The method uses a library of synthetic spectra calculated with the stellar atmosphere code PHOENIX (Husser et al., 2012). An isochrone is used for an initial guess of the stellar parameters T_{eff} and $\log g$. These initial guesses are used as input for the model spectra which are fitted to the spectra using a full-spectrum fit with effective temperature T_{eff}, metallicity [M/H], radial velocity and other spectral features as free parameters. This method yields either a solar scaled abundance [M/H] if the alpha-element abundance [α/Fe] is fixed to the solar value or a metallicity [Fe/H] when [α/Fe] is treated as a free parameter.

For many stars more than one spectrum exists (cf. Section 4.1.1). Therefore the metallicities computed from the single spectra are averaged in order to get a mean metallicity for each star. This method is called *mean params*, in contrast to *combined params* where spectra of single stars are first combined and the metallicities are inferred from these combined spectra.

The quality of the data is summarised by the SNR. The SNR of single spectra can be improved by taking more exposures of a single pointing or combining several spectra to one spectrum. Since the reliability of the determination of atmospheric parameters, such as metallicity, increases with increasing SNR, the following methods only use spectra above a certain SNR threshold. This threshhold is further called *SNR cut*.

4.1.3. Photometric Data

The photometric data used in this study is mainly provided by the *ACS survey on globular clusters* (Anderson et al., 2008), which was a survey on 65 Galactic globular clusters using the Wide-Field Chanel (WFC) of the Advanced Camera for Surveys (ACS) of the HST (this catalogue was also used for spectrum extraction in the previous section). In this survey all clusters were observed using the filters "F606W" and "F814W". The numbers denote a typical wavelength of the light which passes the respective filter, i.e. light passing through the F814W filter is redder than through the filter F606W. Because of this the denomination of the redder filter is I for *infrared* and for F606W it is V as in *visible*. Four of our clusters (NGC 1904, NGC 6266, NGC 6293, NGC 6522) were not included in the ACS survey, in those cases archival HST images are taken and analysed (Kamann et al., 2018)

We correct the photometric data for interstellar reddening as well as for distance in order to work with absolute instead of relative magnitudes. The reddening correction uses the reddening parameter E_{B-V} from Harris (2010) (cf. Table 4.1) and a line-of-sight-dependent parameter $R(V)$ which is fixed to 3.1 (Fitzpatrick, 1999). Different wavelengths are accounted for using a code based on Fitzpatrick (1999). The distance is taken into account by transforming apparent magnitudes into absolute magnitudes using the distance modulus

$$\mu = 5 \log \left(\frac{d}{10\,\mathrm{pc}} \right),$$

where d denotes the distance taken from Harris (2010).

4.2. Measuring Metallicity Trends

As the MUSE data are medium-resolution, moderate-SNR data (cf. Section 4.1.1), data from single stars from the survey in this work give less accurate values than data from high-resolution spectra as described for example in Section 3. The strength of the MUSE survey is the large number of stars which allows for minor fluctuations in the determination of stellar parameters to be averaged out. In order to find the trend of metallicity over several stages of stellar evolution, stars which are near to each other in the CMD are grouped together in bins. After that the average values of the stars in a bin are calculated and used in the further analysis.

These metallicity trends are then quantified and compared to the corresponding trend predicted by a MIST isochrone (cf. Section 2.3).

4.2.1. Isochrone Fitting

In order to estimate the initial metallicity as well as the age of the cluster, an isochrone has to be found for each cluster. In order to do so, first a 2-dimensional grid of MIST isochrones which are obtained from the MIST website (cf. Section 2.3) in metallicity and age was created.

Then the observational CMD is overplotted with an isochrone matching the parameters obtained from Harris (2010). This isochrone is taken as a starting value, from where the parameters metallicity, age and distance are adjusted such that the isochrone matches the CMD.

4.2.2. Binning

In order to minimize the effect of single observation errors the data are binned together assuming that stars which are close to each other in the CMD have similar atmospheres. The binning can be carried out using different methods where the bins differ in size and homogeneity. In this study four different methods are used which are described in this subsection.

Another approach could be to fit a function to the unbinned metallicities and hence reproduce the shape of the trend. However, this method would be dependent on finding a suitable function which reproduces the trends, as there is no theoretically well-founded analytic function to describe the trends. Due to the huge amount of data and especially the differing density in data (there are a lot more stars in a

smaller magnitude area on the MSTO than on the RGB) it would also be unclear if really the global shape of the trend would be fitted or rather small scale features which have no physical significance.

In future studies it could be useful to combine binning methods and a fitting function but in this work the desired parameters can more easily be inferred from methods without fitting functions.

Fixed bins

The direct approach to binning t is to sort all the stars in a CMD along a monotonously increasing quantity and allocate to bins either via a fixed bin width in this quantity or via a fixed bin size. This quantity was chosen to be the magnitude of the star V. In the calculation of the fixed bin size, first the number of bins is calculated by dividing the number of stars by the fixed bin size. Afterwards the binning is completed using a quantile-based discretization function. As the number of stars in general isn't a multiple of the number of bins and it could appear that two or more stars have the same value for the magnitude, the exact number of stars per bin might differ by a few stars per bin. For fixed bin widths, a bin width of 0.1 mag and for fixed bin sizes a bin size of 100 stars per bin was used.

The disadvantage of this method is its inflexibility towards changes of stellar densities along the CMD. While there are many stars on the main sequence in a relatively small region of the CMD, there are far fewer stars on the RGB. This results in large differences in either bin size (for fixed bin width) or bin width (for fixed bin size). It is questionable if bins on different regions of the CMD can thus still be compared to each other. A solution to this problem could be to adapt bin sizes and bin widths to the region in the CMD. An example for such an approach is the k-means clustering algorithm which will be described later.

Figure 4.1 shows the distribution of stars into bins for these two binning methods for the cluster NGC 3201.

Isochrone binning

A more sophisticated approach is to use an isochrone in order to find a path through the CMD. For this purpose at first an isochrone had to be found using the method described in Section 4.2.1. The isochrone parameters which were found for the

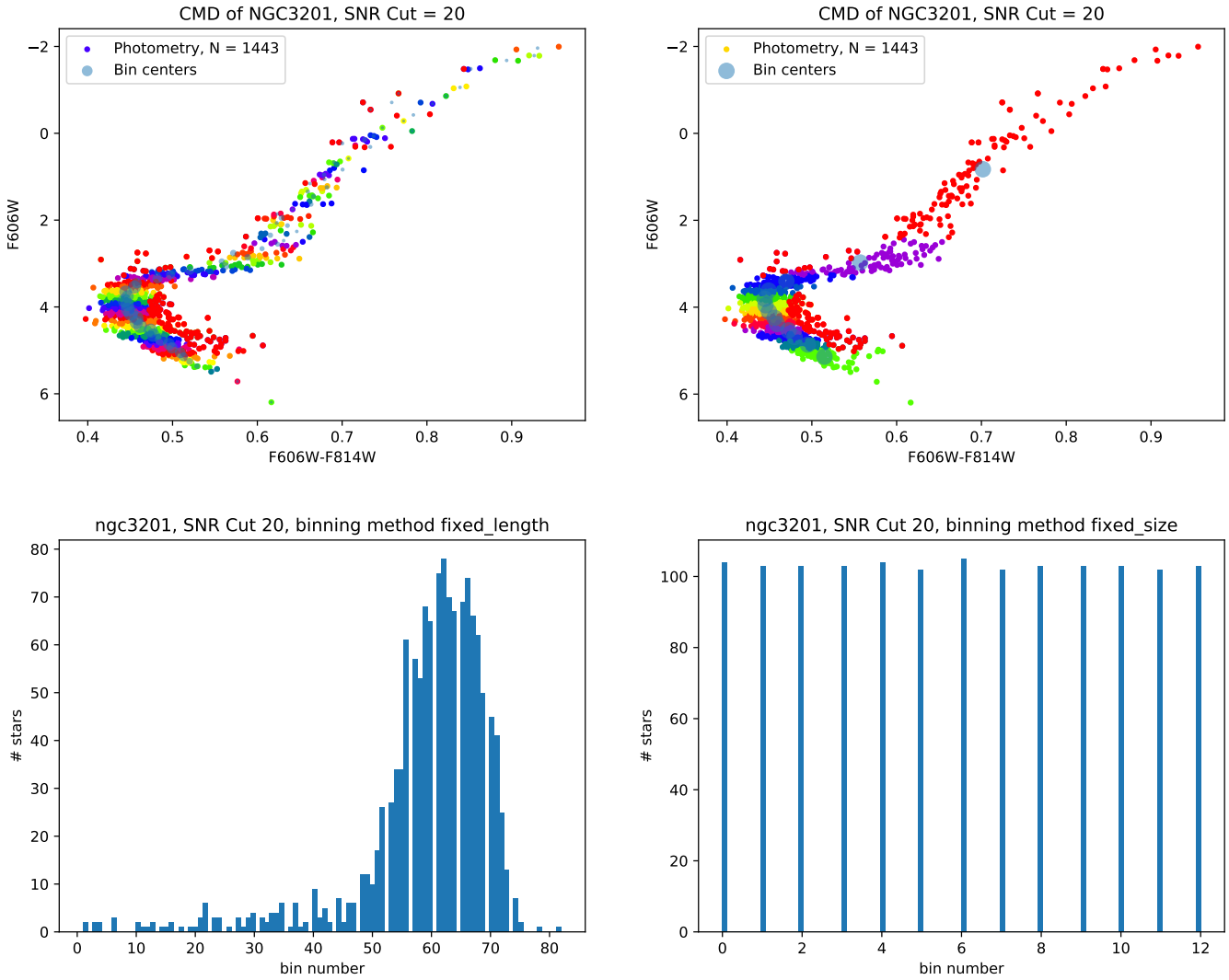

Figure 4.1.: **Upper Panel:** Color Magnitude Dagram of the Cluster NGC 3201 (only stars with SNR > 20 are taken into account), where the bins are colored according to fixed bin width (left) and fixed bin size (right). The bin mean values are also marked, where the size of the marker scales with bin size. **Lower Panel:** Corresponding histograms where the bin sizes for the respective binning methods are shown. Smaller bin numbers account for brighter magnitudes.

Table 4.2.: Parameters found from isochrone fitting.

Cluster	Metallicity	Age
NGC 104	-0.90	1.49×10^{10}
NGC 1851	-1.10	1.40×10^{10}
NGC 1904	-1.10	1.35×10^{10}
NGC 2808	-1.65	1.35×10^{10}
NGC 3201	-1.20	1.26×10^{10}
NGC 362	-1.40	1.17×10^{10}
NGC 5139	-1.55	1.49×10^{10}
NGC 5286	-1.70	1.49×10^{10}
NGC 5904	-1.35	1.41×10^{10}
NGC 6093	-1.35	1.49×10^{10}
NGC 6121	-0.55	1.49×10^{10}
NGC 6218	-1.10	1.48×10^{10}
NGC 6254	-1.90	1.50×10^{10}
NGC 6266	-1.00	1.18×10^{10}
NGC 6293	-2.00	1.30×10^{10}
NGC 6388	-0.90	1.29×10^{10}
NGC 6441	-0.70	1.49×10^{10}
NGC 6541	-2.00	1.48×10^{10}
NGC 6624	-1.00	1.49×10^{10}
NGC 6656	-1.50	1.49×10^{10}
NGC 6681	-0.90	1.48×10^{10}
NGC 6752	-1.00	1.45×10^{10}
NGC 7078	-2.00	1.30×10^{10}
NGC 7089	-1.80	1.32×10^{10}
NGC 7099	-1.65	1.45×10^{10}

clusters analysed in this work are presented in table 4.2.

The isochrone binning method works as follows (Göttgens, 2015):

For an isochrone point $\vec{x} = (x_V, x_{V-I})$ the distance to a star $\vec{s} = (s_V, s_{V-I})$ is measured via

$$d(\vec{x}, \vec{s}) = \sqrt{(s_V - x_V)^2 + w \cdot (s_{V-I} - x_{V-I})^2}, \tag{4.1}$$

where the index V denotes the magnitude (i.e. the ordinate in the CMD) and the index $V - I$ denotes the color (i.e. the abscissa in the CMD) and w refers to a weighting factor which accounts for the fact that the spread in color and magnitude differ by about one order of magnitude. $w = 20$ was found to be a reasonable value. For any isochrone point $\vec{x_i}, i \in \{1, ..., N\}$, where N is the number of points in the given isochrone, the resulting *isochrone bin* B_i from all the observed cluster stars C is now

$$B_i(R) = \{\vec{s} \in C | d(\vec{x_i}, \vec{s}) < R\}.$$

R is a parameter which denotes the radius of the isochrone bin. R can be fixed or adjustable. If there is a given constraint on the binned stars like a minimum or maximum number of stars to be included in the bins the binning procedure has to be iterative which means it starts with a starting value $R = R_0$, does the binning as described, checks whether the criterion is met and, if not, increases or decreases R before it starts over again.

The advantage of this approach is that there are overlapping bins, therefore trends along an isochrone should be continuous. Another advantage addresses the disadvantage of the first methods in using adaptable bin sizes and bin widths. It also does the binning not only in one dimension but accounts for both variables in the CMD. The disadvantage is that an isochrone has to be found for every cluster which fits the CMD well because otherwise the value for R has to be very large in order for a sufficient number of stars to be binned.

Figure 4.2 shows the results of such a binning process in cluster NGC 3201 in showing a CMD and the resulting bins as overplotted circles.

K-means Clustering

A widely used approach to cluster data is the k-means clustering algorithm. The algorithm is explained e.g. in MacKay (2003). For this approach it has to be

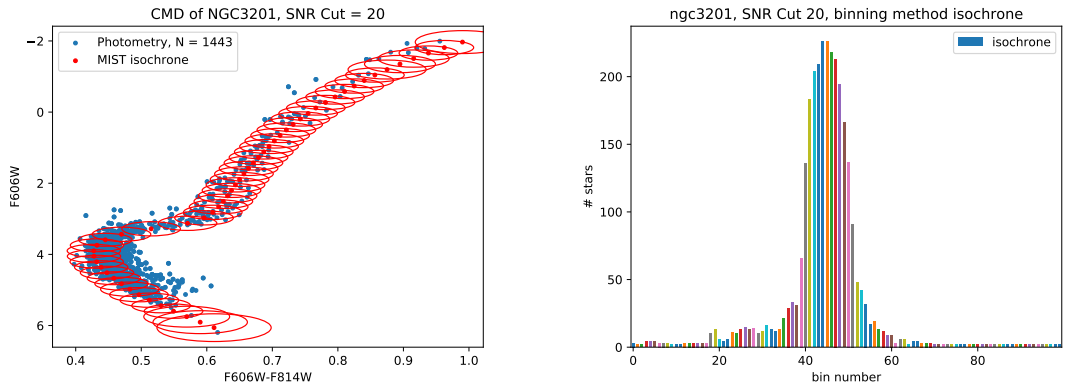

Figure 4.2.: CMD and histogram for isochrone binning of cluster NGC 3201 where only stars with a SNR > 20 are used. The circles denote the size of the bins. Smaller bin numbers account for brighter magnitudes.

specified which number of bins[1] shall be created. 100 was found to be a reasonable value. The algorithm first generates a sample of 100 randomly distributed means. In the next step it assigns each point in the CMD to the mean which is nearest according to the metric defined in equation 4.1. After that it updates the means to the mean of all assigned points and repeats the assignment and update step until the assignment does not change anymore.

Like the isochrone approach this method uses adaptable bin sizes and bin widths. The binning is also not only done in one dimension but accounts for both variables in the CMD. The advantage over the isochrone approach is its independence on finding a suiting isochrone. Its disadvantage is that the binning depends on the initial sample of means and therefore slightly differs with every execution of the algorithm as the initial sample is a random distribution.

Figure 4.3 shows the distribution of stars into bins of a k-means clustering algorithm for the Cluster NGC 3201.

4.2.3. Error estimation

The errors of the metallicity bin values consist of two components: The errors of the single measurements and the statistical errors of the metallicities in the bin. The

[1] In the context of this method the single bins are called *clusters* but I will avoid this term because in the context of this work *clusters* are objects described in section 1.1

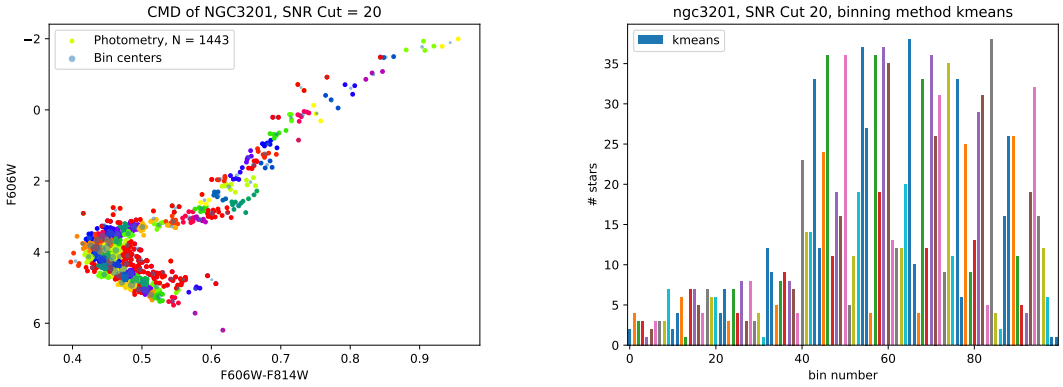

Figure 4.3.: Color Magnitude Diagram and Histogram for kmeans binning of Cluster NGC 3201 where only stars with a SNR > 20 are used. The bins are colorized, the bin centers are marked and the marker size scales with bin size. Smaller bin numbers account for brighter magnitudes.

statistical error σ_s is given by the standard deviation

$$\sigma_\mathrm{s} = \sqrt{\frac{1}{N-1}\sum_i (x_i - \overline{x_\mathrm{bin}})^2}, \tag{4.2}$$

where N is the number of stars in the particular bin, x_i are the single measurements in the bin and $\overline{x_\mathrm{bin}}$ is the mean value of the bin. The errors of the metallicity of single stars σ_i are combined using their quadratic mean

$$\sigma_\mathrm{e} = \sqrt{\frac{1}{N}\sum_i \sigma_i^2}. \tag{4.3}$$

The two error components σ_s and σ_e are then combined to the error of the bin

$$\sigma_\mathrm{bin} = \sqrt{\sigma_\mathrm{s}^2 + \sigma_\mathrm{e}^2}. \tag{4.4}$$

4.2.4. Quantification of metallicity spread

In order to quantify the strength of the metallicity difference a method is implemented to find a value for the spread between the MSTO and the RGB.

The average value on the RGB was determined by finding the average value of all bins for V magnitude larger 0 and smaller 3 and color V-I larger than 0.5, weighted by their errors (cf. section 4.2.3). The value of the metallicity at the turnoff is more

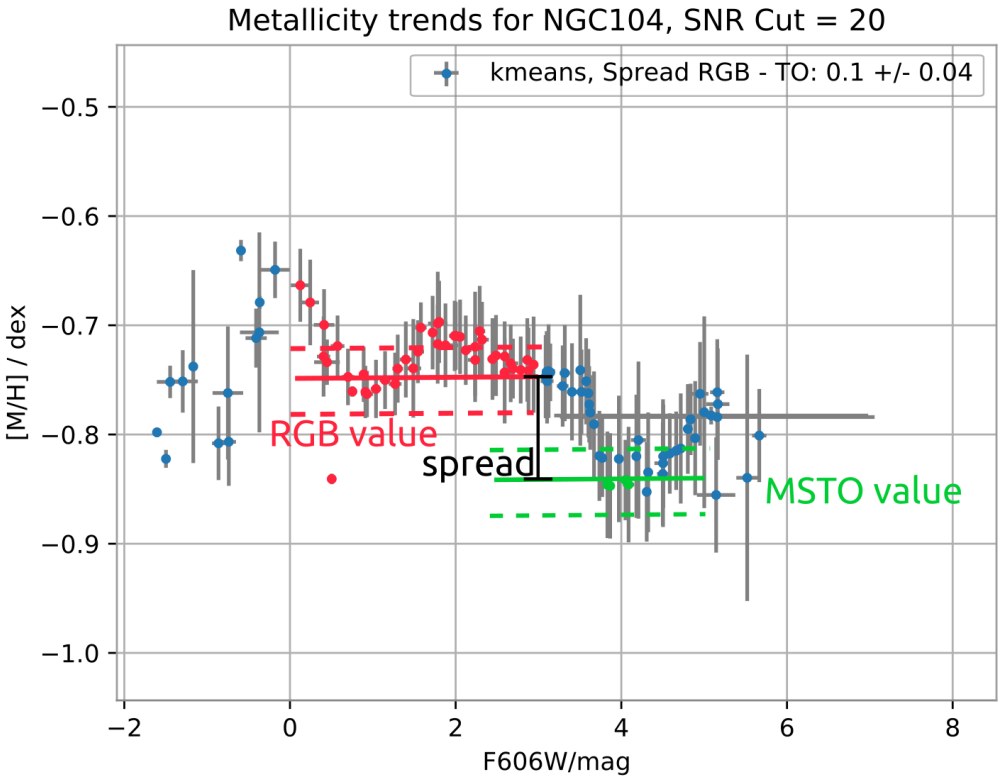

Figure 4.4.: Example for the calculation of the metallicity spread. The red dots are the values which are considered for the calculation of the RGB metallicity, the green dots for the turnoff metallicity, while the solid lines are the respective average values and the dashed lines are the uncertainties.

difficult to determine as it is unclear if one single bin represents the correct value at the turnoff. So the turnoff value is determined by taking the weighted average of the n lowest values at the approximate turnoff position, where n is a compromise between having enough values to meet the turnoff value and not too many values from main sequence or SGB which would introduce a bias towards higher turnoff values. $n = 4$ was found to be a reasonable number. Figure 4.4 illustrates this process.

The errors of RGB and turnoff metallicity are calculated from the single RGB values and the n smallest turnoff values, respectively, using equation 4.4.

The spread is then calculated as the difference between RGB and turnoff value while its error is the root of the quadratic sum of the two errors.

This method is a measure for a lower boundary of the maximum metallicity spread

in the cluster assuming the initial metallicity is restored on the red giant branch (cf. section 2.3) while it ignores the actual shape of the trend as well as the trend on the main sequence.

5. Metallicity Trends in Globular Clusters

In this chapter the resulting metallicity trends obtained from the methods described in Section 4.2 are presented. These trends are analysed in detail for three example clusters, namely NGC 104 ([Fe/H]=-0.72), NGC 3201 ([Fe/H]=-1.59) and NGC 7099 ([Fe/H]=-2.27), where the metallicities are taken from Harris (2010). These three clusters are relatively data-rich examples of clusters of their respective metallicity, therefore they are taken as representative examples for these three classes of clusters which are high metallicity ([Fe/H]>-1), medium metallicity (-2.0<[Fe/H]<-1.0) and low metallicity ([Fe/H]< -2.0). The results for the other clusters in the survey are presented in the appendix (additional plots are shown in Appendix A while tables showing the results are shown in Appendix B).

First, the different binning methods described in chapter 4.2.2 are compared and the impact of different SNR cuts are evaluated. After that different features of the metallicity profiles in the different regions are described qualitatively before a quantitative analysis of the metallicity spreads is given and compared amongst different clusters

5.1. Comparison of binning methods

Figure 5.1 shows the results of the binning methods with fixed bin widths, fixed bin sizes, isochrone binning and k-means clustering for the cluster NGC 104. There is no qualitative difference between the binning methods. Some binning methods include less bins which is also visible from the plots in Section 4.2.2. Also quantitatively the different binning methods give the same results since the spreads between MSTO and RGB are in their mutual error intervals.

In the method with fixed bin sizes (top right panel) the stars on the RGB are binned together in relatively few bins, therefore there is only one bin for the bright

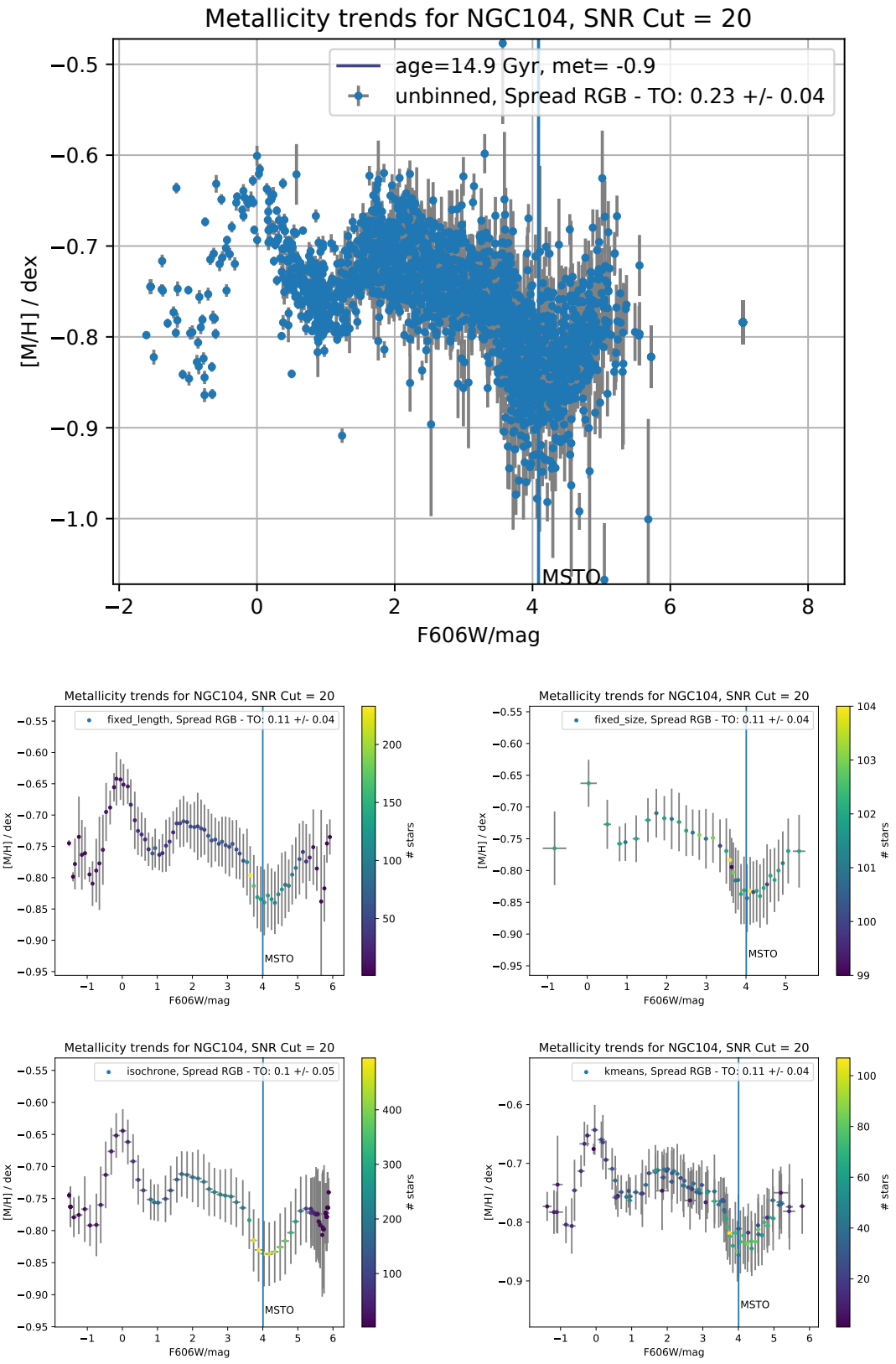

Figure 5.1.: Metallicity profiles for NGC 104 for different binning methods, all with SNR cut 20. The vertical line denotes the MSTO as determined from the CMD.

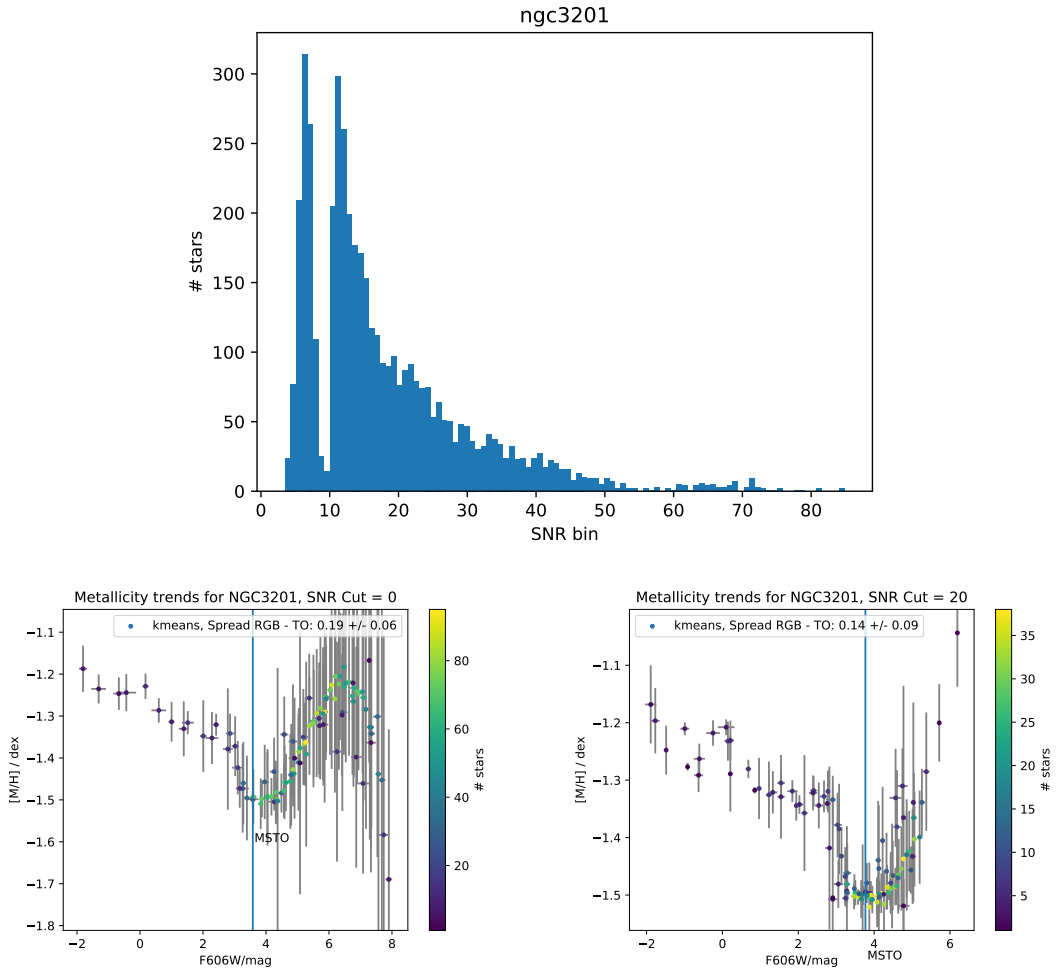

Figure 5.2.: **Upper panel:** Distribution of SNR across the stars in NGC 3201. **Lower panel:**Comparison of metallicity profiles using different SNR cuts. The vertical line denotes the MSTO.

end, while the other methods show much variation in this area. Since the isochrone method (bottom left panel) is highly dependent from the choice of the isochrone and the isochrone rarely fits well along the whole CMD, there are always areas in which only few stars (down to one) are binned into one single bin (cf. Fig 4.2).

In the lower panel of figure 5.2 the results are shown for two different SNR cuts. It is visible that the SNR cut mostly affects the main sequence as many stars in this area have a low SNR and are therefore excluded. In the exampe it seems that the metallicity tends to decrease for some bins on the main sequence. Nevertheless, the MSTO, SGB and RGB are basically the same except for smaller error bars in bins on the bright end which are on the one hand due to smaller bins and therefore

less deviation inside the bin, on the other hand stars with higher SNR have lower intrinsic errors in metallicity.

Taking these results together with the considerations from section 4.2.2 into account the k-means method was chosen as the most appropriate method. The method is independent from an isochrone which is a heavy issue of the isochrone method. All further results are mainly based on this method. Furthermore a SNR cut of 20 was chosen because it is a compromise between excluding too many stars (cf. Figure 5.2, upper panel) and therefore have bins with too less stars and taking into account too many bad quality spectra whose metallicity measurements are not reliable. However, for some clusters no MSTO was visible at a SNR cut of 20, therefore in these clusters lower SNR cuts were taken into account.

5.2. Inspection of peculiar regions

In this section the metallicity trend on the main sequence, the main sequence turnoff, the subgiant branch and the red giant branch is described and compared between a low, a medium and a high metallicity cluster. Furthermore the behaviour is compared with predicted models from MIST isochrones (section 2.3).

5.2.1. Main sequence

On the main sequence the uncertainties in [M/H] are very large, therefore a quantitative analysis of the metallicity trends down to such faint magnitudes is very difficult. Nevertheless it can be observed that the metallicity decreases with increasing brightness.

In all three clusters in Figure 5.3 it can be observed that the observed trend on the main sequence is steeper than predicted from the isochrone. It is also visible that the highest metallicity stars on the main sequence have higher metallicities than the stars on the RGB despite the fact that these – according to isochrones – have masses of about 0.6-0.7 $M_{\odot}$ and therefore shouldn't have their original metallicity visible on the surface (cf. Section 2.3).

Unfortunately, there is not enough data for all the clusters on the MS to be analysed at sufficient SNR. For this reason not all plots in Appendix A show a main sequence. In the tables shown in Appendix B the column "MS vis?" denotes if the trend on the main sequence is visible in the respective cluster. The definition of

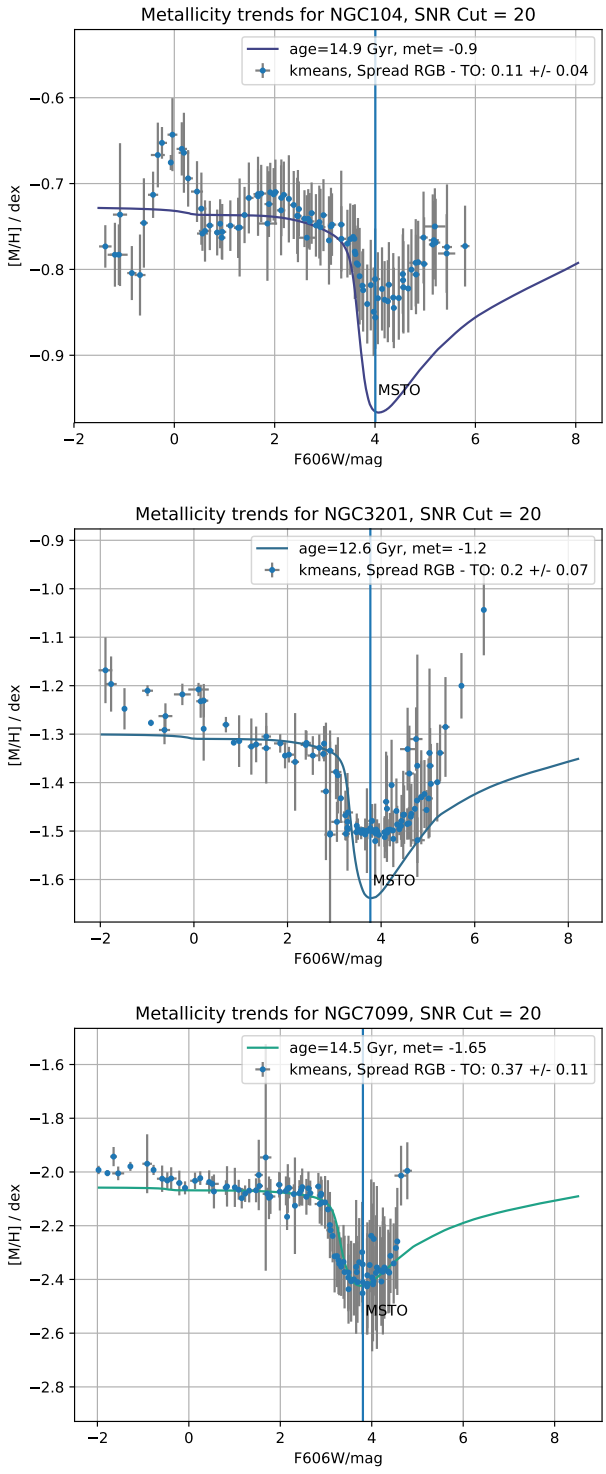

Figure 5.3.: Comparison between a high metallicity (NGC 104, [Fe/H]=-0.72, top), a medium metallicity (NGC 3201, [Fe/H]=-1.59, middle) and a low metallicity cluster (NGC 7099, [Fe/H]=-2.27, bottom). The binning method is kmeans method, the SNR cut is 20. In every plot a MIST isochrone is overplotted, where the isochrone parameters are determined by isochrone fitting as described in Section 4.2.1 and given in table 4.2. The isochrones are shifted in y-direction in order to fit the average RGB metallicity.

visibility of the trend on the MS is that the maximum value in metallicity below the MSTO is at least in the confidence interval of the RGB metallicity value.

5.2.2. Main sequence turnoff

The general definition for the MSTO is the bluest point on the main sequence. However, this definition is sometimes hard to apply since the turnoff often is not clearly defined, but a broad region in the CMD, where the transition between MS, MSTO and SGB stars is fluent. Therefore, there is not one single MSTO bin which makes it difficult to define the actual turnoff metallicity. In the magnitude-metallicity diagrams like those in Figure 5.3 the MSTO as determined from the bluest bin in the kmeans method is marked with a vertical line.

Besides, in some clusters at high SNR cuts the data only reach to the bright parts of the MSTO, therefore there is not enough data to reliably determine a turnoff metallicity. However, for the plots in Appendix A the SNR cuts are chosen s.t. for each cluster at least the MSTO is visible.

In the tables in Appendix B the column "MSTO sep?" denotes if the metallicity of the MSTO is significantly below the metallicity on the RGB, i.e. if the significance intervals of the two values (c. Figure 4.4) do not overlap.

5.2.3. SGB

The SGB is a very steep region in the metallicity-magnitude diagram, as the luminosity does not change very much while the metallicity is almost completely restored during this phase. The spread is quantified using the method described in Section 4.2.4.

This behaviour is qualitatively in accordance with the behaviour predicted by the isochrones as seen in Figure 5.3. Quantitatively, this metalicity spread is overestimated by the isochrone in most clusters while this overestimation gets smaller at lower metallicity clusters.

5.2.4. RGB

In the plots in Figure 5.3 and Appendix A the isochrone is shifted in y-direction s.t. the average metallicity on the RGB is the same for the isochrone and the observed data.

On the RGB the metallicity is predicted to basically stay on a constant plateau with a slight increase in the brighter region due to the first dredge-up where material from the core get to the surface (cf. Section 2.3).

While in some clusters the plateau of constant metallicity is observed in accordance with the isochrone, in most clusters a significant rise in metallicity is also observed which exceeds the increase predicted from the isochrones. In the tables in Appendix B the column "RGB inc?" denotes if such a significant increase is observed.

However, while most clusters show a – more or less – monotonous increase in metallicity on the RGB, there are few clusters (NGC 104, NGC 6441 and NGC 6624) where the metallicity fluctuates on the upper RGB, i.e. decreases, increases and decreases again (except for NGC 6441 where there is no first decreasing phase). The three clusters where this behaviour occurs are the highest metallicity clusters in the sample with metallicities of -0.72 dex, -0.46 dex and -0.44 dex.

5.3. Overall Analysis

As described in section 4.2.4 the difference between the RGB and the MSTO can be measured in each cluster where suffcient data is available. The resulting metallicity differences are plotted against original metallicity taken from Harris (2010) in Figure 5.4. Also plotted are metallicity differences obtained from MIST models where the MS metallicity is the minimum metallicity and the RGB metallicity is the maximum metallicity on the RGB.

In the plot a clear trend for decreasing metallicity spread with increasing original cluster metallicity is visible, as predicted from stellar modeling. In the plot the corresponding spreads from MIST isochrones are also visible. The Pearson correlation coefficient[1] for the spreads of the isochrone calculations is -0.92 while for the observtions it is -0.75. However, the spreads predicted by the isochrones are systematically larger than the observed spreads.

There is one cluster which clearly stands out, as it has the largest spread as a medium metallicity cluster. This cluster is NGC 5139 (ω Centauri) which is known to be a very peculiar cluster. Not only because it is the largest known globular cluster in the Milky Way with a mass of $5 \times 10^6 M_\odot$ but also because its large spread

[1]The Pearson correlation coefficient is a measure for correlation between two variables, where 0 means no correlation, +1 means perfect positive correlation and -1 means perfect negative correlation

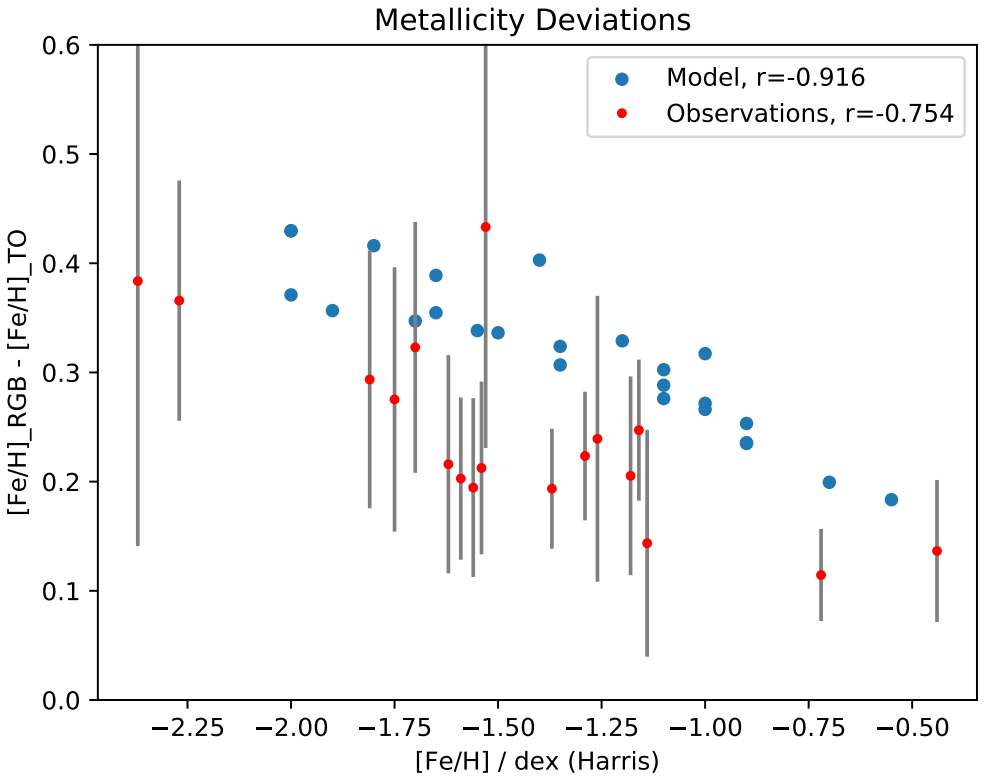

Figure 5.4.: Metallicity spreads of all clusters where a separation between RGB and MSTO is visible. The blue points denote values for different MIST isochrones. The metallicity on the x-axis denotes the Harris metallicity (Harris, 2010) for the observations and the original metallicity for the models. The metallicity spread on the y-axis is calculated using the method described in section 4.2.4. The results are from the kmeans method with SNR cut 20.

in metal abundance and the complex structures in metal abundances. The reason for this complex structure is not yet known. Either could it be a general property of very massive GCs or it is a very peculiar property of this special cluster, as several mechanisms have been proposed, e.g. that ω Cen is the merger of two clusters or it is a nucleus of a dissolved dwarf galaxy (Gratton et al., 2004).

6. Conclusions

In this chapter the problems occured using the methods described in Chapter 4.2 as well as possible physical interpretations of the results described in Chapter 5 are discussed. Furthermore an outlook on which research could be further performed on this field is given.

6.1. Discussion of the Method and the Results

6.1.1. Problems

One of the core problems of this work is to find the most suitable method to bin the stars together. Four different methods are tried out and despite the disadvantages of the method (a random initial configuration, a lack of overlapping bins) the k-means method is identified as the best of the considered methods.

It can not be taken for granted that this is indeed the best possible method to perform this task. For example a density-based clustering algorithm like DBSCAN could have been used, in contrast to the centroid-based k-means method. However, there is no large difference, neither qualitatively nor quantitatively between the methods, therefore the result should not be heavily dependent on the chosen binning method.

Another problem is the calculation of average metallicity for the MSTO and the RGB which is crucial in order to quantify the spread of metallicity. As the transitions between the several evolution stages in the isochrone are fluent, it is not possible to assign stars doubtlessly to single evolution stages. Therefore it is not clear if the calculation of average metallicity for the different stages takes all of the respective stars into account. The method described in Section 4.2.4 tries to make sure that only stars on the respective evolution stage are taken into account.

A problem which has not been addressed in this work is the reliability of the metallicity values themselves. The method how to determine those metallicities is

briefly described in Section 4.1.2. It relies on a full spectrum fit to model spectra which has its limitations when applying to mid-resolution spectra like those obtained with the MUSE instrument. Therefore the reliability of metallicities is questionable. Another method to determine metallicities – at least for stars on the RGB – makes use of a CaT-metallicity relation which is calibrated on MUSE data by Husser et.al (in prep.).

6.1.2. Comparison with previous studies

Of the 25 clusters covered in this work, two were also subject of study in one of the AD studies mentioned in Chapter 3, namely NGC 7099 (M 30) and NGC 6752.

In NGC 6752, Gruyters et al. (2014) observed weak abundance trends of about 0.1 dex in single element abundances of several elements, namely Mg (0.11 ± 0.12 dex), Ca (0.11 ± 0.06 dex), Ti (0.09 ± 0.06 dex) and Fe (0.08 ± 0.05 dex), between MSTO and RGB while in the present study a spread in metallicity of 0.21 ± 0.08 dex was observed. Therefore the spread observed in the present study is about as twice as large as in the previous study, yet the uncertainties in both studies are relatively large, which is why the respective uncertainty intervals overlap. However, an overall metallicity is not the same as single element abundances, therefore it is questionable if those values can be compared at all.

Gruyters et al. (2016) observe a spread in iron abundance of about 0.32 dex between MSTO and RGB in NGC 7099 while in the present study a metallicity spread of 0.37 ± 0.11 dex is observed. This is in good agrement with each other. Nevertheless, a single element abundance is compared with an overall metallicity.

Besides, the previous studies used a NLTE analysis of the spectra which could at least explain part of the difference (cf. Section 3.5).

6.1.3. Physical Interpretation of the Results

It is very satisfying that the overall trend in metallicity can be observed in every cluster and also that the metallicity spread tends to decrease with increasing overall metallicity (Section 5.3). This is in very good agreement with predictions from stellar evolution modeling (Section 2.3).

The result that the available models overestimate the observed trends is also qualitatively in aggreement with theoretical explanations, as the models do not take into account additional mixing effects which are present below the convection zone

and extend the mixing zone.

A feature which is not as good to explain is the increase in metallicity on the RGB which is present in almost every cluster. Although such an increase is predicted by models (first dredge-up), the observed increase exceeds the predicted by about one order of magnitude (the typical predicted increase is 0.01 dex while the typical observed increase, if present, is roughly 0.1 dex). A feature which can not be explained by models at all is the fluctuation in metallicity on the RGB for the high metallicity clusters NGC 104, NGC 6441 and NGC 6624. Also, the highest main sequence metallicities seem to be higher than RGB metallicities, which has no reasonable physical explanation, but could be explained by the fact that the spectrum fit misidentifies some noise as metal lines which systematically increases the metallicity in low-SNR spectra which are more present on the MS.

6.2. Outlook

This study did only provide a glimpse on what is possible with MUSE data applying to AD studies. It clearly confirmed the trend that the metallicity spread increases with decreasing metallicity and it gave strong hints for the development of the trend on the main sequence, but a coherent quantitative analysis is still missing.

The reason for this is the lack of models since it was out of scope of this work to calculate new models but the results only are compared with calculations available on the web. In future works new models should be calculated from scratch using different turbulence models as well as radiative levitation. Using those models the results presented in this work could indeed put constraints on the parameters used in the models. Rudimentary calculations with the MESA code were also tried out. The results are shown in Figure 6.1. As can be seen from the plots, there are two main issues with these calculations. First, in some models, there are sharp edges in the metallicity trend which should not occur in nature, even if the trend is very steep. Second, the metallicity spread is larger in the model with lower initial metallicity which contradicts the findings from above. It is not said, that this is impossible, however, before such an endavour should be trusted, it needs more careful examination. These issues lead to the conclusion that these models can not yet be trusted.

If the models improve in further studies, it could also make sense to apply fitting functions to the observed models in order to quantitatively compare the trends and

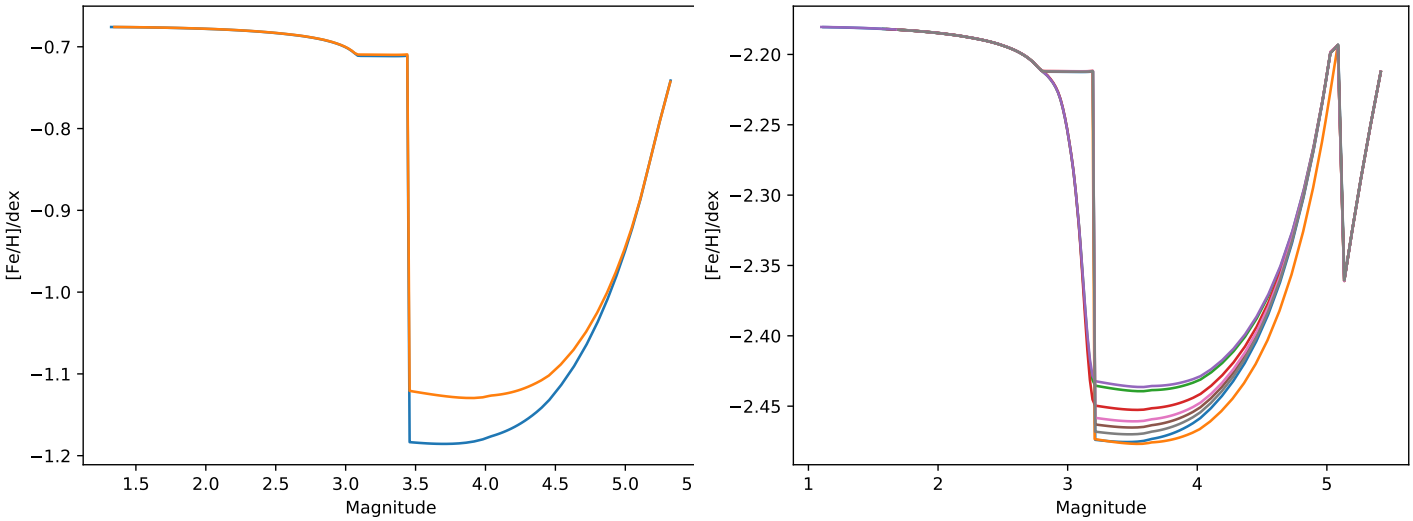

Figure 6.1.: Results of MESA calculations. In the left panel two models with an initial metallicity of -0.6 dex, in the right panel 8 models with an initial metallicity of -2.1 dex are plotted. In both cases the initial stellar mass was 0.75 $M_{\odot}$ which corresponds to a turnoff age of about 13.5 Gyrs. The models differ in a certain mixing parameter which is a free parameter describing additional mixing and which is differed between 1 and 2.

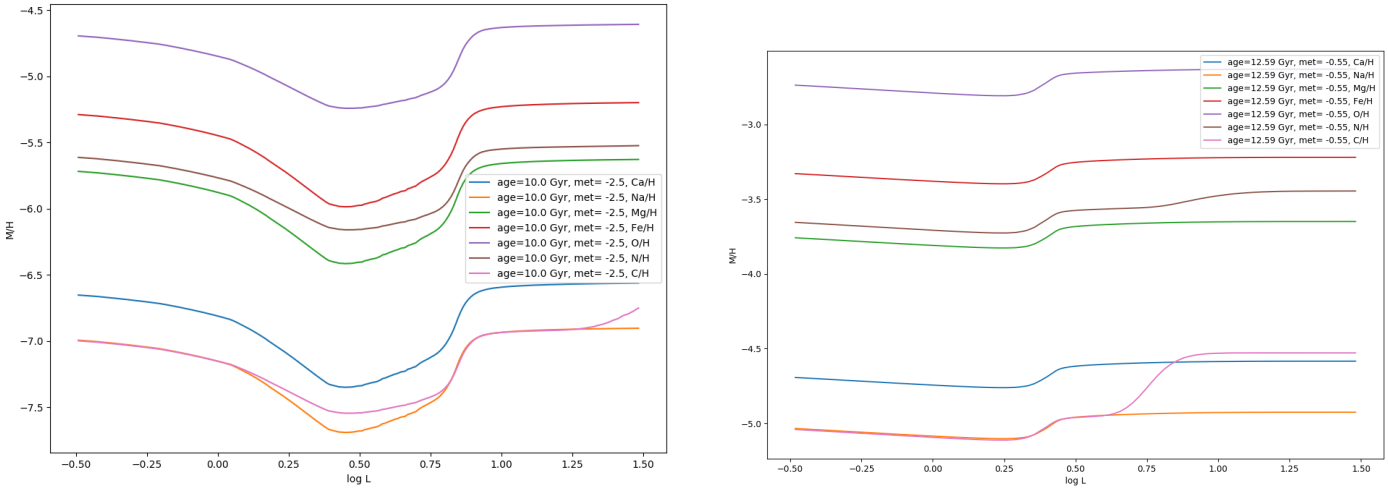

Figure 6.2.: Single element abundances in 7 different elements in MIST isochrones for two different metallicities: -2.5 dex on the left and -0.55 dex on the right side.

the models beyond the size of the spread between MSTO and RGB.

Systematic single element abundance analyses could also be perfomed. Actually the resolution of the MUSE spectrograph is too low for this, but with a new approach (Latour et al., submitted) developed to analyse element abundances in RGB stars it might be possible to analyse element abundances of stars on the SGB down to the MSTO. Those results could be used to further constrain the models which are also calculated for single elements (cf. Figure 6.2).

In the future there will be new data by making deep field observations of globular cluster centers, for example of the cluster NGC 104 (47 Tucanae). Using these observations many fainter stars can be taken into account. The faintest stars which are considered in the analyses with SNR cut 20 have an absolute magnitude of about 5, which refers to a stellar mass of about 0.6-0.7 $M_{\odot}$, depending on the assumed age and metallicity of the isochrone. In order to observe stars which are fully convective, i.e. stars with masses of less than 0.35 $M_{\odot}$ (cf. Section 2.3), stars of magnitude 9 should be taken into account. With these stars the main sequence down to fully convective stars can be analysed. If such very faint stars could be analysed in detail, they would give a very precise measurement of the original abundance of the population, in contrast to RGB stars where the surface abundance might already be polluted by the products of the core fusion.

7. Summary

In this work an analysis with the integral field spectrogaph MUSE on a sample of 25 Galactic globular clusters was performed in order to find metallicity trends between the main sequence and the red giant branch. This is – to our knowledge – the largest study on atomic diffusion in globular clusters which has been performed so far.

For every cluster several hundred up to a few thousand stars were analysed. Therefore, the difficulty of this work was to handle such a large amount of data. The approach we used was to bin the data together and analyse the binned data. Different binning methods were tried, among which the k-means clusterig algorithm proofed to be best suited for this purpose, yet the results of other binning methods did not show any qualitative differences.

A clear metallicity trend in each of the analysed clusters from the red giant branch down to the main sequence turnoff was found. For some clusters also data below the turnoff were given where a positive metallicity trend with magnitude could be observed. These metallicity trends were quantified by a number for the metallicity spread between turnoff and red giant branch. A negative correlation between size of the metallicity spread and original cluster metallicity was found.

The results were also compared to computational results of a stellar evolution code. It proved to be difficult to find the correct model for every cluster, but a rough estimation was made using isochrone fitting. The data qualitatively met the models well, although the spread seems to be systematically overestimated by the models. This might be due to some additional mixing which is not considered in the used models.

Two major deviations from the models were observed. First, the trend on the main sequence was observed to be systematically steeper than predicted in the models. Second, the metallicity seems to increase on the bright parts of the red giant branch. In both cases it is not clear yet if this observation is due to a real physical effect or if it is just a systematic error on the data.

A. Metallicity Trend plots

In this appendix the respective metallicity plots for the kmeans and the isochrone method are shown. On the left side the corresponding CMD is shown, where in the upper panel the kmeans bins are color coded and in the lower panel the isochrone bins are noted as ellipses. On the right side the resulting metallicity-magnitude diagrams are shown where the number of stars per bin is color coded and an isochrone is overplotted where the isochrone parameters are taken from Table 4.2 and are noted in the legend. Also noted in the legend is the metallicity spread between MSTO and RGB, calculated as described in Section 4.2.4.

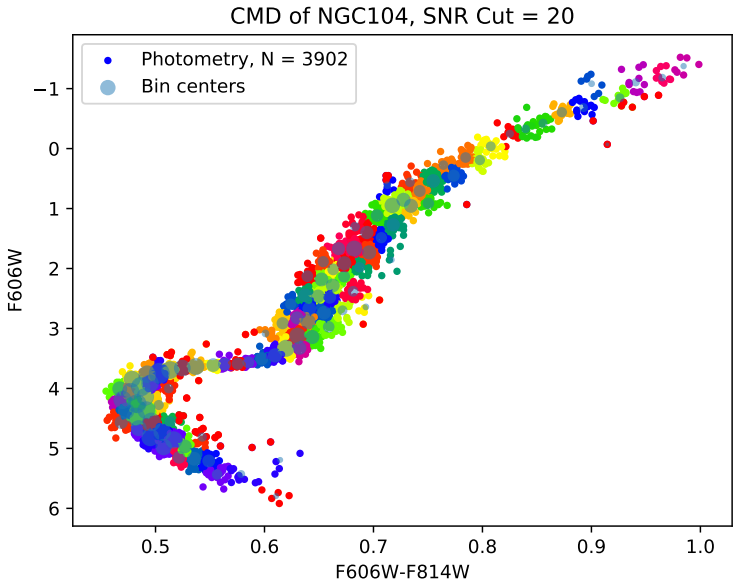
CMD of NGC104, SNR Cut = 20
Photometry, N = 3902
Bin centers
F606W
F606W-F814W

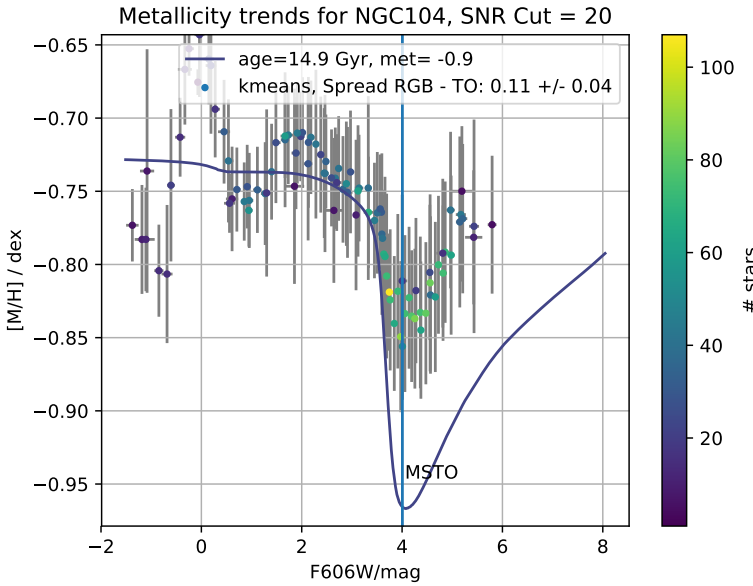
Metallicity trends for NGC104, SNR Cut = 20
age=14.9 Gyr, met= -0.9
kmeans, Spread RGB - TO: 0.11 +/- 0.04
MSTO
[M/H] / dex
F606W/mag
stars

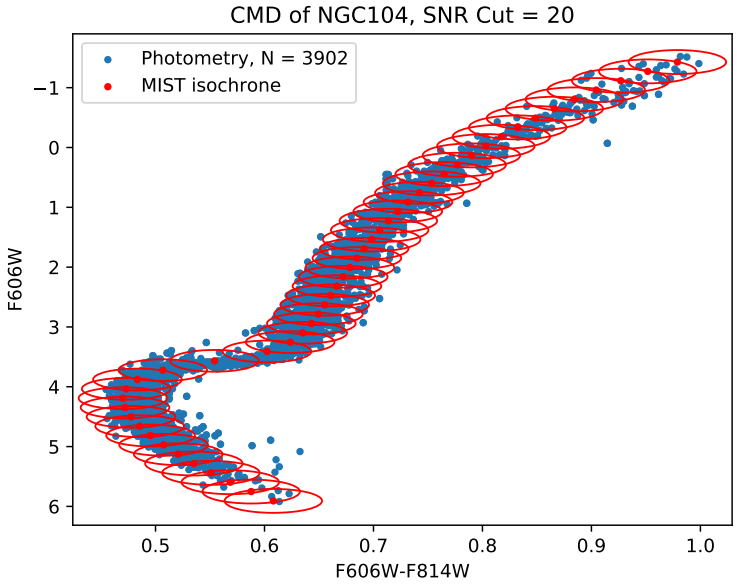
CMD of NGC104, SNR Cut = 20
Photometry, N = 3902
MIST isochrone
F606W
F606W-F814W

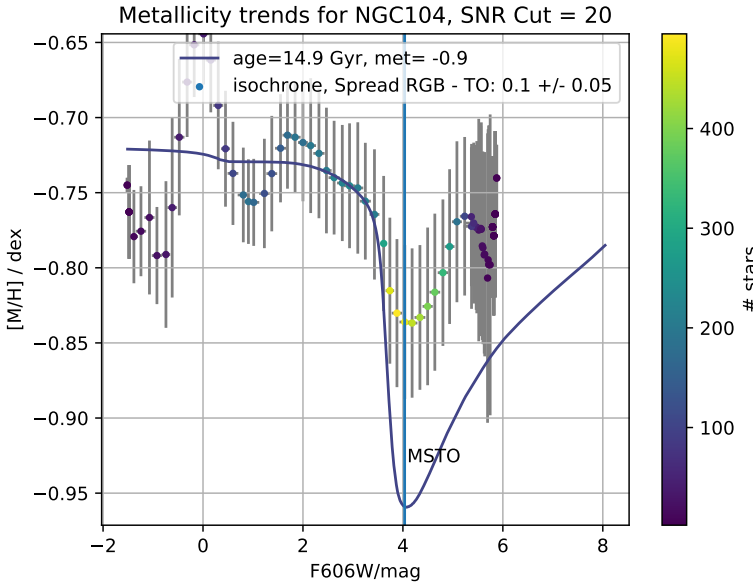
Metallicity trends for NGC104, SNR Cut = 20
age=14.9 Gyr, met= -0.9
isochrone, Spread RGB - TO: 0.1 +/- 0.05
MSTO
[M/H] / dex
F606W/mag
stars

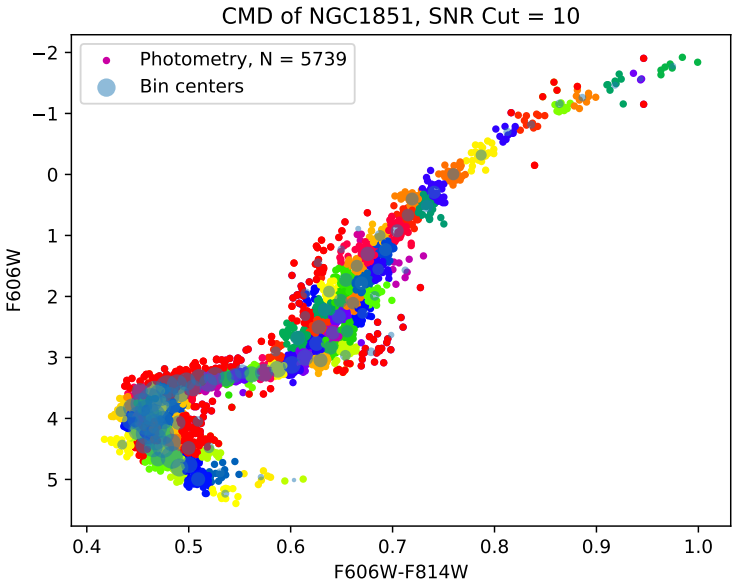
CMD of NGC1851, SNR Cut = 10
Photometry, N = 5739
Bin centers
F606W
F606W-F814W

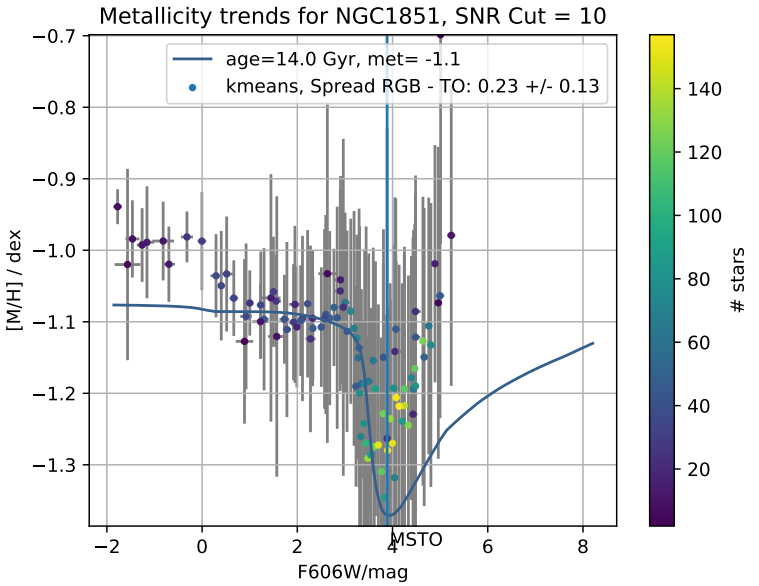
Metallicity trends for NGC1851, SNR Cut = 10
age=14.0 Gyr, met= -1.1
kmeans, Spread RGB - TO: 0.23 +/- 0.13
[M/H] / dex
MSTO
F606W/mag
stars

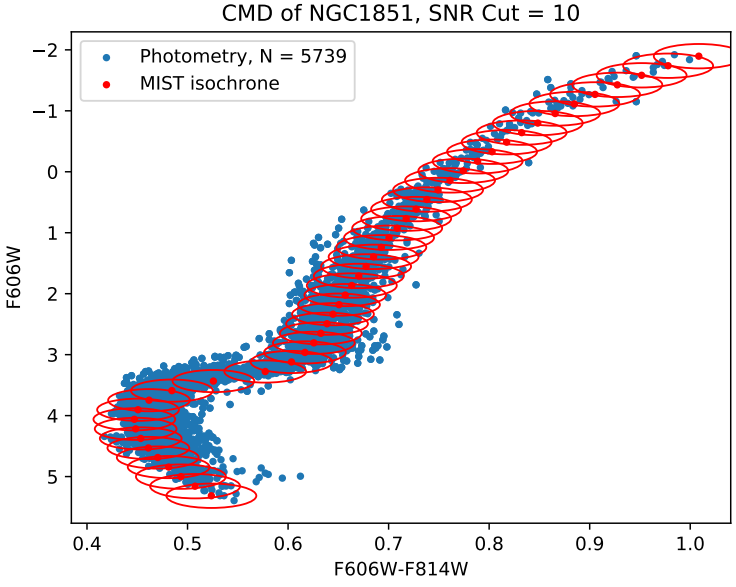
CMD of NGC1851, SNR Cut = 10
Photometry, N = 5739
MIST isochrone
F606W
F606W-F814W

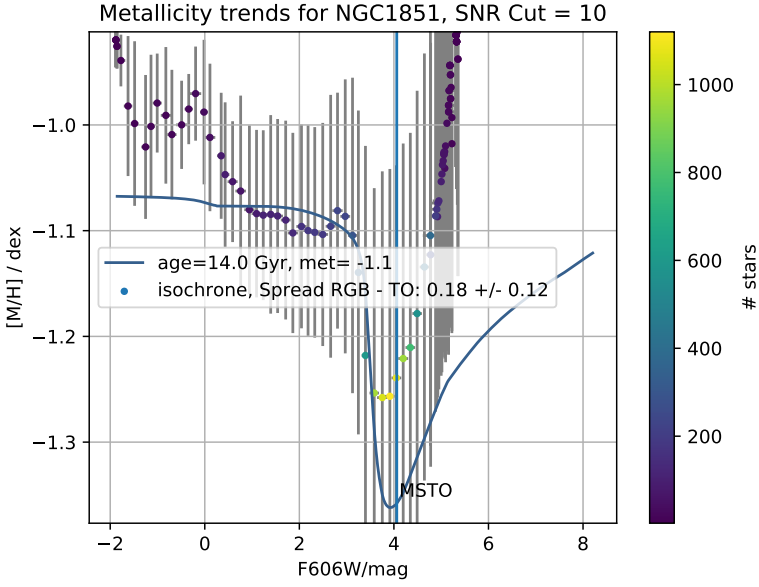
Metallicity trends for NGC1851, SNR Cut = 10
age=14.0 Gyr, met= -1.1
isochrone, Spread RGB - TO: 0.18 +/- 0.12
[M/H] / dex
MSTO
F606W/mag
stars

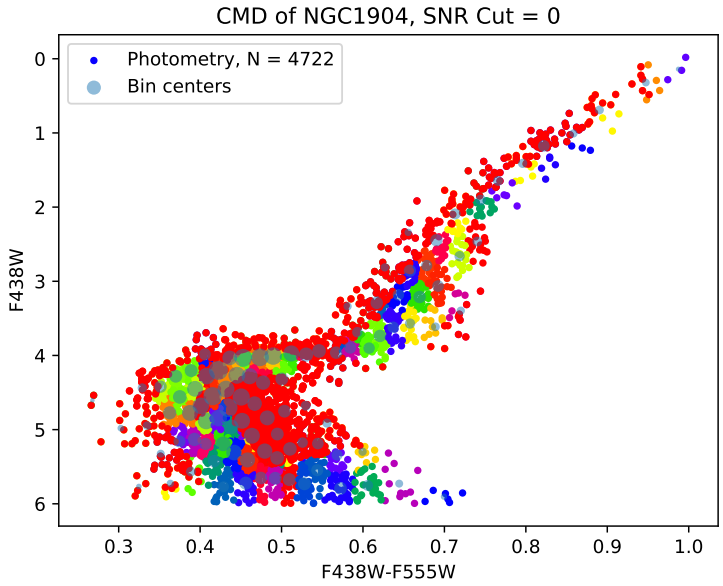
CMD of NGC1904, SNR Cut = 0
Photometry, N = 4722
Bin centers
F438W
F438W-F555W

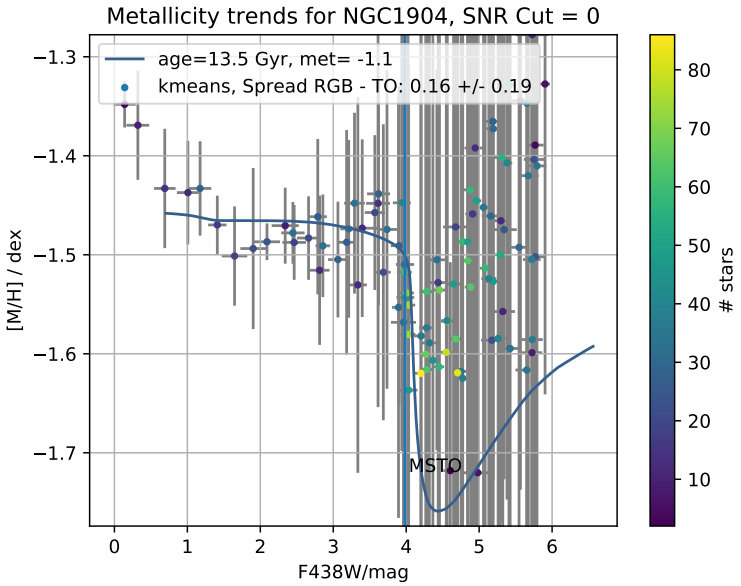
Metallicity trends for NGC1904, SNR Cut = 0
age=13.5 Gyr, met= -1.1
kmeans, Spread RGB - TO: 0.16 +/- 0.19
MSTO
[M/H] / dex
F438W/mag
stars

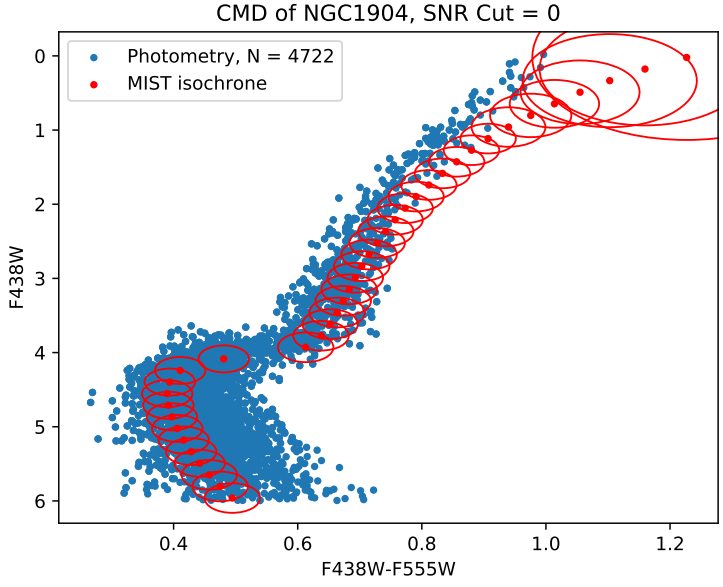
CMD of NGC1904, SNR Cut = 0
Photometry, N = 4722
MIST isochrone
F438W
F438W-F555W

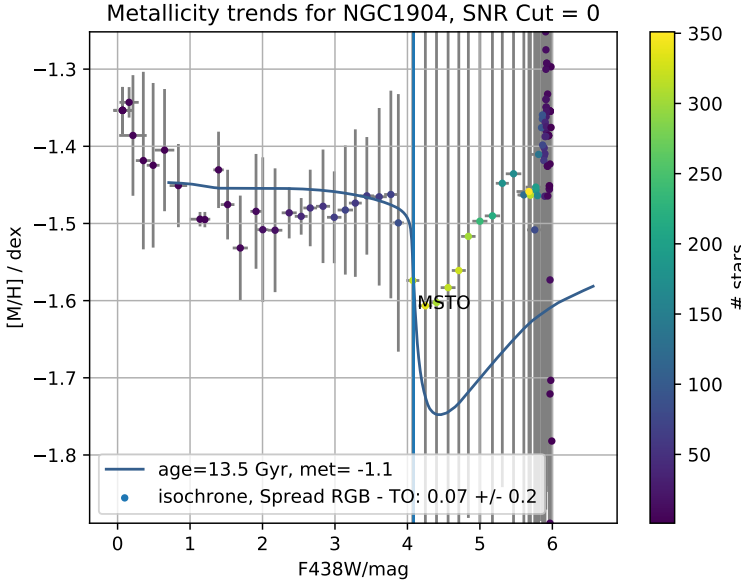
Metallicity trends for NGC1904, SNR Cut = 0
MSTO
age=13.5 Gyr, met= -1.1
isochrone, Spread RGB - TO: 0.07 +/- 0.2
[M/H] / dex
F438W/mag
stars

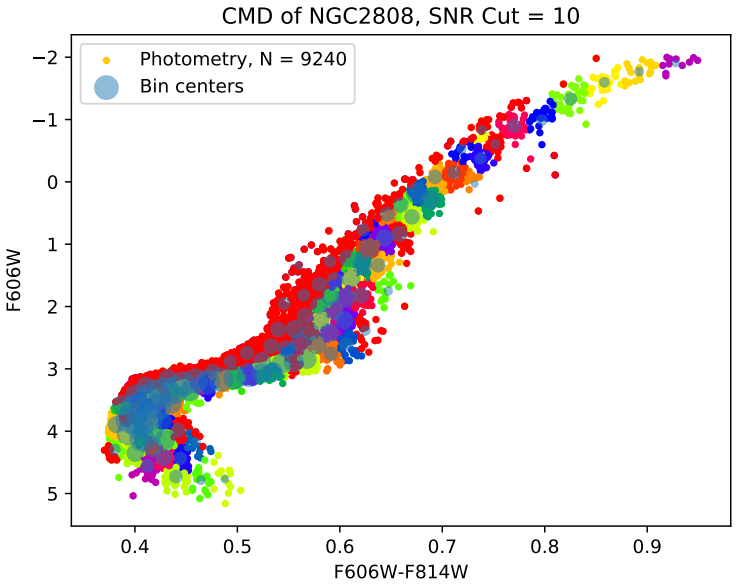
CMD of NGC2808, SNR Cut = 10
Photometry, N = 9240
Bin centers
F606W
F606W-F814W

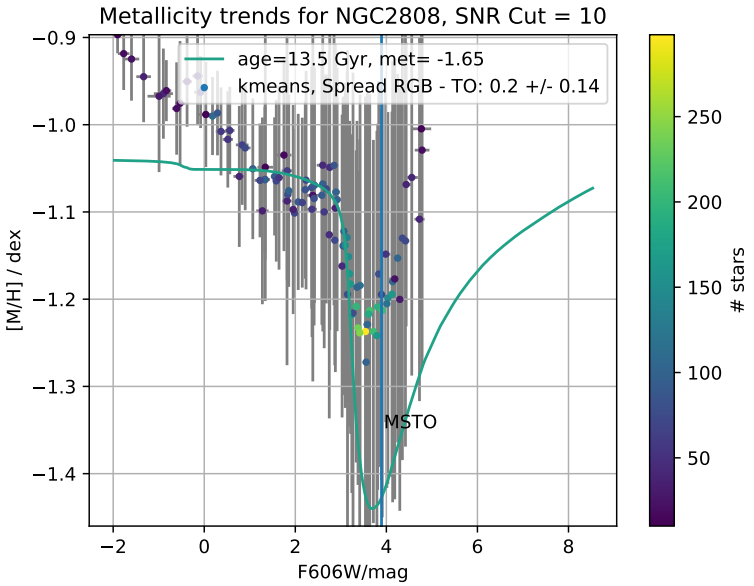
Metallicity trends for NGC2808, SNR Cut = 10
age=13.5 Gyr, met= -1.65
kmeans, Spread RGB - TO: 0.2 +/- 0.14
MSTO
[M/H] / dex
F606W/mag
stars

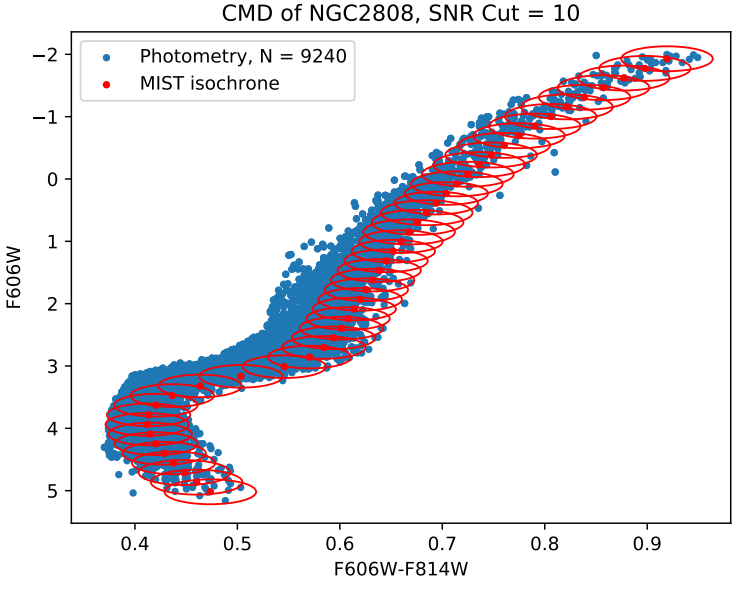
CMD of NGC2808, SNR Cut = 10
Photometry, N = 9240
MIST isochrone
F606W
F606W-F814W

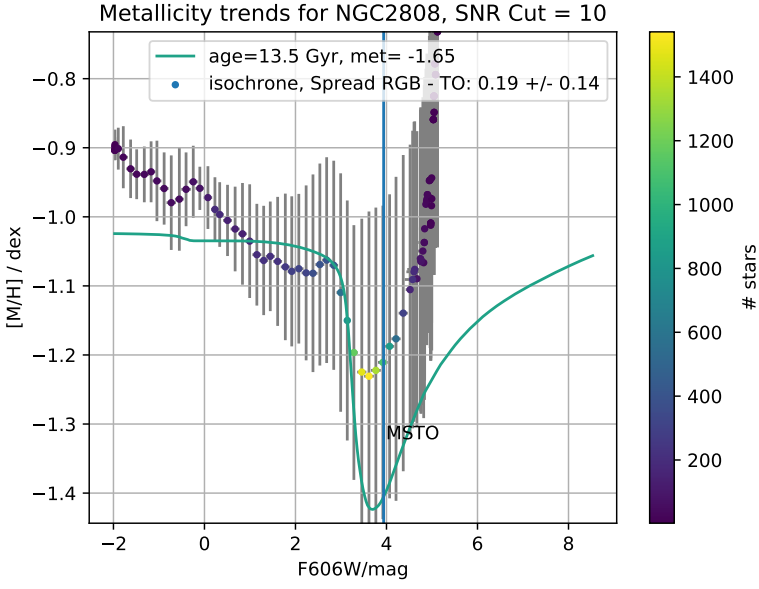
Metallicity trends for NGC2808, SNR Cut = 10
age=13.5 Gyr, met= -1.65
isochrone, Spread RGB - TO: 0.19 +/- 0.14
MSTO
[M/H] / dex
F606W/mag
stars

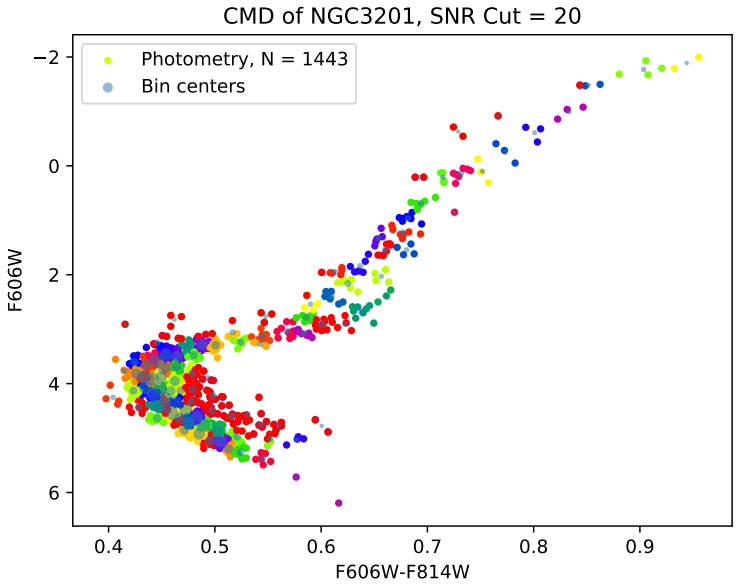
CMD of NGC3201, SNR Cut = 20
Photometry, N = 1443
Bin centers
F606W
F606W-F814W

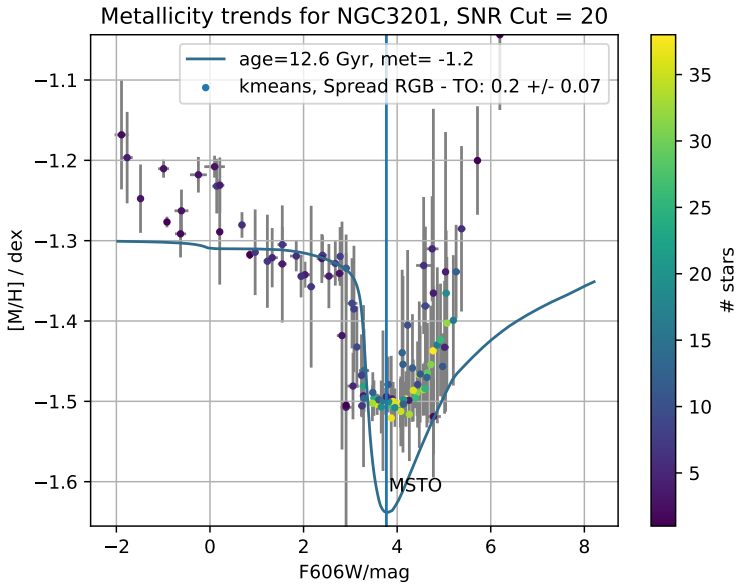
Metallicity trends for NGC3201, SNR Cut = 20
age=12.6 Gyr, met= -1.2
kmeans, Spread RGB - TO: 0.2 +/- 0.07
MSTO
[M/H] / dex
F606W/mag
stars

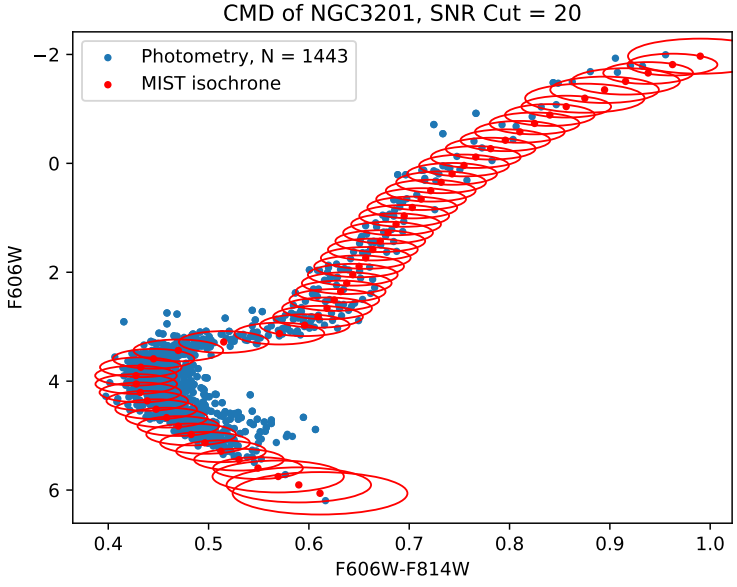
CMD of NGC3201, SNR Cut = 20
Photometry, N = 1443
MIST isochrone
F606W
F606W-F814W

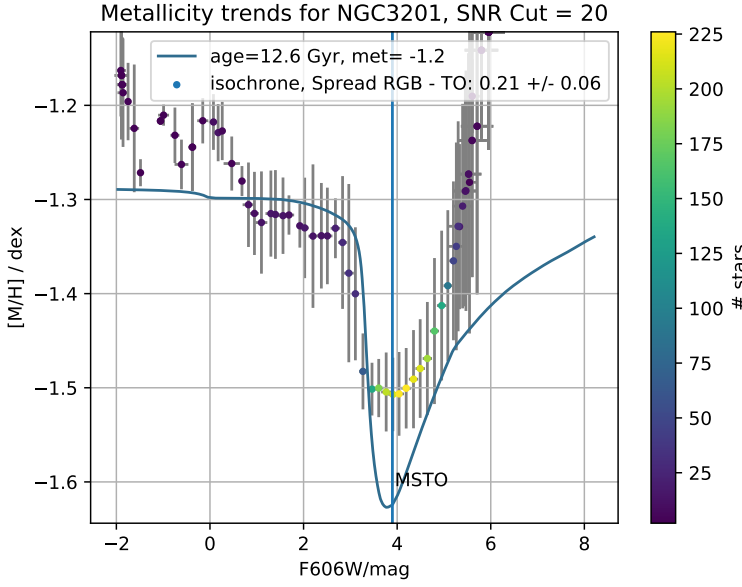
Metallicity trends for NGC3201, SNR Cut = 20
age=12.6 Gyr, met= -1.2
isochrone, Spread RGB - TO: 0.21 +/- 0.06
MSTO
[M/H] / dex
F606W/mag
stars

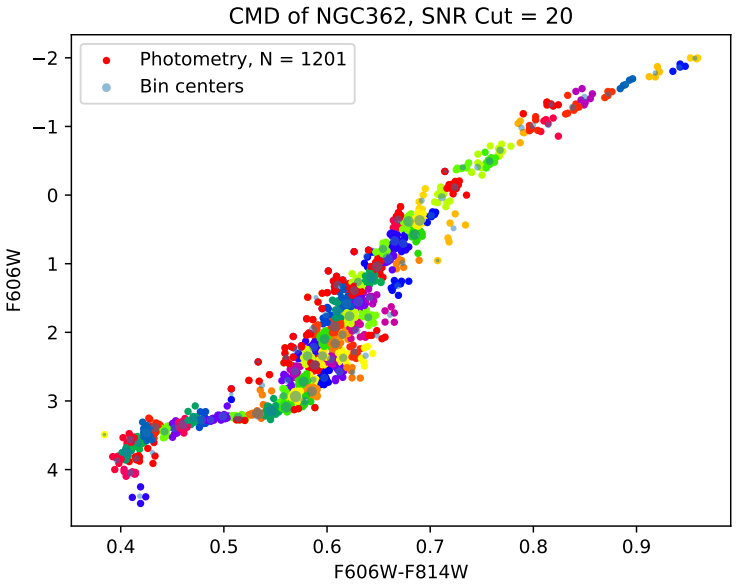
CMD of NGC362, SNR Cut = 20
Photometry, N = 1201
Bin centers
F606W
F606W-F814W

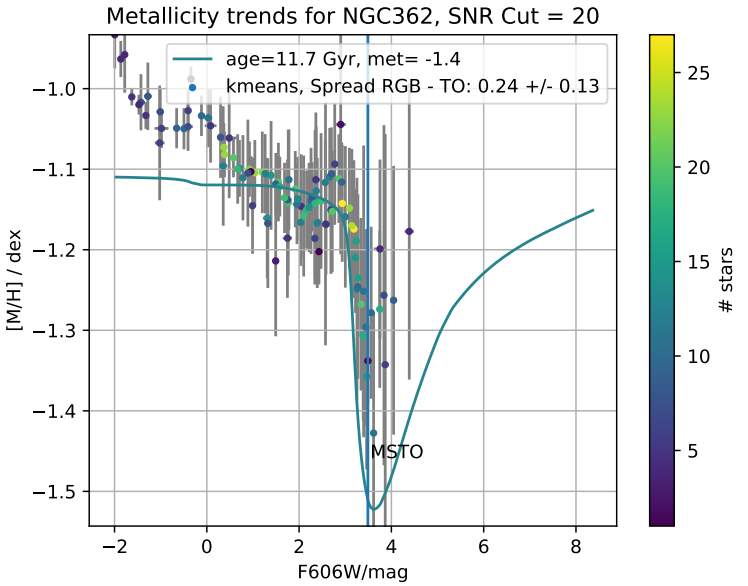
Metallicity trends for NGC362, SNR Cut = 20
age=11.7 Gyr, met= -1.4
kmeans, Spread RGB - TO: 0.24 +/- 0.13
MSTO
[M/H] / dex
F606W/mag
stars

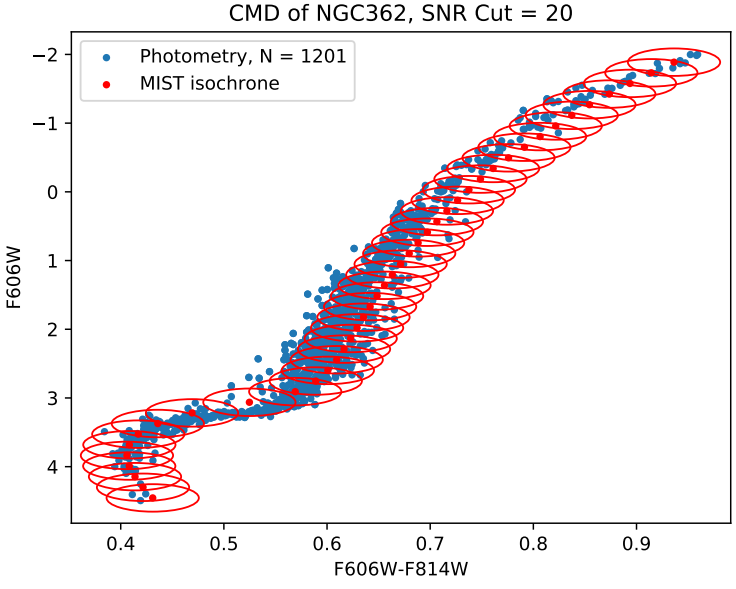
CMD of NGC362, SNR Cut = 20
Photometry, N = 1201
MIST isochrone
F606W
F606W-F814W

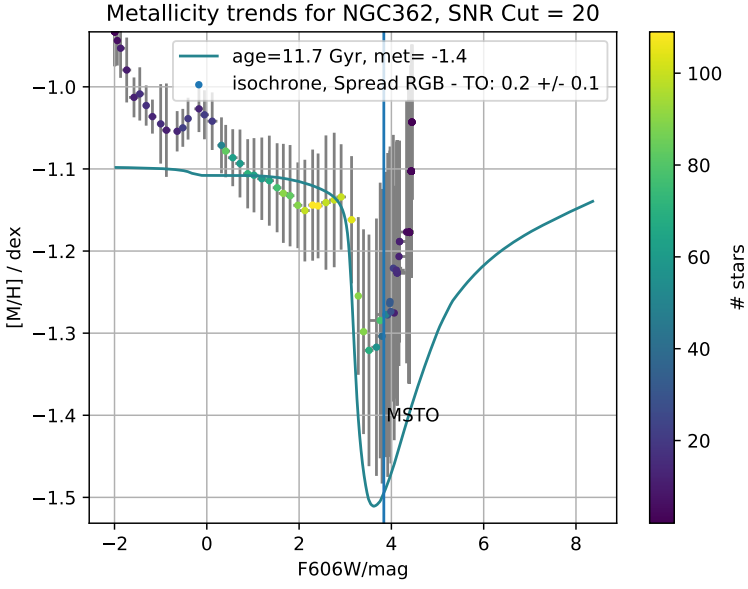
Metallicity trends for NGC362, SNR Cut = 20
age=11.7 Gyr, met= -1.4
isochrone, Spread RGB - TO: 0.2 +/- 0.1
MSTO
[M/H] / dex
F606W/mag
stars

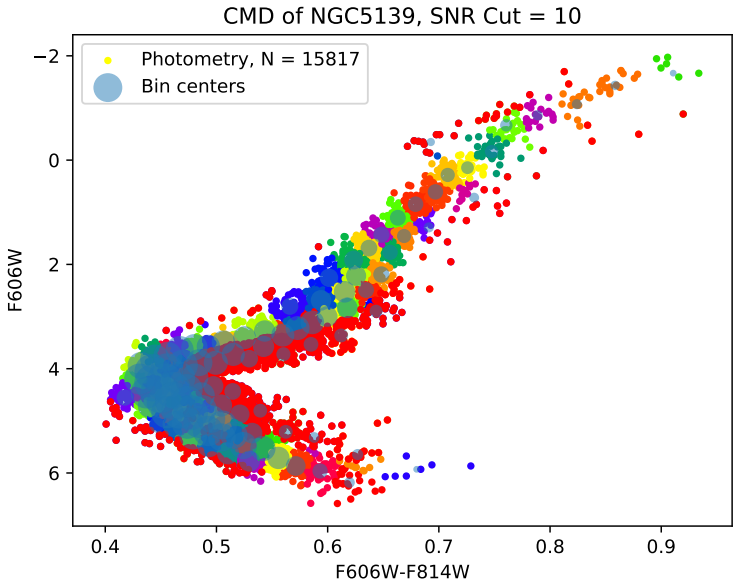
CMD of NGC5139, SNR Cut = 10
Photometry, N = 15817
Bin centers
F606W
F606W-F814W

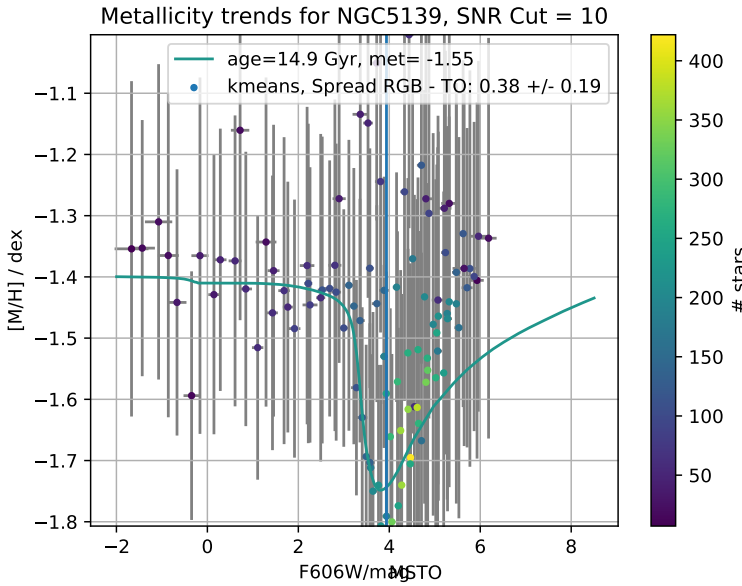
Metallicity trends for NGC5139, SNR Cut = 10
age=14.9 Gyr, met= -1.55
kmeans, Spread RGB - TO: 0.38 +/- 0.19
[M/H] / dex
F606W/mag
MSTO
stars

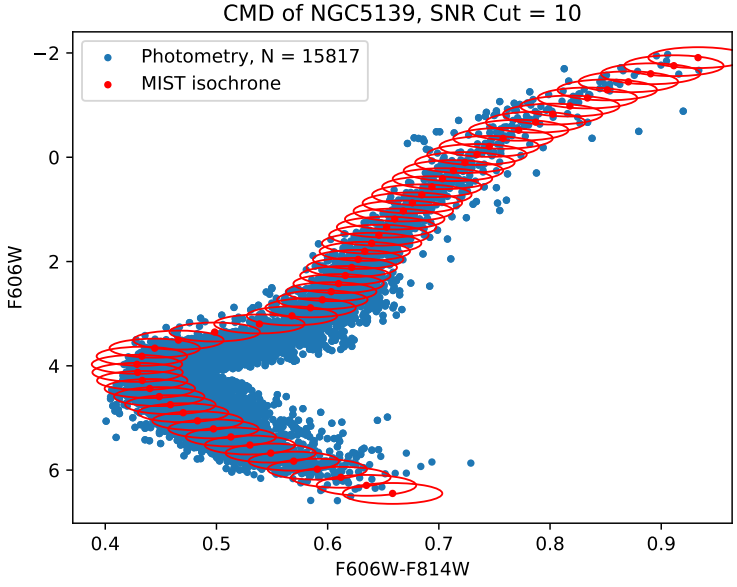
CMD of NGC5139, SNR Cut = 10
Photometry, N = 15817
MIST isochrone
F606W
F606W-F814W

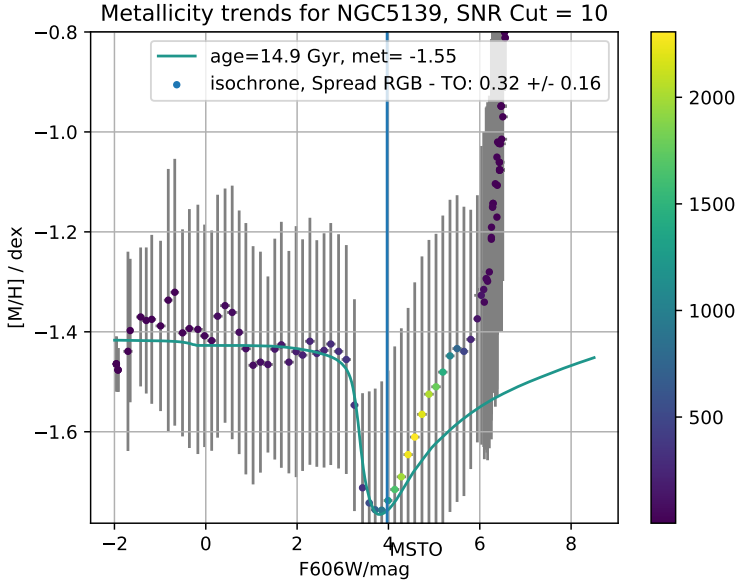
Metallicity trends for NGC5139, SNR Cut = 10
age=14.9 Gyr, met= -1.55
isochrone, Spread RGB - TO: 0.32 +/- 0.16
[M/H] / dex
F606W/mag
MSTO

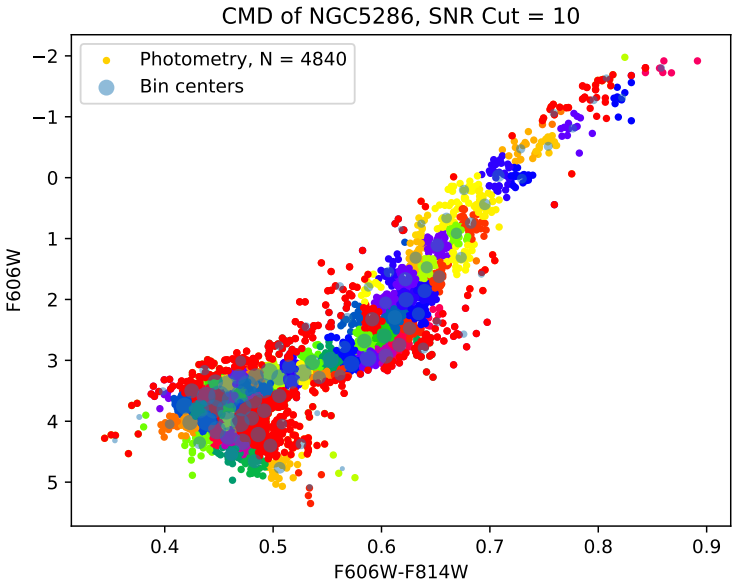
CMD of NGC5286, SNR Cut = 10
Photometry, N = 4840
Bin centers
F606W
F606W-F814W

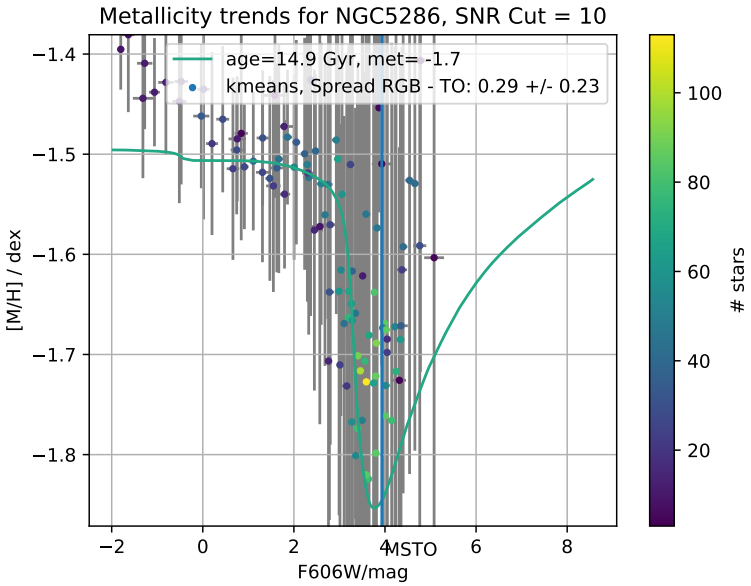
Metallicity trends for NGC5286, SNR Cut = 10
age=14.9 Gyr, met= -1.7
kmeans, Spread RGB - TO: 0.29 +/- 0.23
[M/H] / dex
MSTO
F606W/mag
stars

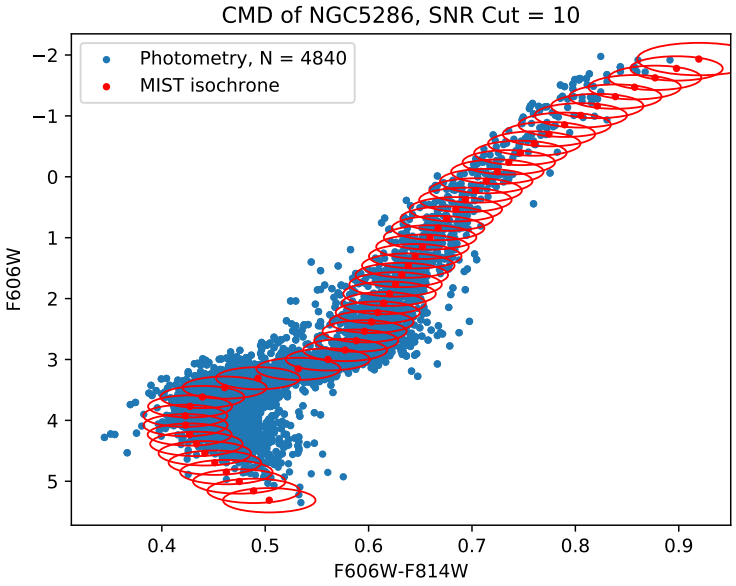
CMD of NGC5286, SNR Cut = 10
Photometry, N = 4840
MIST isochrone
F606W
F606W-F814W

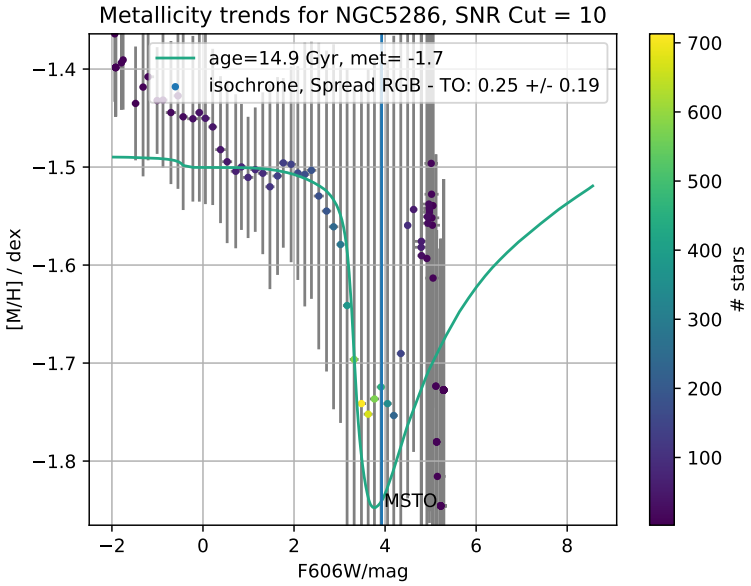
Metallicity trends for NGC5286, SNR Cut = 10
age=14.9 Gyr, met= -1.7
isochrone, Spread RGB - TO: 0.25 +/- 0.19
[M/H] / dex
MSTO
F606W/mag
stars

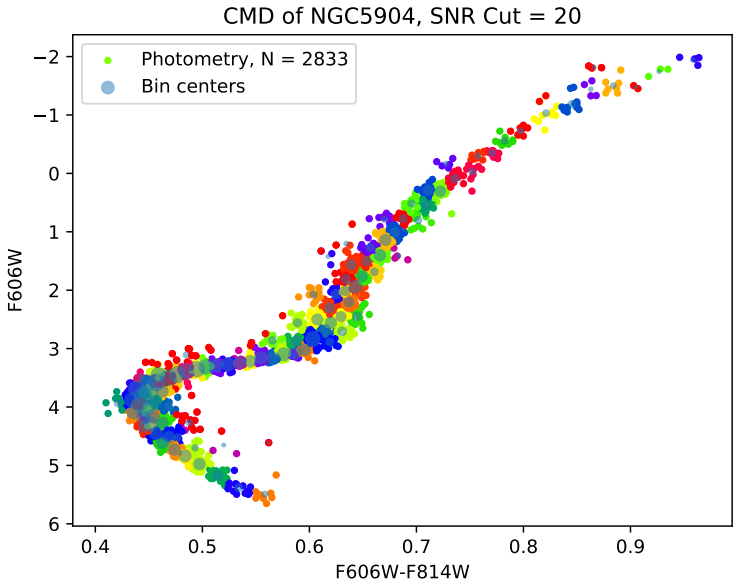
CMD of NGC5904, SNR Cut = 20
Photometry, N = 2833
Bin centers
F606W
F606W-F814W

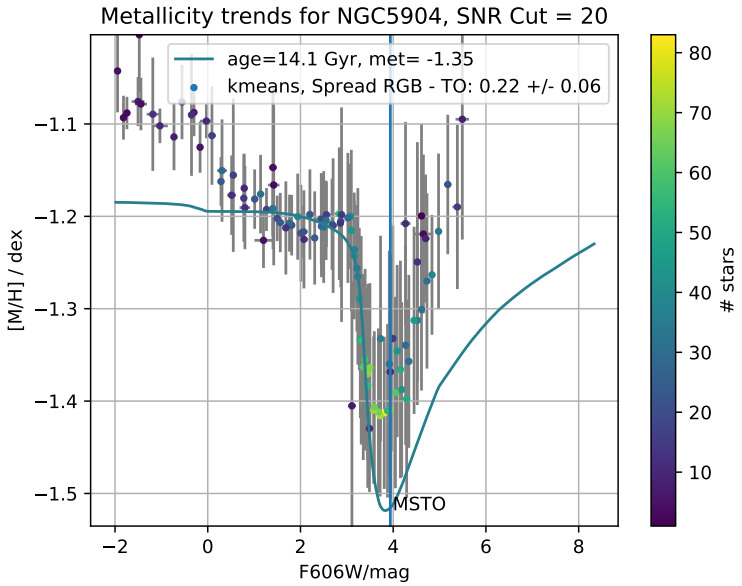
Metallicity trends for NGC5904, SNR Cut = 20
age=14.1 Gyr, met= -1.35
kmeans, Spread RGB - TO: 0.22 +/- 0.06
[M/H] / dex
F606W/mag
MSTO
stars

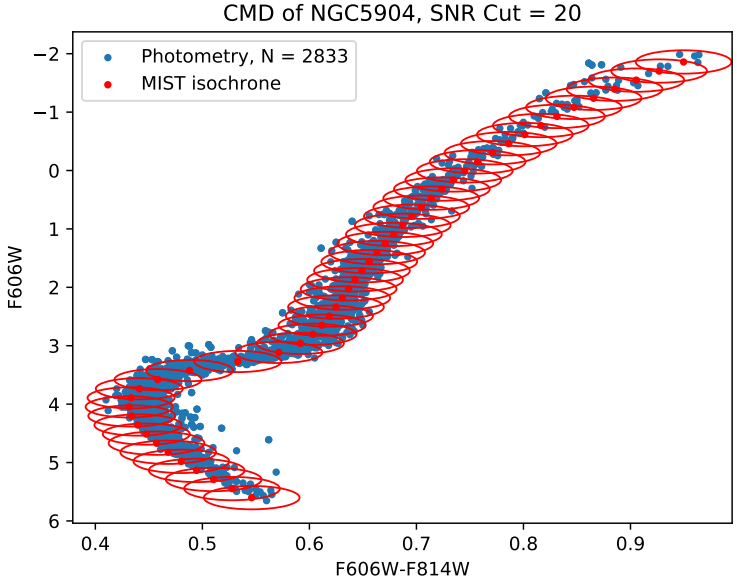
CMD of NGC5904, SNR Cut = 20
Photometry, N = 2833
MIST isochrone
F606W
F606W-F814W

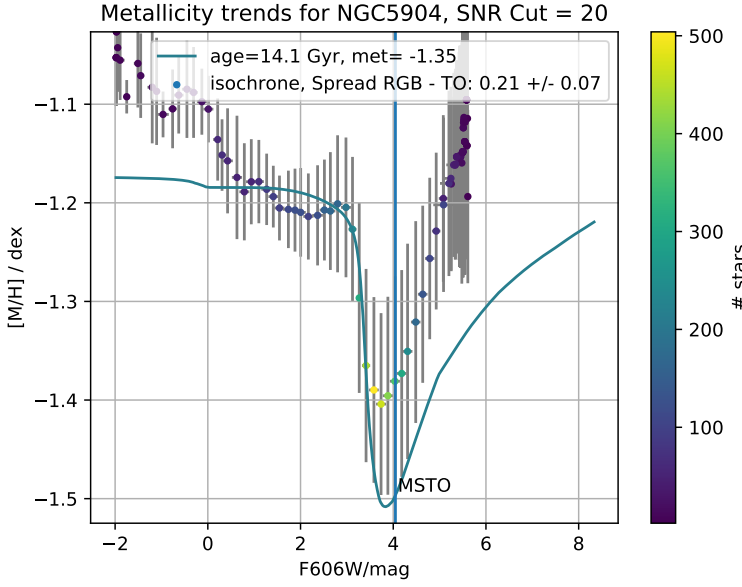
Metallicity trends for NGC5904, SNR Cut = 20
age=14.1 Gyr, met= -1.35
isochrone, Spread RGB - TO: 0.21 +/- 0.07
[M/H] / dex
F606W/mag
MSTO
stars

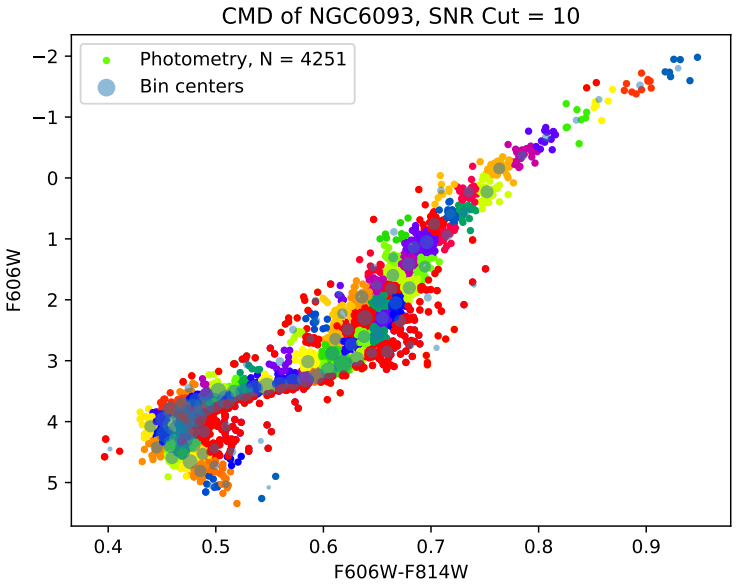
CMD of NGC6093, SNR Cut = 10
Photometry, N = 4251
Bin centers
F606W
F606W-F814W

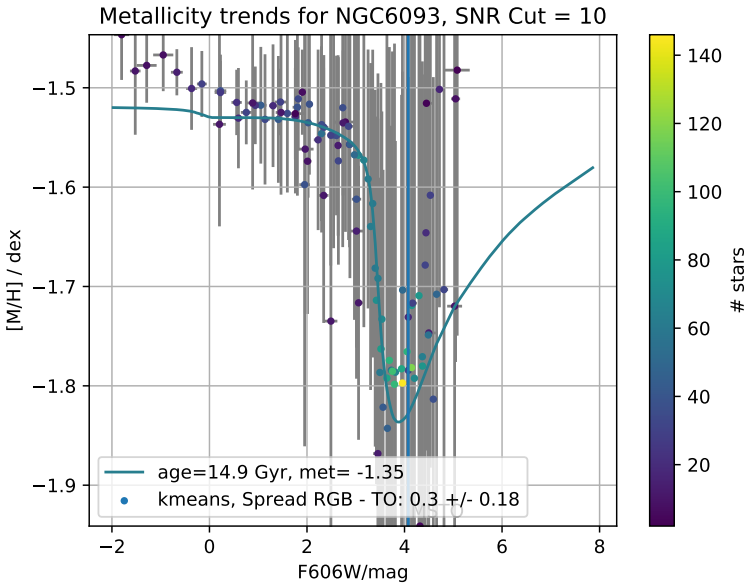
Metallicity trends for NGC6093, SNR Cut = 10
age=14.9 Gyr, met= -1.35
kmeans, Spread RGB - TO: 0.3 +/- 0.18
[M/H] / dex
F606W/mag
stars

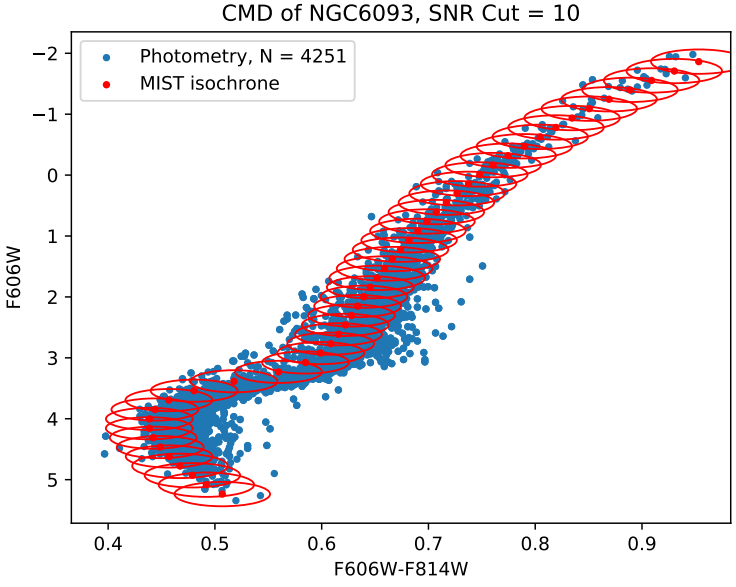
CMD of NGC6093, SNR Cut = 10
Photometry, N = 4251
MIST isochrone
F606W
F606W-F814W

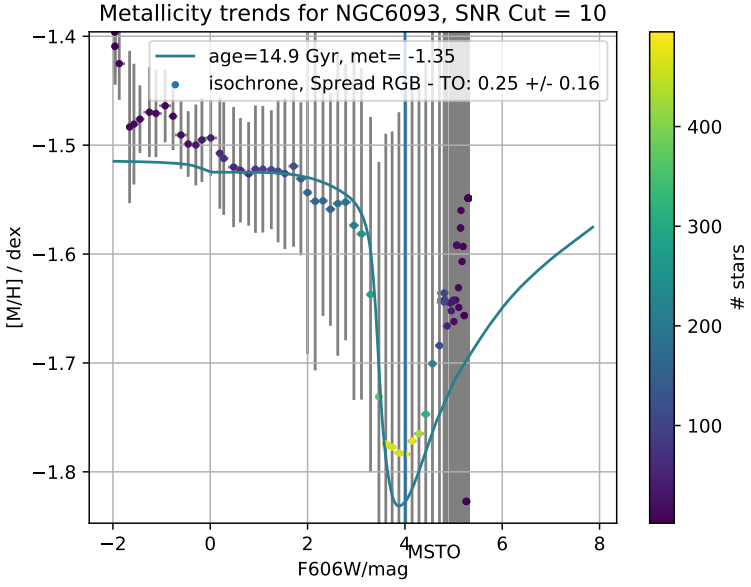
Metallicity trends for NGC6093, SNR Cut = 10
age=14.9 Gyr, met= -1.35
isochrone, Spread RGB - TO: 0.25 +/- 0.16
[M/H] / dex
MSTO
F606W/mag
stars

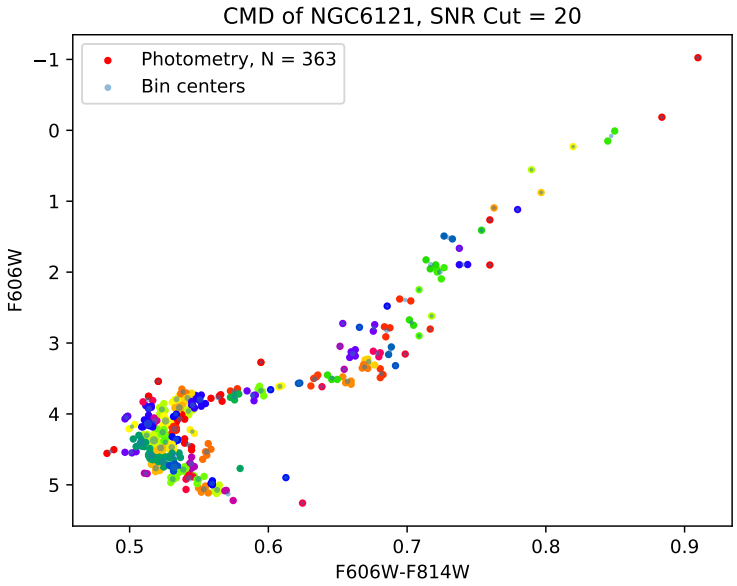
CMD of NGC6121, SNR Cut = 20
Photometry, N = 363
Bin centers
F606W
F606W-F814W

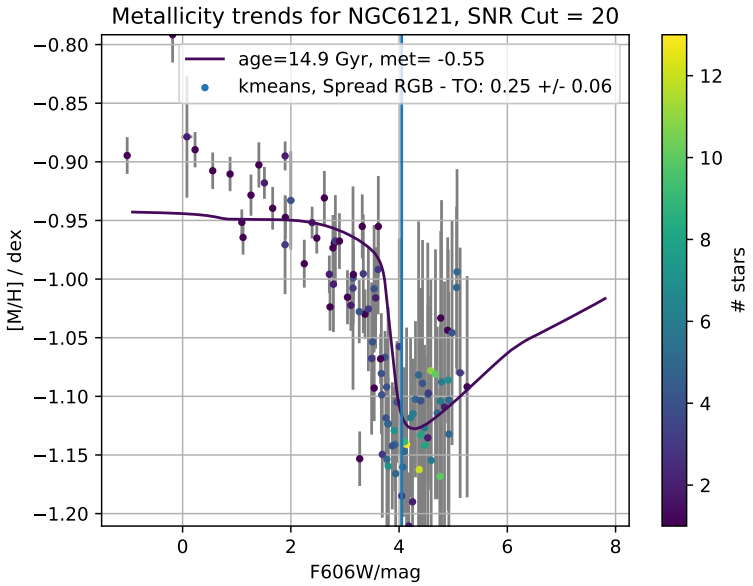
Metallicity trends for NGC6121, SNR Cut = 20
age=14.9 Gyr, met= -0.55
kmeans, Spread RGB - TO: 0.25 +/- 0.06
[M/H] / dex
F606W/mag
stars

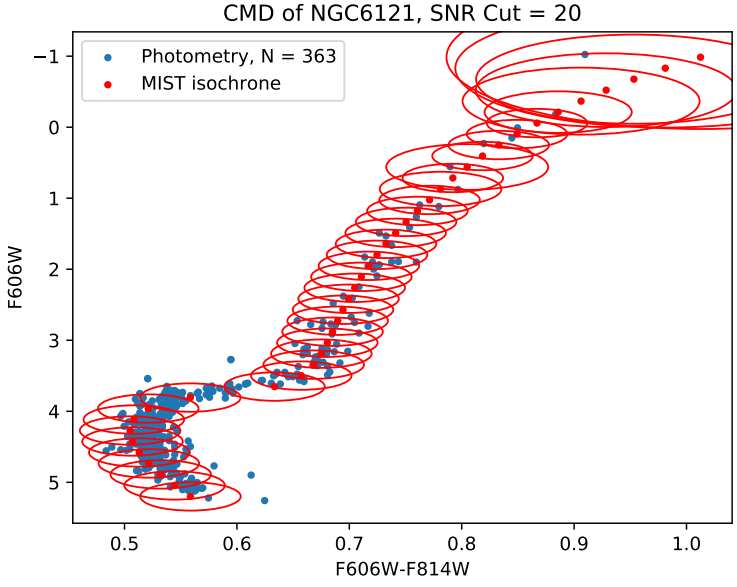
CMD of NGC6121, SNR Cut = 20
Photometry, N = 363
MIST isochrone
F606W
F606W-F814W

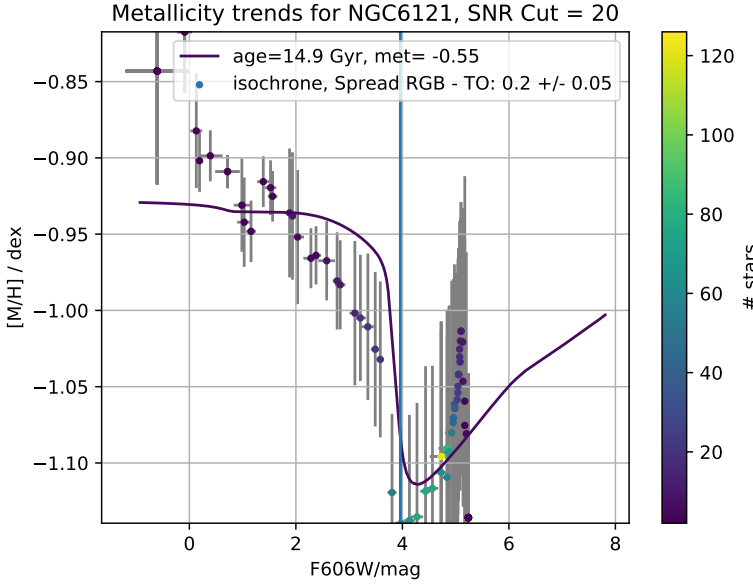
Metallicity trends for NGC6121, SNR Cut = 20
age=14.9 Gyr, met= -0.55
isochrone, Spread RGB - TO: 0.2 +/- 0.05
[M/H] / dex
F606W/mag
stars

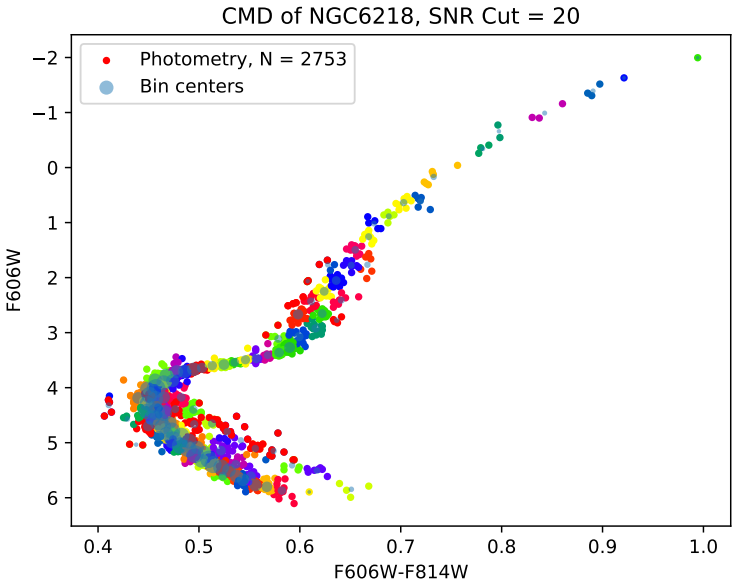
CMD of NGC6218, SNR Cut = 20
Photometry, N = 2753
Bin centers
F606W
F606W-F814W

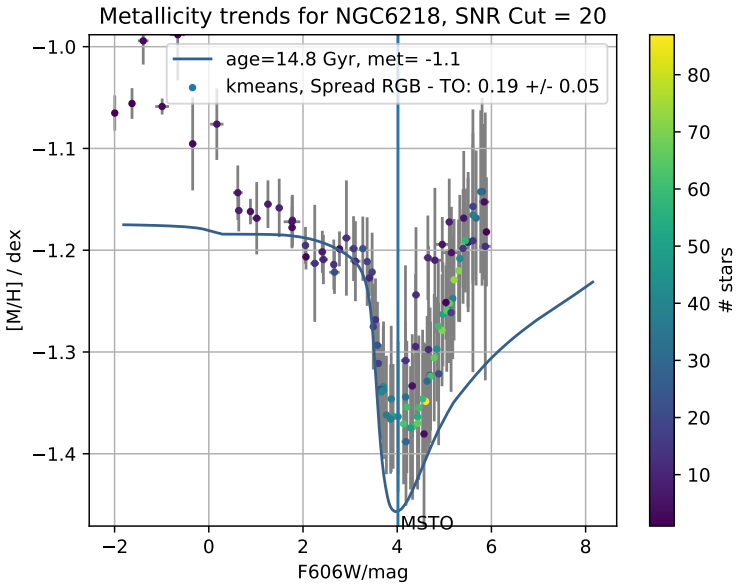
Metallicity trends for NGC6218, SNR Cut = 20
age=14.8 Gyr, met= -1.1
kmeans, Spread RGB - TO: 0.19 +/- 0.05
[M/H] / dex
F606W/mag
MSTO
stars

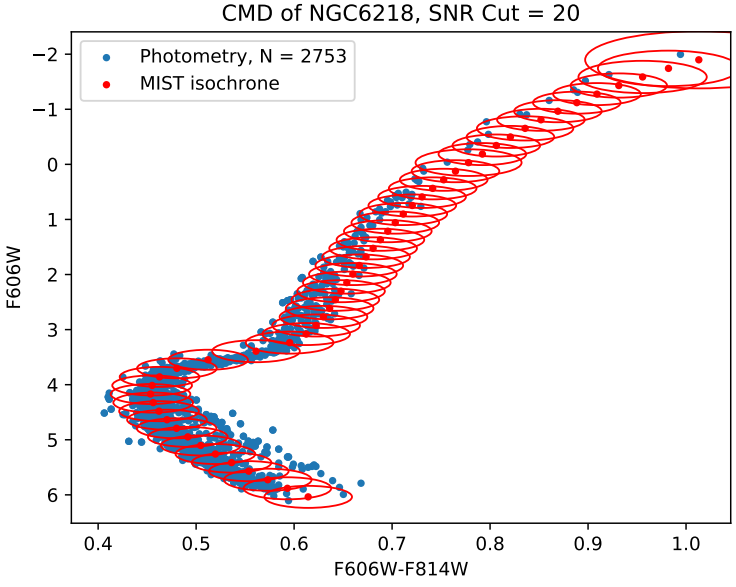
CMD of NGC6218, SNR Cut = 20
Photometry, N = 2753
MIST isochrone
F606W
F606W-F814W

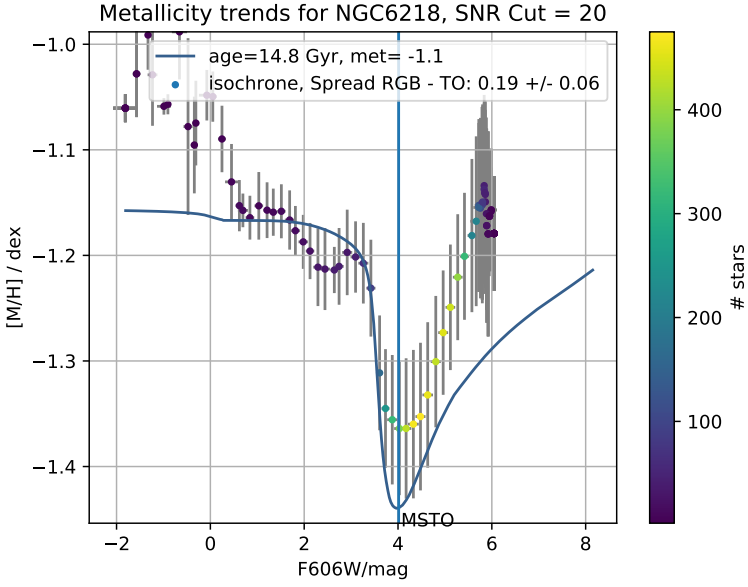
Metallicity trends for NGC6218, SNR Cut = 20
age=14.8 Gyr, met= -1.1
isochrone, Spread RGB - TO: 0.19 +/- 0.06
[M/H] / dex
F606W/mag
MSTO
stars

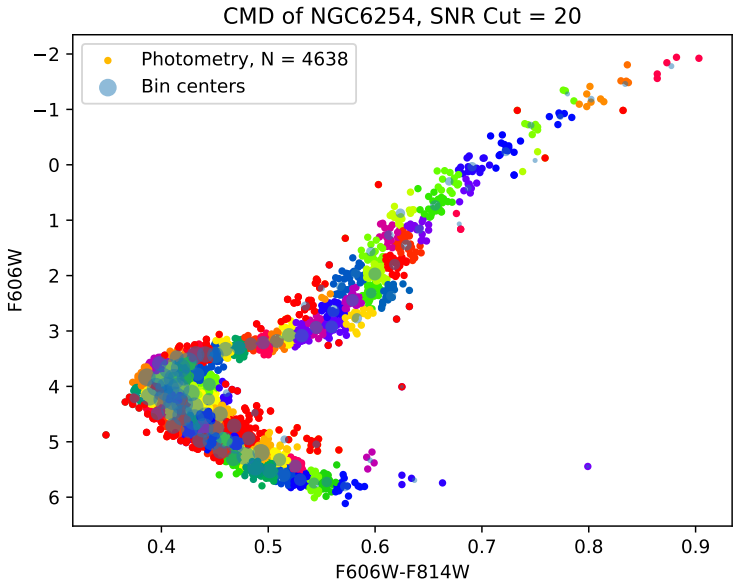
CMD of NGC6254, SNR Cut = 20
Photometry, N = 4638
Bin centers
F606W
F606W-F814W

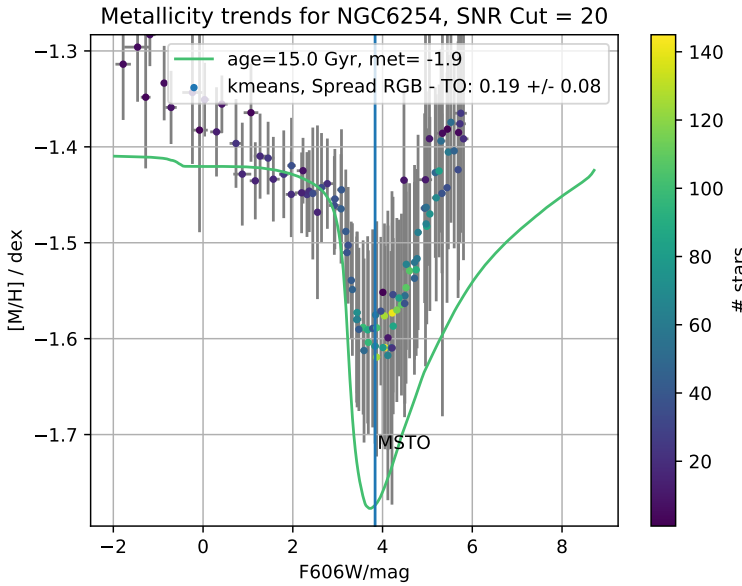
Metallicity trends for NGC6254, SNR Cut = 20
age=15.0 Gyr, met= -1.9
kmeans, Spread RGB - TO: 0.19 +/- 0.08
MSTO
[M/H] / dex
F606W/mag
stars

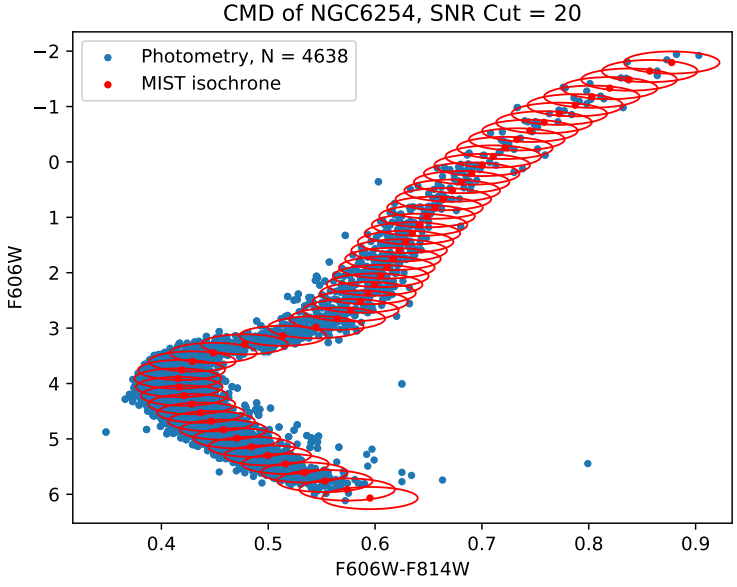
CMD of NGC6254, SNR Cut = 20
Photometry, N = 4638
MIST isochrone
F606W
F606W-F814W

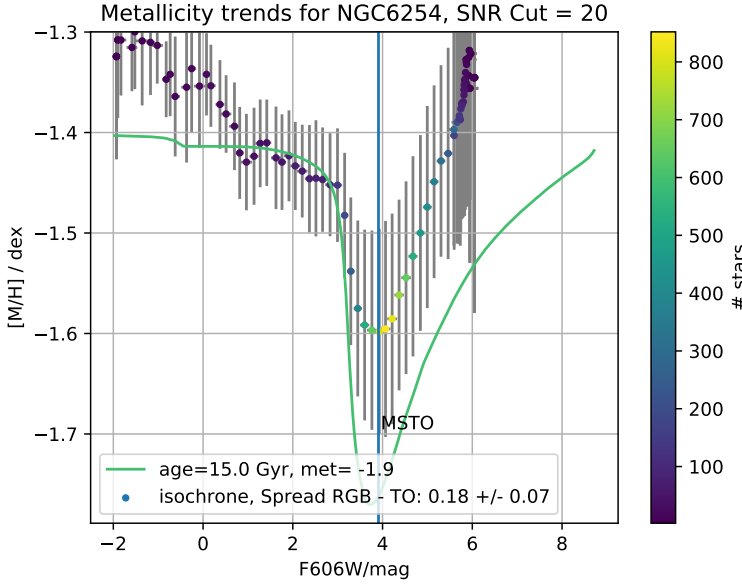
Metallicity trends for NGC6254, SNR Cut = 20
MSTO
age=15.0 Gyr, met= -1.9
isochrone, Spread RGB - TO: 0.18 +/- 0.07
[M/H] / dex
F606W/mag
stars

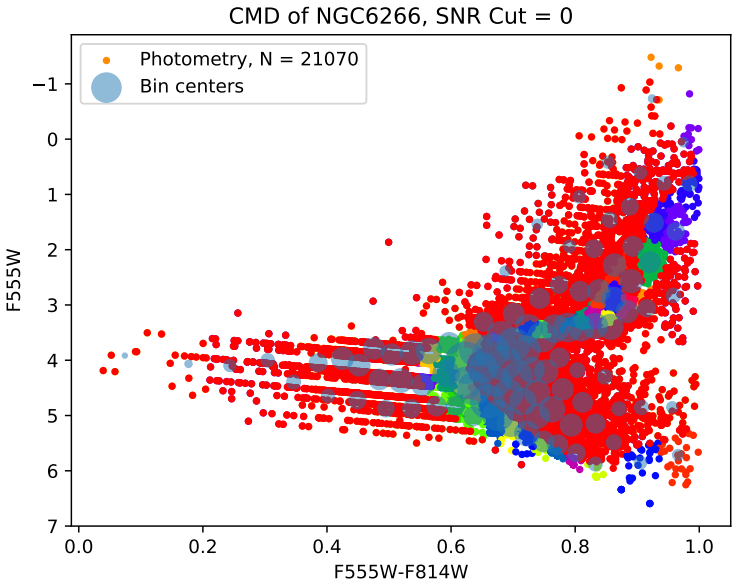
CMD of NGC6266, SNR Cut = 0
Photometry, N = 21070
Bin centers
F555W
F555W-F814W

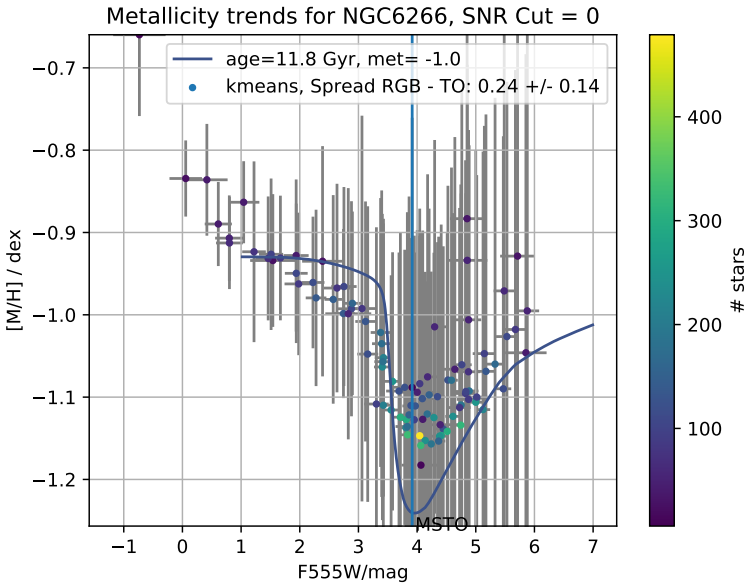
Metallicity trends for NGC6266, SNR Cut = 0
age=11.8 Gyr, met= -1.0
kmeans, Spread RGB - TO: 0.24 +/- 0.14
[M/H] / dex
F555W/mag
MSTO
stars

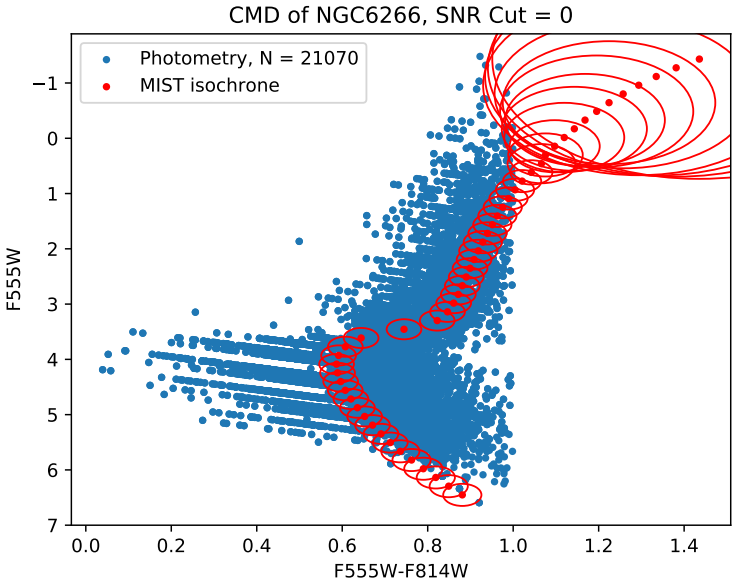
CMD of NGC6266, SNR Cut = 0
Photometry, N = 21070
MIST isochrone
F555W
F555W-F814W

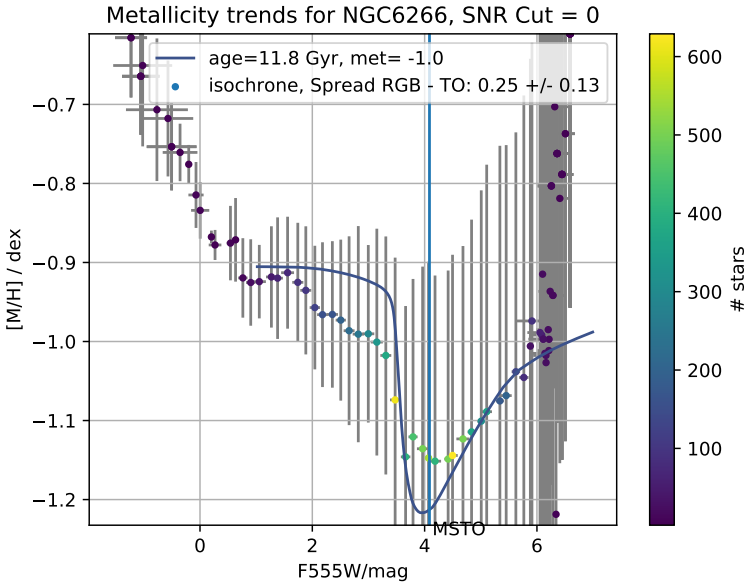
Metallicity trends for NGC6266, SNR Cut = 0
age=11.8 Gyr, met= -1.0
isochrone, Spread RGB - TO: 0.25 +/- 0.13
[M/H] / dex
F555W/mag
MSTO
stars

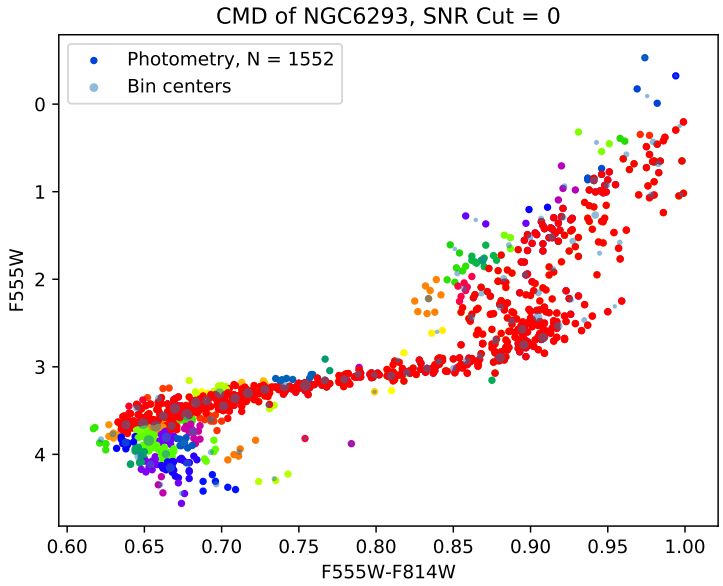
CMD of NGC6293, SNR Cut = 0
Photometry, N = 1552
Bin centers
F555W
F555W-F814W

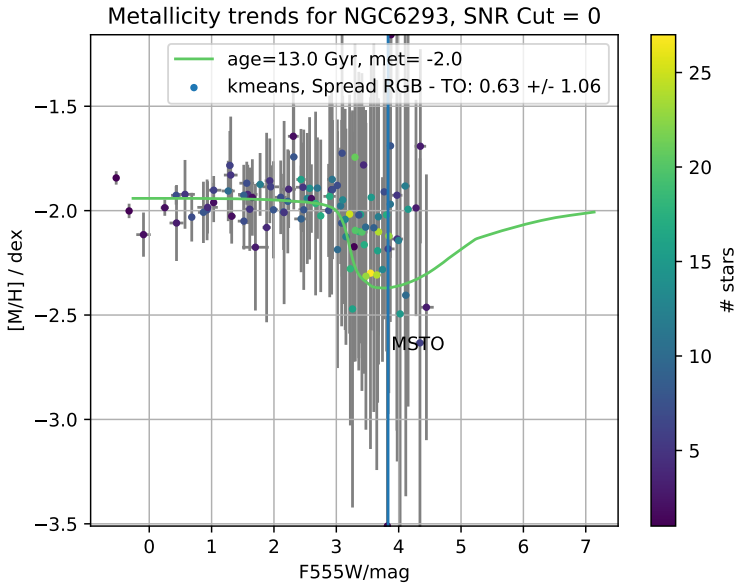
Metallicity trends for NGC6293, SNR Cut = 0
age=13.0 Gyr, met= -2.0
kmeans, Spread RGB - TO: 0.63 +/- 1.06
MSTO
[M/H] / dex
F555W/mag
stars

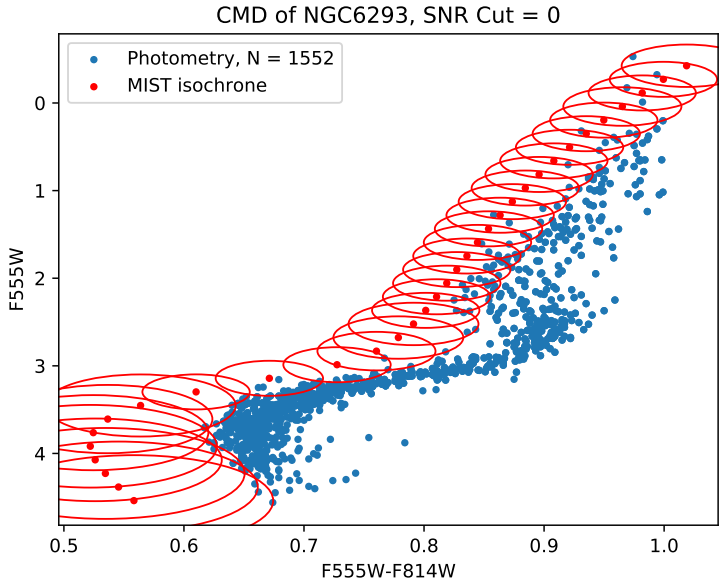
CMD of NGC6293, SNR Cut = 0
Photometry, N = 1552
MIST isochrone
F555W
F555W-F814W

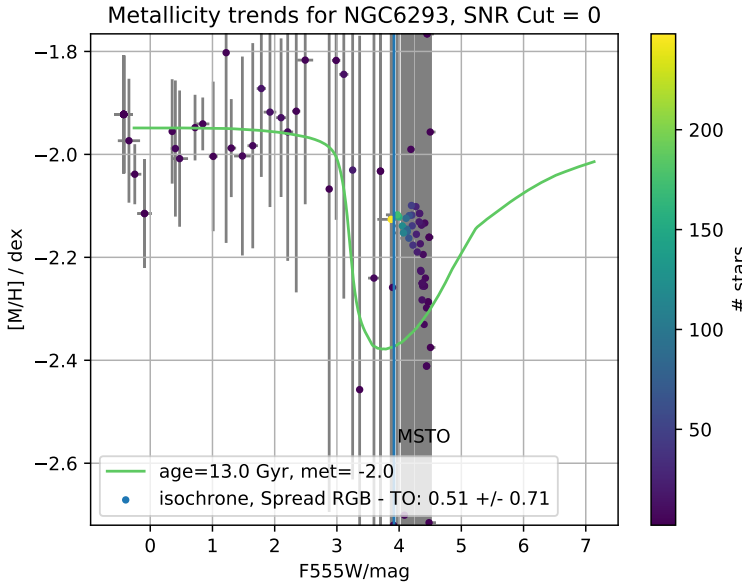
Metallicity trends for NGC6293, SNR Cut = 0
MSTO
age=13.0 Gyr, met= -2.0
isochrone, Spread RGB - TO: 0.51 +/- 0.71
[M/H] / dex
F555W/mag
stars

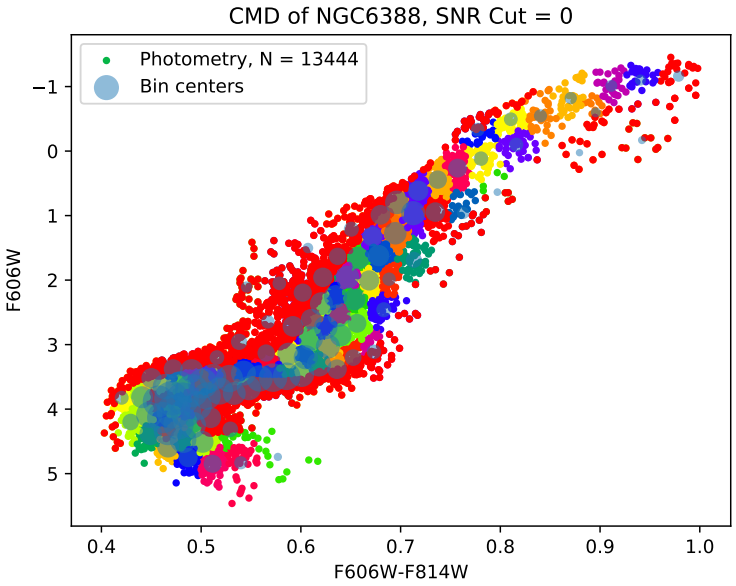
CMD of NGC6388, SNR Cut = 0
Photometry, N = 13444
Bin centers
F606W
F606W-F814W

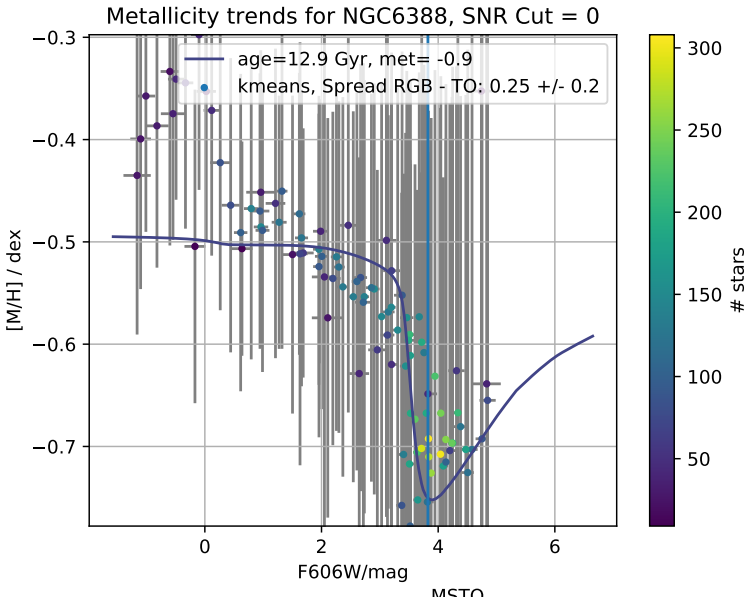
Metallicity trends for NGC6388, SNR Cut = 0
age=12.9 Gyr, met= -0.9
kmeans, Spread RGB - TO: 0.25 +/- 0.2
[M/H] / dex
F606W/mag
stars

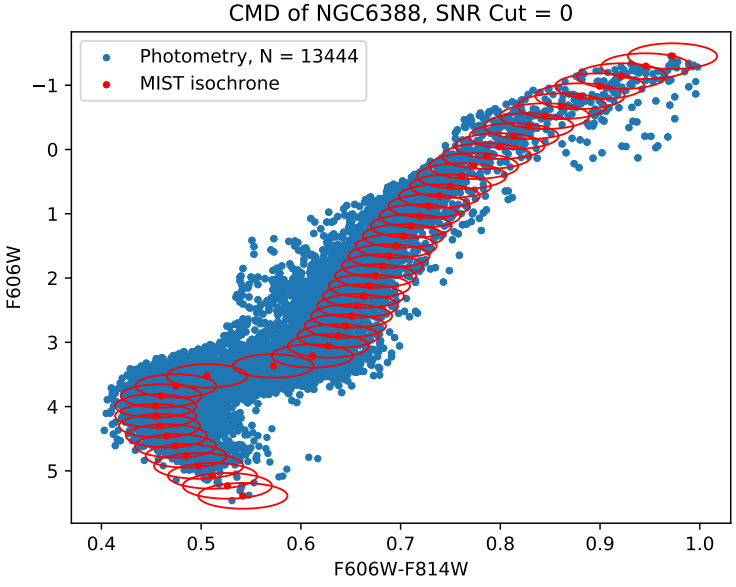
CMD of NGC6388, SNR Cut = 0
Photometry, N = 13444
MIST isochrone
F606W
F606W-F814W

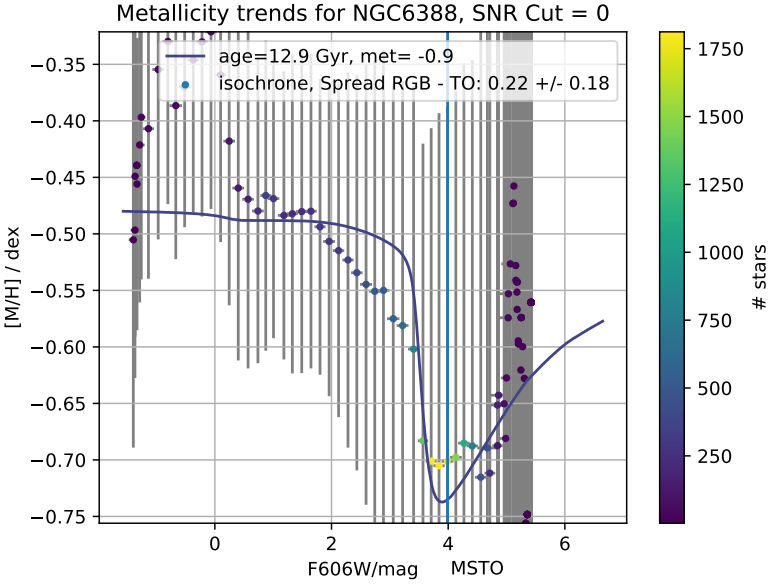
Metallicity trends for NGC6388, SNR Cut = 0
age=12.9 Gyr, met= -0.9
isochrone, Spread RGB - TO: 0.22 +/- 0.18
[M/H] / dex
F606W/mag
MSTO
stars

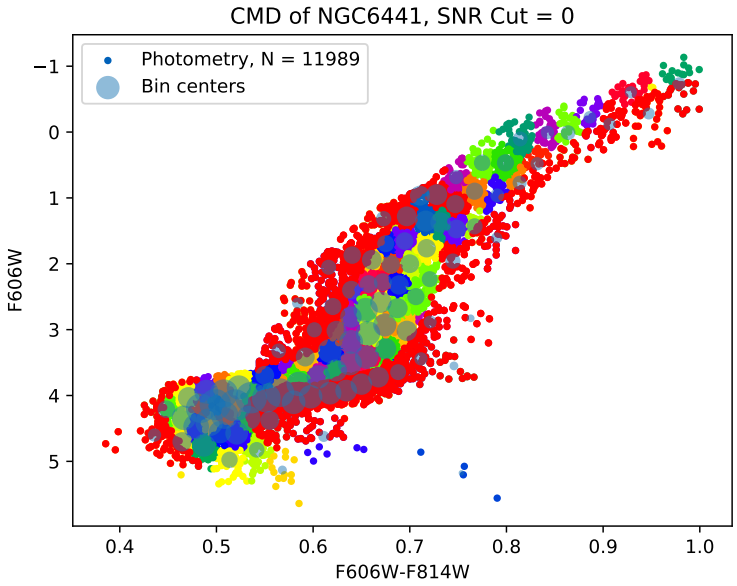
CMD of NGC6441, SNR Cut = 0
Photometry, N = 11989
Bin centers
F606W
F606W-F814W

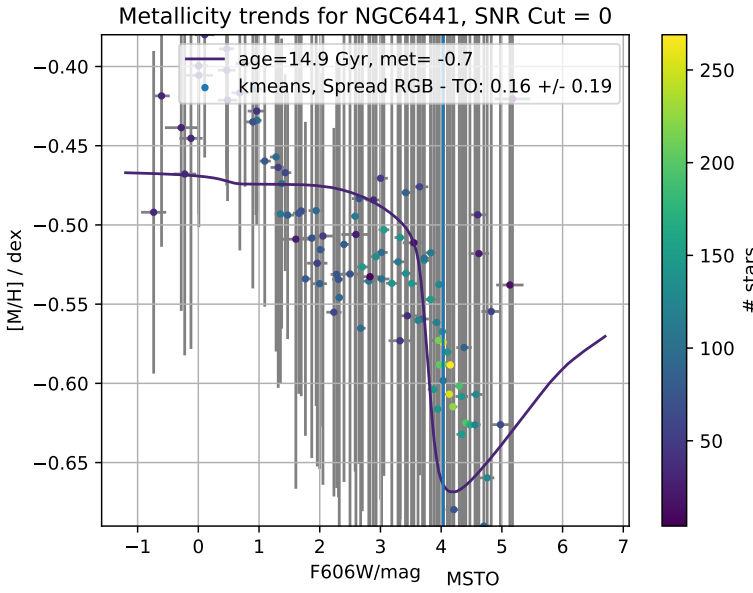
Metallicity trends for NGC6441, SNR Cut = 0
age=14.9 Gyr, met= -0.7
kmeans, Spread RGB - TO: 0.16 +/- 0.19
[M/H] / dex
F606W/mag
MSTO
stars

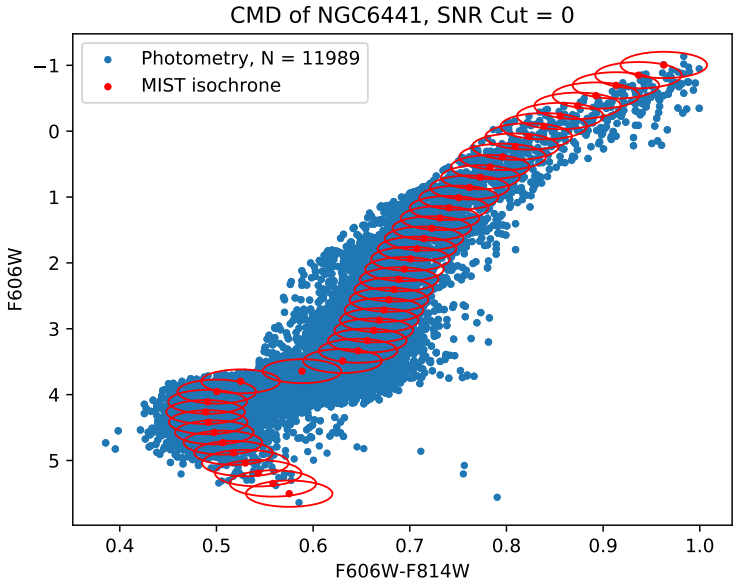
CMD of NGC6441, SNR Cut = 0
Photometry, N = 11989
MIST isochrone
F606W
F606W-F814W

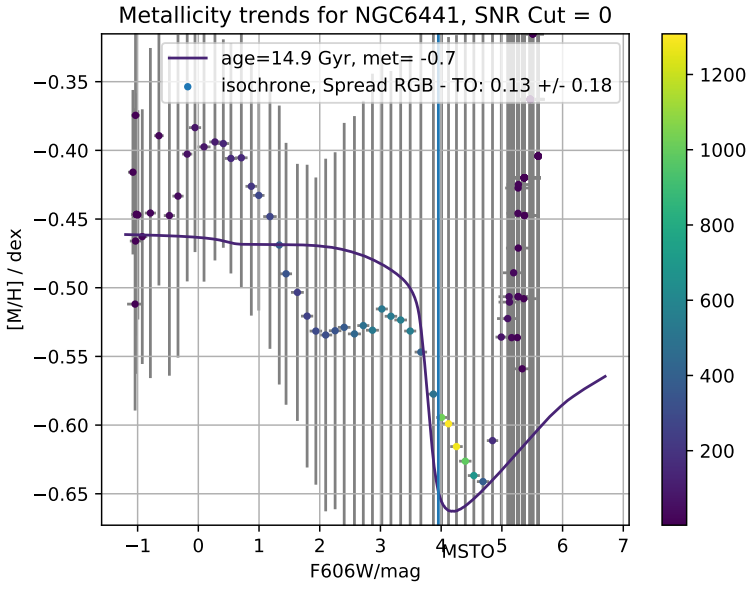
Metallicity trends for NGC6441, SNR Cut = 0
age=14.9 Gyr, met= -0.7
isochrone, Spread RGB - TO: 0.13 +/- 0.18
[M/H] / dex
F606W/mag
MSTO

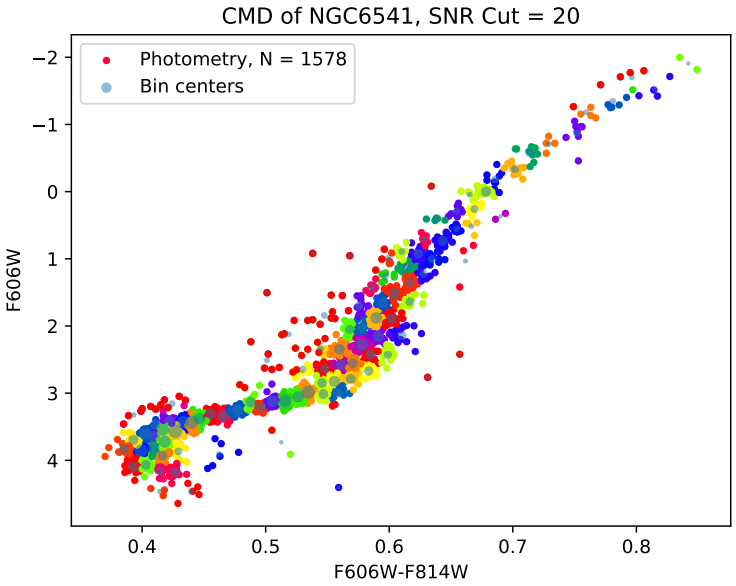
CMD of NGC6541, SNR Cut = 20
Photometry, N = 1578
Bin centers
F606W
F606W-F814W

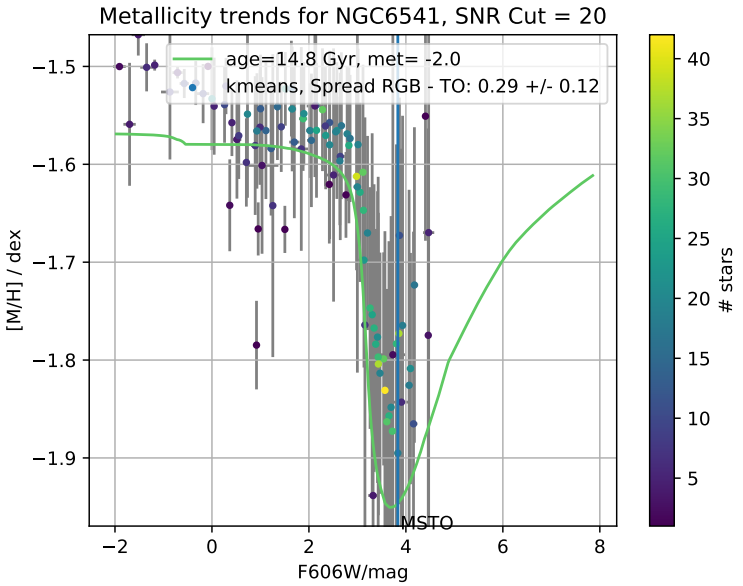
Metallicity trends for NGC6541, SNR Cut = 20
age=14.8 Gyr, met= -2.0
kmeans, Spread RGB - TO: 0.29 +/- 0.12
MSTO
[M/H] / dex
F606W/mag
stars

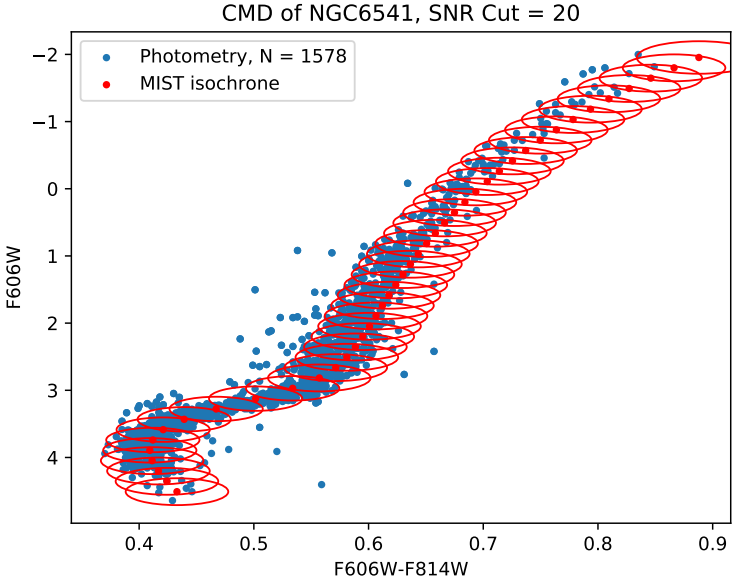
CMD of NGC6541, SNR Cut = 20
Photometry, N = 1578
MIST isochrone
F606W
F606W-F814W

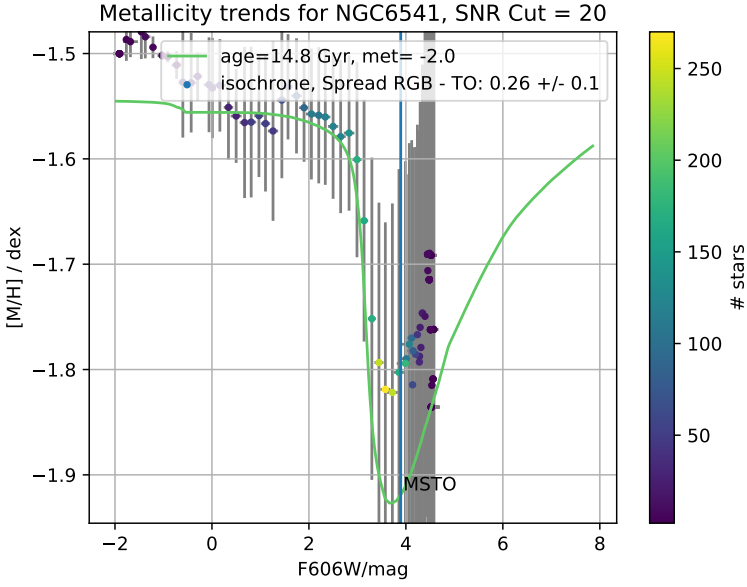
Metallicity trends for NGC6541, SNR Cut = 20
age=14.8 Gyr, met= -2.0
isochrone, Spread RGB - TO: 0.26 +/- 0.1
MSTO
[M/H] / dex
F606W/mag
stars

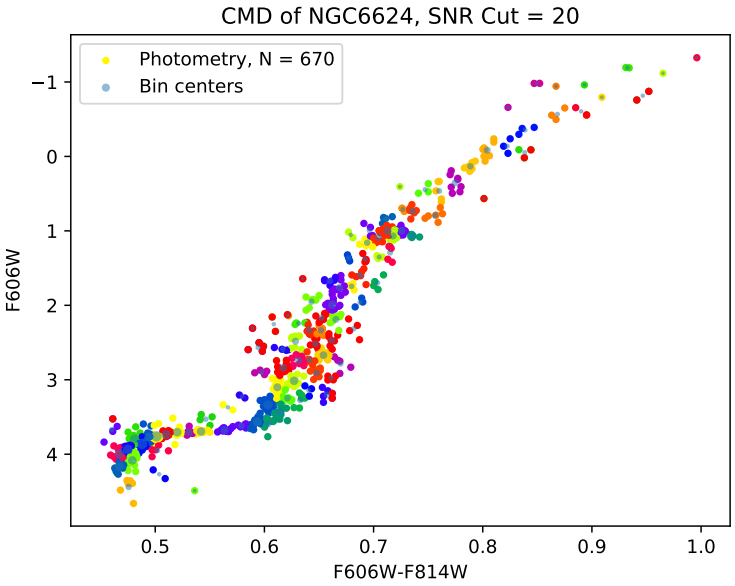
CMD of NGC6624, SNR Cut = 20
Photometry, N = 670
Bin centers
F606W
F606W-F814W

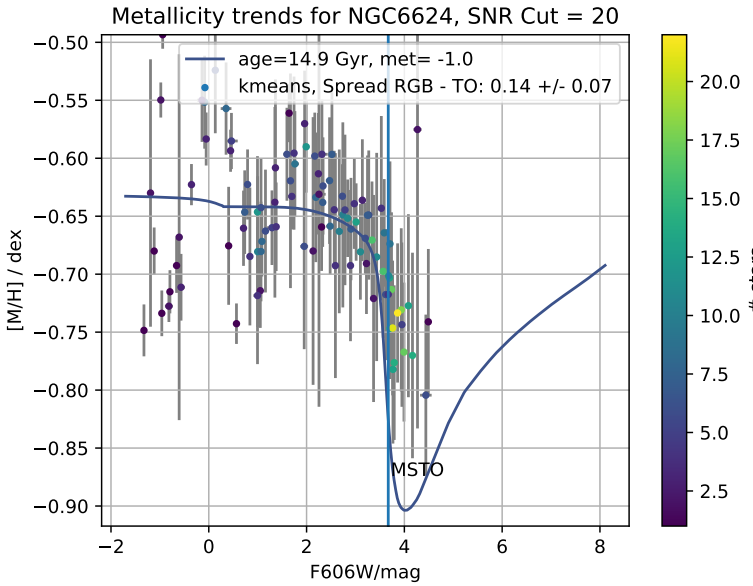
Metallicity trends for NGC6624, SNR Cut = 20
age=14.9 Gyr, met= -1.0
kmeans, Spread RGB - TO: 0.14 +/- 0.07
MSTO
[M/H] / dex
F606W/mag

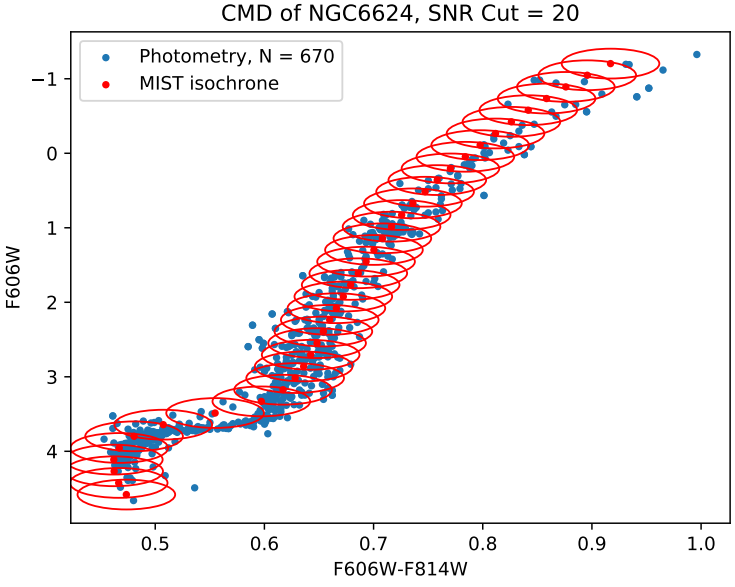
CMD of NGC6624, SNR Cut = 20
Photometry, N = 670
MIST isochrone
F606W
F606W-F814W

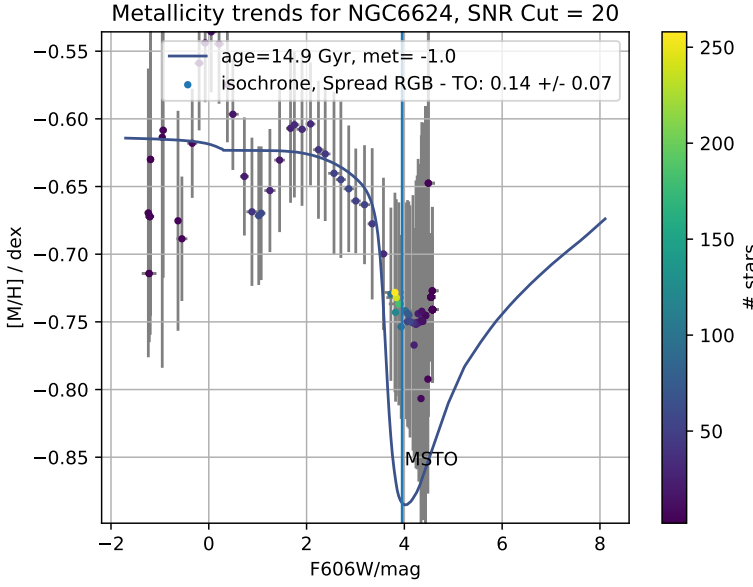
Metallicity trends for NGC6624, SNR Cut = 20
age=14.9 Gyr, met= -1.0
isochrone, Spread RGB - TO: 0.14 +/- 0.07
MSTO
[M/H] / dex
F606W/mag

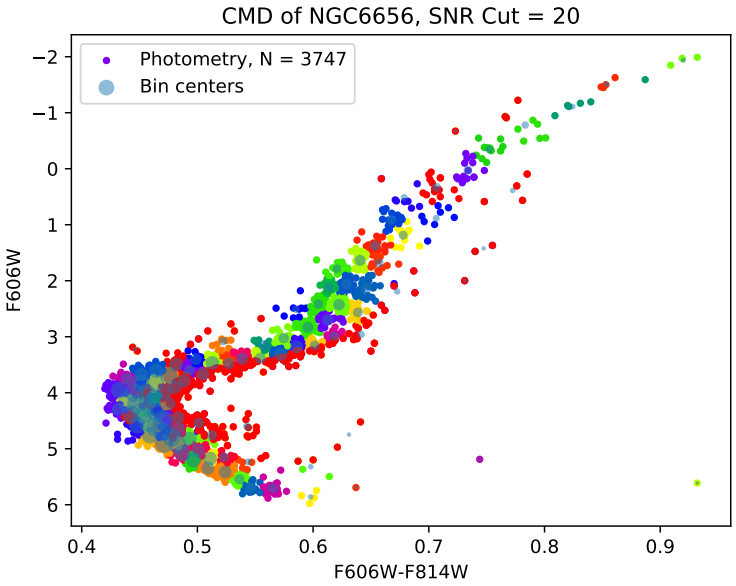
CMD of NGC6656, SNR Cut = 20
Photometry, N = 3747
Bin centers
F606W
F606W-F814W

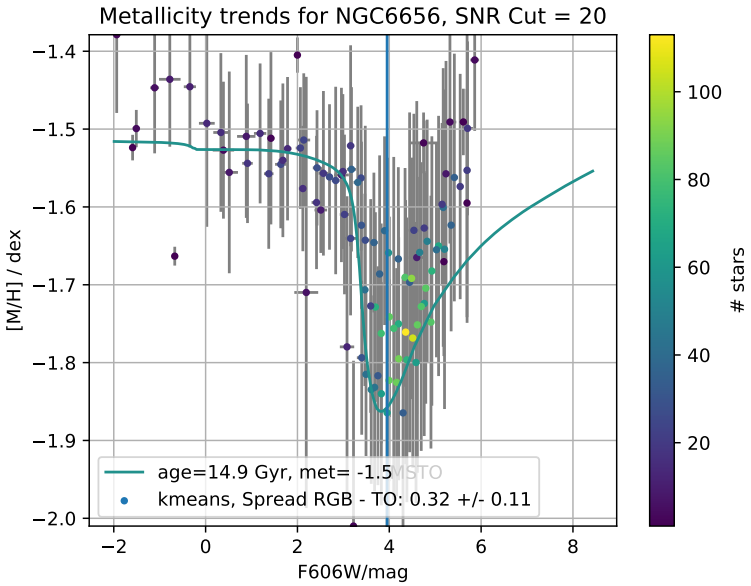
Metallicity trends for NGC6656, SNR Cut = 20
age=14.9 Gyr, met= -1.5
kmeans, Spread RGB - TO: 0.32 +/- 0.11
MSTO
[M/H] / dex
F606W/mag
stars

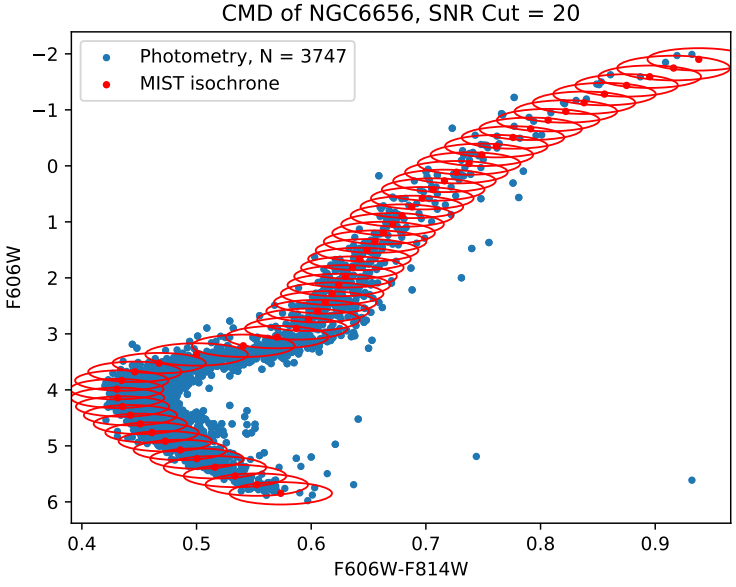
CMD of NGC6656, SNR Cut = 20
Photometry, N = 3747
MIST isochrone
F606W
F606W-F814W

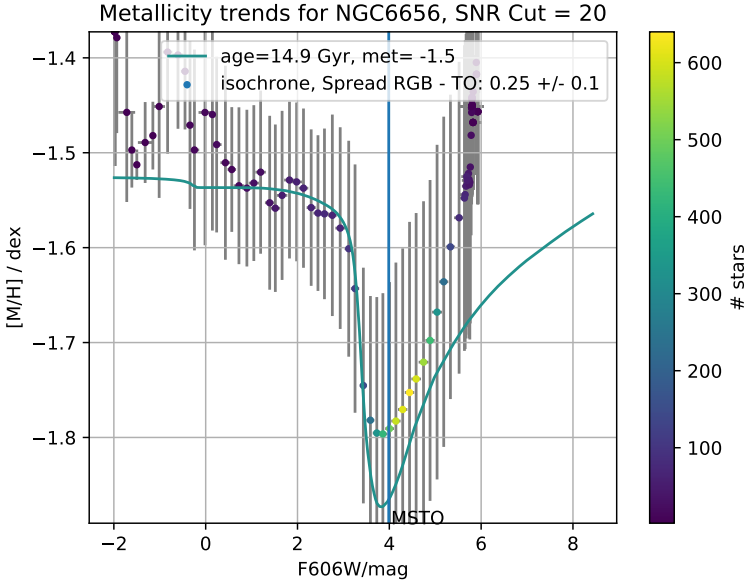
Metallicity trends for NGC6656, SNR Cut = 20
age=14.9 Gyr, met= -1.5
isochrone, Spread RGB - TO: 0.25 +/- 0.1
MSTO
[M/H] / dex
F606W/mag
stars

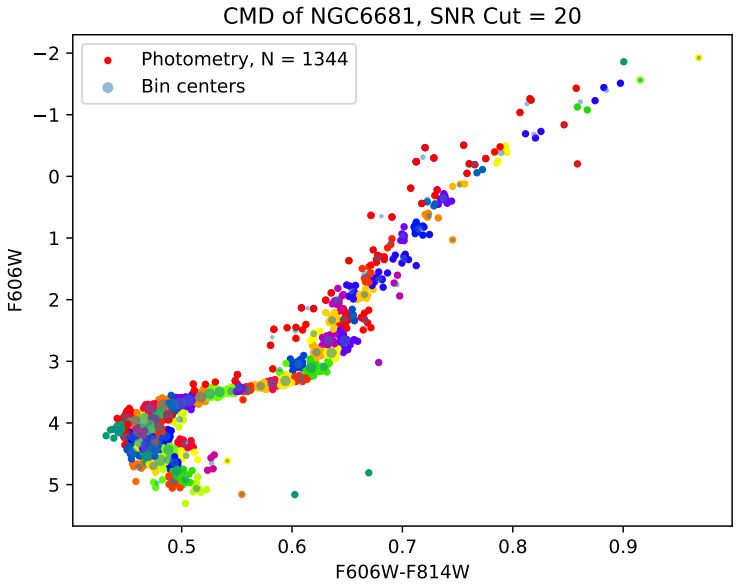
CMD of NGC6681, SNR Cut = 20
Photometry, N = 1344
Bin centers
F606W
F606W-F814W

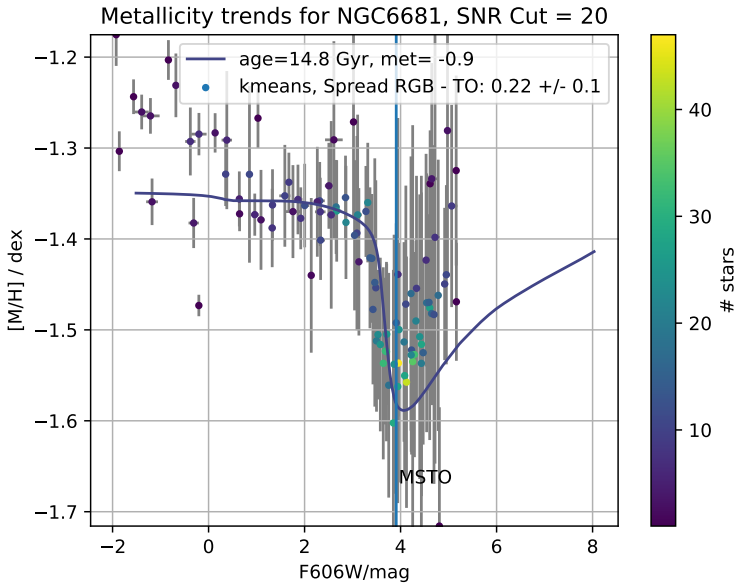
Metallicity trends for NGC6681, SNR Cut = 20
age=14.8 Gyr, met= -0.9
kmeans, Spread RGB - TO: 0.22 +/- 0.1
[M/H] / dex
F606W/mag
MSTO
stars

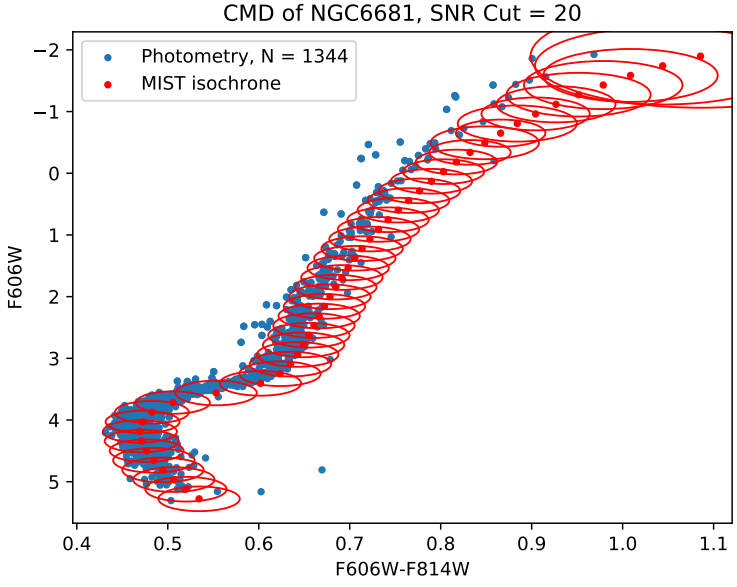
CMD of NGC6681, SNR Cut = 20
Photometry, N = 1344
MIST isochrone
F606W
F606W-F814W

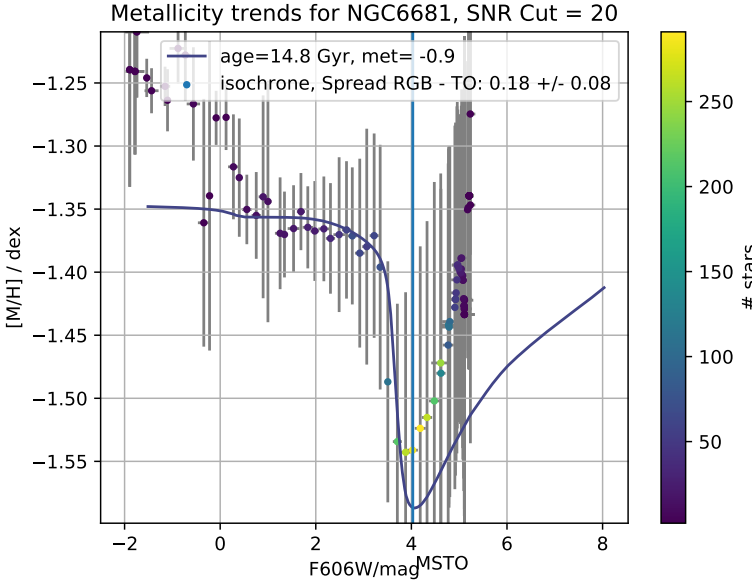
Metallicity trends for NGC6681, SNR Cut = 20
age=14.8 Gyr, met= -0.9
isochrone, Spread RGB - TO: 0.18 +/- 0.08
[M/H] / dex
F606W/mag
MSTO
stars

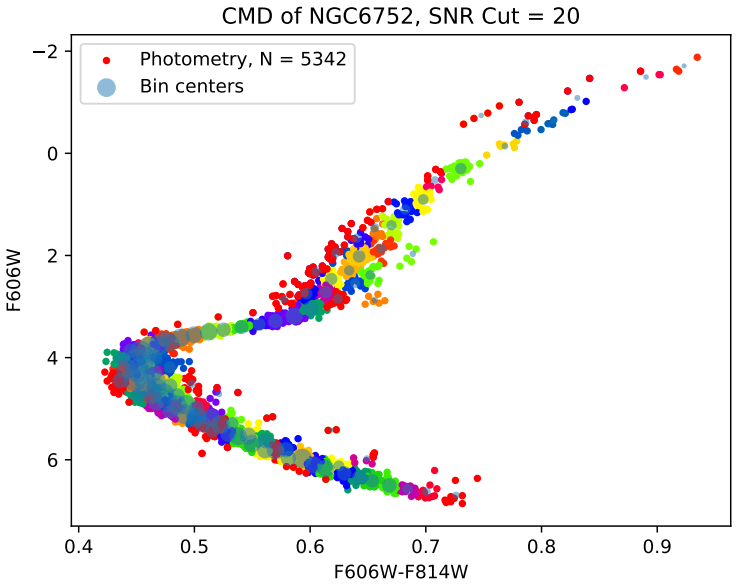
CMD of NGC6752, SNR Cut = 20
Photometry, N = 5342
Bin centers
F606W
F606W-F814W

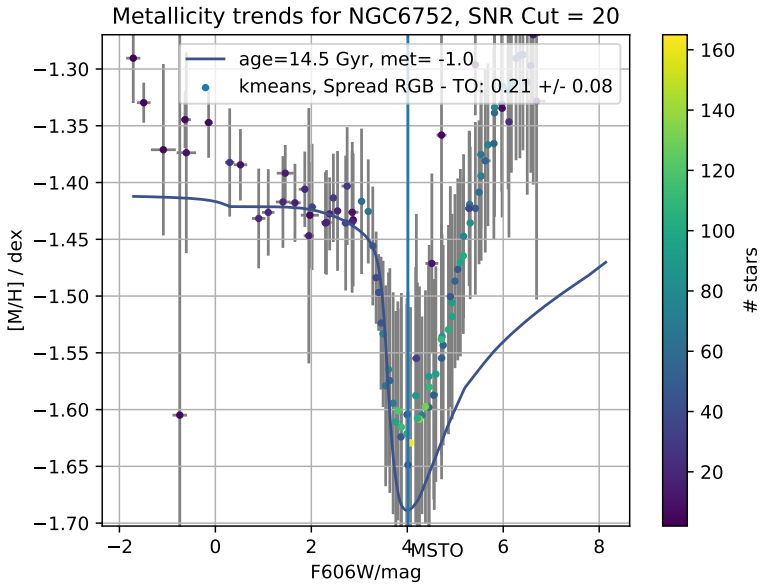
Metallicity trends for NGC6752, SNR Cut = 20
age=14.5 Gyr, met= -1.0
kmeans, Spread RGB - TO: 0.21 +/- 0.08
[M/H] / dex
MSTO
F606W/mag
stars

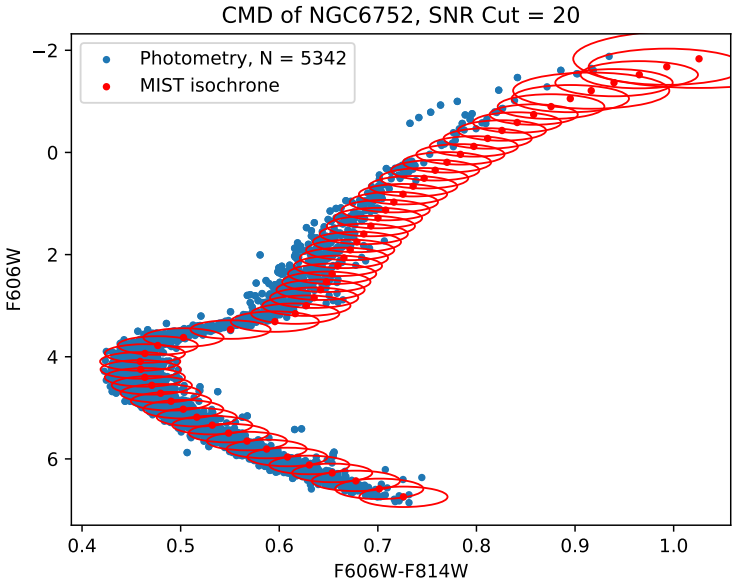
CMD of NGC6752, SNR Cut = 20
Photometry, N = 5342
MIST isochrone
F606W
F606W-F814W

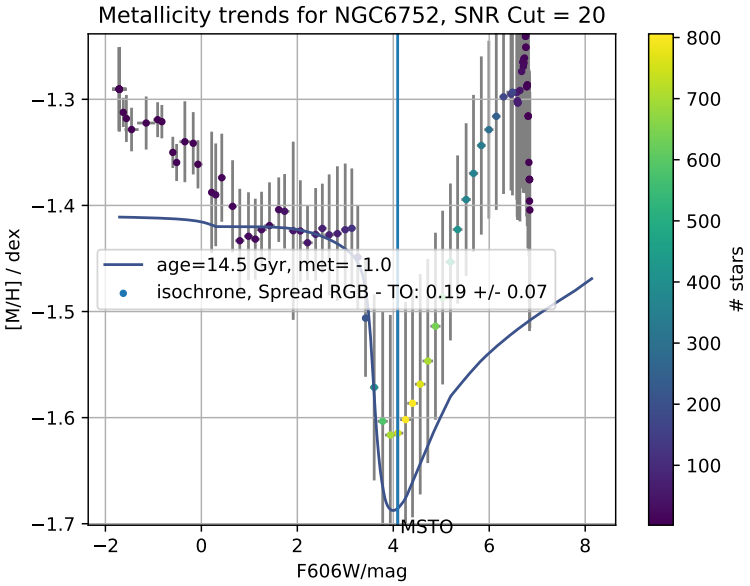
Metallicity trends for NGC6752, SNR Cut = 20
age=14.5 Gyr, met= -1.0
isochrone, Spread RGB - TO: 0.19 +/- 0.07
[M/H] / dex
MSTO
F606W/mag
stars

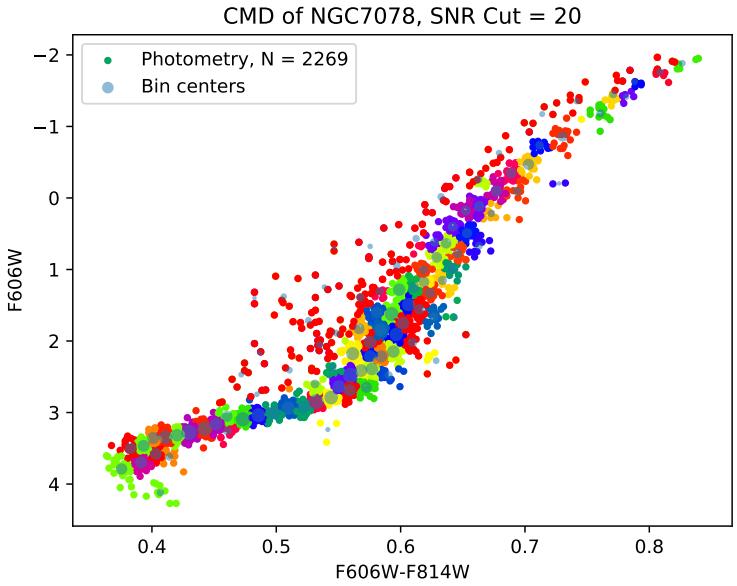
CMD of NGC7078, SNR Cut = 20
Photometry, N = 2269
Bin centers
F606W
F606W-F814W

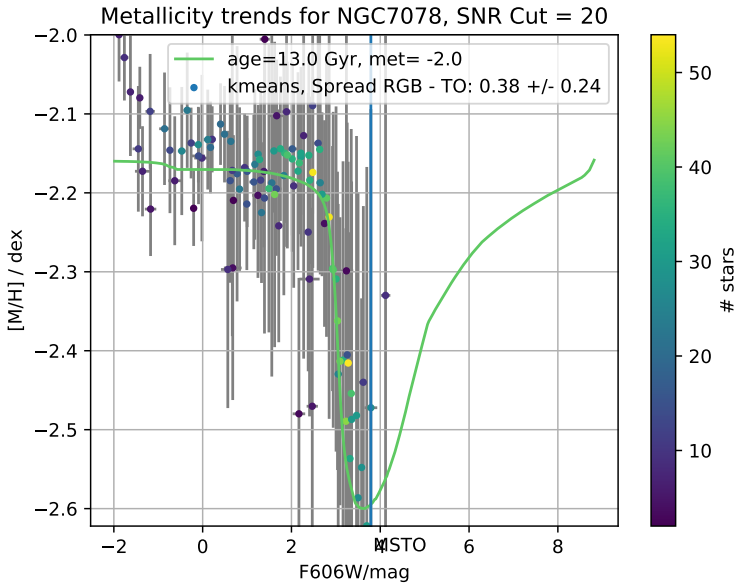
Metallicity trends for NGC7078, SNR Cut = 20
age=13.0 Gyr, met= -2.0
kmeans, Spread RGB - TO: 0.38 +/- 0.24
[M/H] / dex
F606W/mag
MSTO
stars

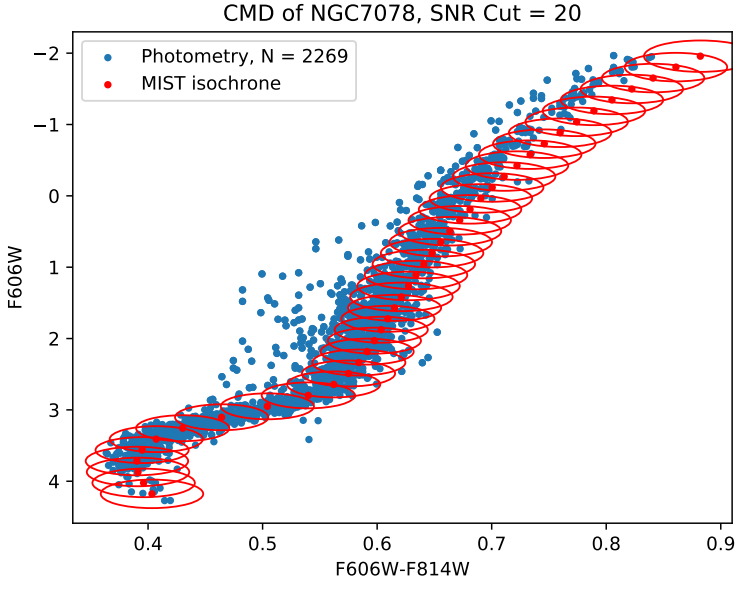
CMD of NGC7078, SNR Cut = 20
Photometry, N = 2269
MIST isochrone
F606W
F606W-F814W

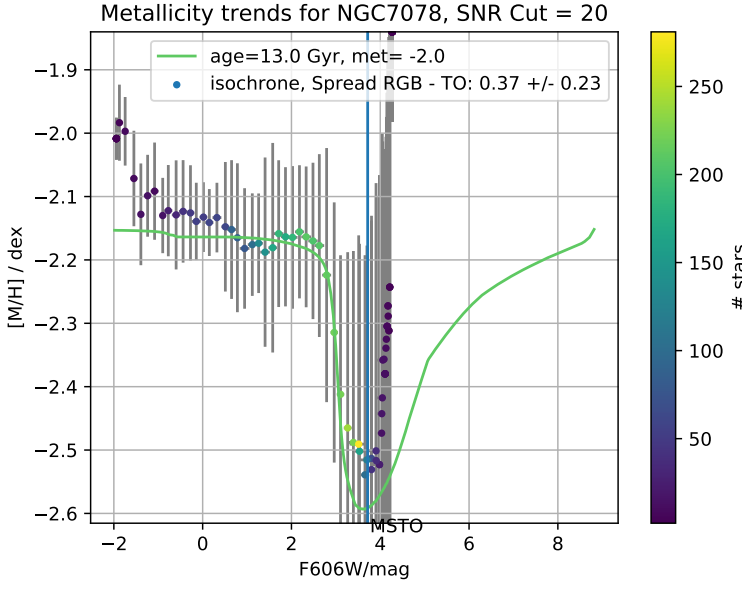
Metallicity trends for NGC7078, SNR Cut = 20
age=13.0 Gyr, met= -2.0
isochrone, Spread RGB - TO: 0.37 +/- 0.23
[M/H] / dex
F606W/mag
MSTO
stars

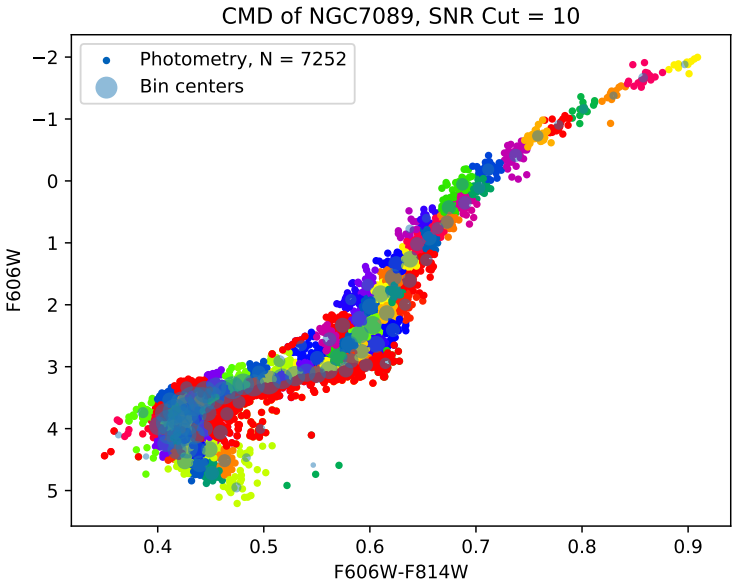
CMD of NGC7089, SNR Cut = 10
Photometry, N = 7252
Bin centers
F606W
F606W-F814W

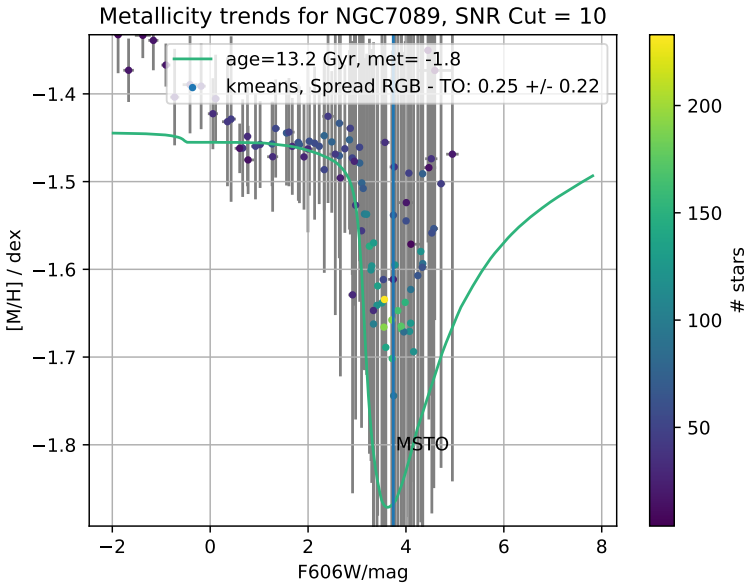
Metallicity trends for NGC7089, SNR Cut = 10
age=13.2 Gyr, met= -1.8
kmeans, Spread RGB - TO: 0.25 +/- 0.22
MSTO
[M/H] / dex
F606W/mag
stars

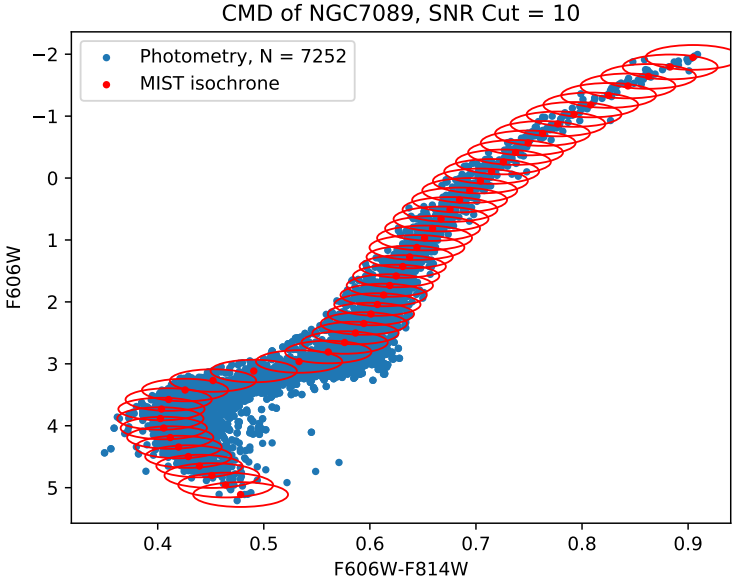
CMD of NGC7089, SNR Cut = 10
Photometry, N = 7252
MIST isochrone
F606W
F606W-F814W

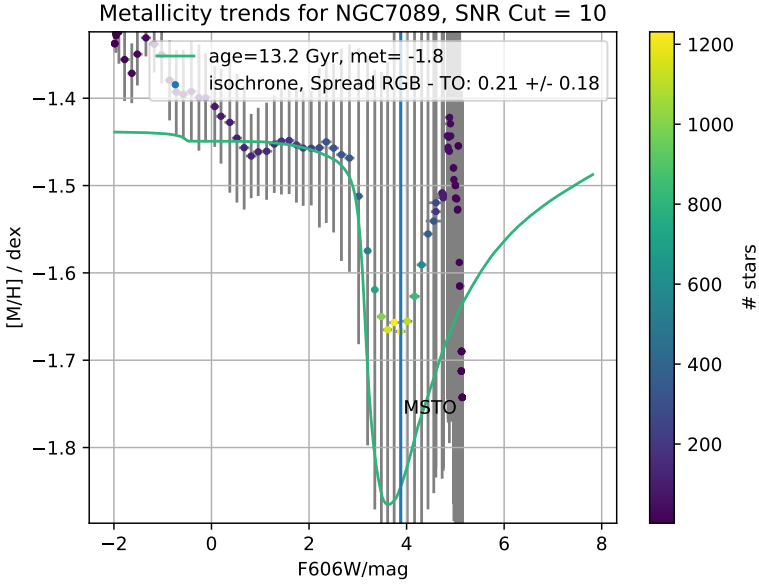
Metallicity trends for NGC7089, SNR Cut = 10
age=13.2 Gyr, met= -1.8
isochrone, Spread RGB - TO: 0.21 +/- 0.18
MSTO
[M/H] / dex
F606W/mag
stars

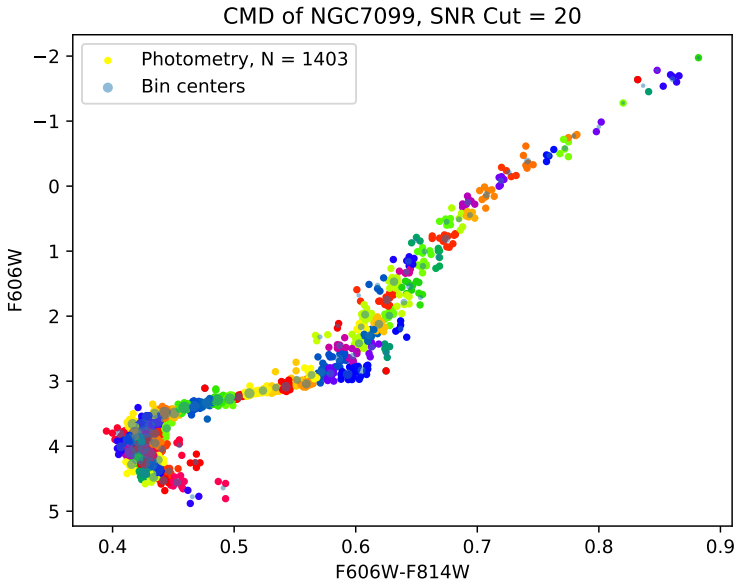
CMD of NGC7099, SNR Cut = 20
Photometry, N = 1403
Bin centers
F606W
F606W-F814W

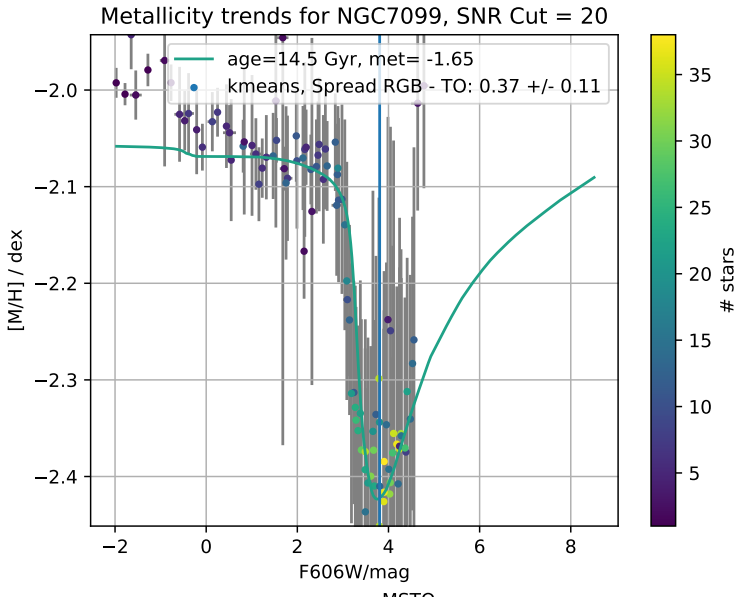
Metallicity trends for NGC7099, SNR Cut = 20
age=14.5 Gyr, met= -1.65
kmeans, Spread RGB - TO: 0.37 +/- 0.11
[M/H] / dex
F606W/mag
stars

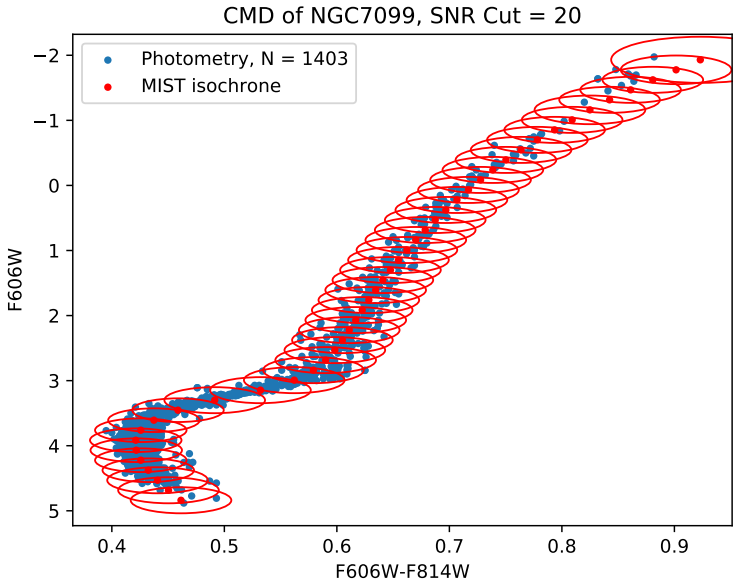
CMD of NGC7099, SNR Cut = 20
Photometry, N = 1403
MIST isochrone
F606W
F606W-F814W

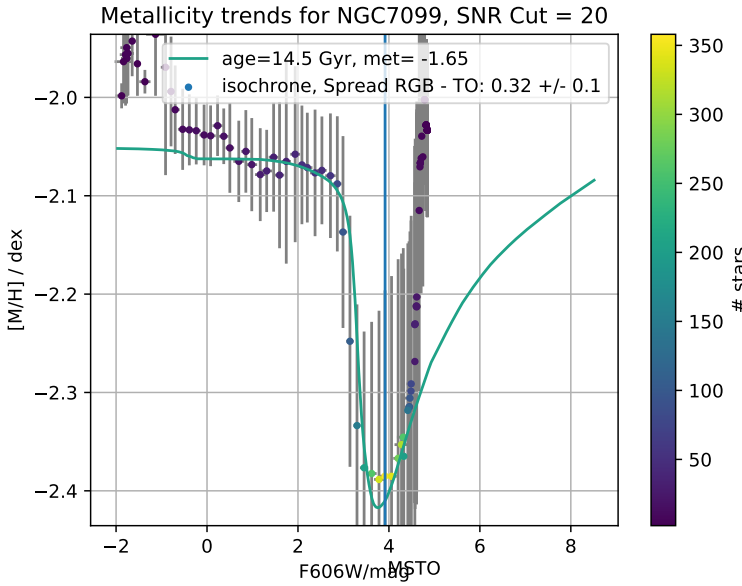
Metallicity trends for NGC7099, SNR Cut = 20
age=14.5 Gyr, met= -1.65
isochrone, Spread RGB - TO: 0.32 +/- 0.1
[M/H] / dex
F606W/mag
MSTO
stars

B. Metallicity Spread Tables

Table B.1.: Results from the spread quantification as described in Section 4.2.4 for an SNR cut of 20 and the method kmeans. The metallicity is taken from Harris (2010). The column "MS vis?" denotes if a main sequence is visible, "RGB inc?" denotes if a significantly increasing metallicity is observed on the RGB and "MSTO sep?" denotes if the main sequence turnoff is clearly separated from the SGB in the data. Details can be found in Section 5.2.

Cluster	Metallicity	RGB	MSTO	MS vis?	RGB inc?	MSTO sep?
NGC 104	-0.72	-0.73 ± 0.03	-0.85 ± 0.03	yes	no	yes
NGC 1851	-1.18	-1.09 ± 0.04	-	no	yes	no
NGC 1904	-1.60	-1.49 ± 0.05	-1.5 ± 0.02	no	no	no
NGC 2808	-1.14	-1.05 ± 0.06	-1.19 ± 0.09	no	yes	yes
NGC 3201	-1.59	-1.31 ± 0.07	-1.51 ± 0.03	yes	no	yes
NGC 362	-1.26	-1.12 ± 0.05	-1.36 ± 0.12	no	yes	yes
NGC 5139	-1.53	-1.41 ± 0.15	-1.85 ± 0.13	no	no	yes
NGC 5286	-1.69	-1.51 ± 0.07	-1.69 ± 0.18	no	no	no
NGC 5904	-1.29	-1.19 ± 0.03	-1.42 ± 0.05	yes	yes	yes
NGC 6093	-1.75	-1.51 ± 0.05	-1.78 ± 0.11	no	no	yes
NGC 6121	-1.16	-0.94 ± 0.04	-1.19 ± 0.05	no	yes	yes
NGC 6218	-1.37	-1.18 ± 0.04	-1.37 ± 0.04	yes	yes	yes
NGC 6254	-1.56	-1.42 ± 0.04	-1.61 ± 0.07	yes	yes	yes
NGC 6266	-1.18	-0.94 ± 0.06	-1.14 ± 0.07	no	yes	yes
NGC 6388	-0.55	-0.48 ± 0.08	-	no	no	no
NGC 6441	-0.46	-0.46 ± 0.07	-	no	no	no
NGC 6541	-1.81	-1.58 ± 0.05	-1.87 ± 0.1	no	yes	yes
NGC 6624	-0.44	-0.64 ± 0.05	-0.77 ± 0.04	no	no	yes
NGC 6656	-1.70	-1.53 ± 0.07	-1.85 ± 0.09	yes	no	yes
NGC 6681	-1.62	-1.35 ± 0.05	-1.57 ± 0.09	yes	no	yes
NGC 6752	-1.54	-1.42 ± 0.03	-1.63 ± 0.07	yes	yes	yes
NGC 7078	-2.37	-2.17 ± 0.07	-2.55 ± 0.23	no	no	yes
NGC 7089	-1.65	-1.46 ± 0.03	-1.65 ± 0.16	no	yes	no
NGC 7099	-2.27	-2.07 ± 0.05	-2.43 ± 0.1	no	no	yes

Table B.2.: Same as Table B.1, but for the isochrone method.

Cluster	Metallicity	RGB	MSTO	MS vis?	RGB inc?	MSTO sep?
NGC 104	-0.72	-0.72 ± 0.04	-0.83 ± 0.03	yes	no	yes
NGC 1851	-1.18	-1.08 ± 0.04	-1.24 ± 0.09	no	yes	yes
NGC 1904	-1.60	-1.46 ± 0.07	-1.5 ± 0.0	no	no	no
NGC 2808	-1.14	-1.04 ± 0.05	-1.23 ± 0.06	no	yes	yes
NGC 3201	-1.59	-1.3 ± 0.05	-1.5 ± 0.02	yes	yes	yes
NGC 362	-1.26	-1.11 ± 0.04	-1.31 ± 0.1	yes	yes	yes
NGC 5139	-1.53	-1.43 ± 0.09	-1.79 ± 0.11	yes	no	yes
NGC 5286	-1.69	-1.5 ± 0.04	-1.79 ± 0.2	no	yes	yes
NGC 5904	-1.29	-1.18 ± 0.04	-1.39 ± 0.06	yes	yes	yes
NGC 6093	-1.75	-1.52 ± 0.03	-1.8 ± 0.06	no	yes	yes
NGC 6121	-1.16	-0.93 ± 0.03	-1.13 ± 0.04	no	yes	yes
NGC 6218	-1.37	-1.16 ± 0.05	-1.36 ± 0.04	yes	yes	yes
NGC 6254	-1.56	-1.41 ± 0.04	-1.6 ± 0.05	yes	yes	yes
NGC 6266	-1.18	-0.91 ± 0.06	-1.12 ± 0.06	no	yes	yes
NGC 6388	-0.55	-0.64 ± 0.11	-	no	yes	no
NGC 6441	-0.46	-0.52 ± 0.06	-	no	yes	no
NGC 6541	-1.81	-1.56 ± 0.03	-1.81 ± 0.1	no	yes	yes
NGC 6624	-0.44	-0.62 ± 0.05	-0.76 ± 0.05	yes	no	yes
NGC 6656	-1.70	-1.54 ± 0.05	-1.79 ± 0.08	yes	yes	yes
NGC 6681	-1.62	-1.35 ± 0.04	-1.54 ± 0.07	yes	yes	yes
NGC 6752	-1.54	-1.42 ± 0.03	-1.61 ± 0.06	yes	yes	yes
NGC 7078	-2.37	-2.16 ± 0.07	-2.53 ± 0.22	no	no	yes
NGC 7089	-1.65	-1.45 ± 0.03	-1.74 ± 0.08	no	yes	yes
NGC 7099	-2.27	-2.06 ± 0.04	-2.39 ± 0.09	yes	yes	yes

Table B.3.: Same as Table B.1, but for the fixed length method.

Cluster	Metallicity	RGB	MSTO	MS vis?	RGB inc?	MSTO sep?
NGC 104	-0.72	-0.73 ± 0.03	-0.83 ± 0.03	yes	no	yes
NGC 1851	-1.18	-1.08 ± 0.04	-1.19 ± 0.13	no	yes	no
NGC 1904	-1.60	-1.46 ± 0.06	-1.5 ± 0.02	no	yes	no
NGC 2808	-1.14	-1.04 ± 0.05	-1.21 ± 0.06	no	yes	yes
NGC 3201	-1.59	-1.3 ± 0.05	-1.5 ± 0.03	yes	yes	yes
NGC 362	-1.26	-1.11 ± 0.04	-1.35 ± 0.11	no	yes	yes
NGC 5139	-1.53	-1.42 ± 0.09	-1.65 ± 0.15	no	no	no
NGC 5286	-1.69	-1.5 ± 0.05	-1.73 ± 0.18	no	yes	yes
NGC 5904	-1.29	-1.19 ± 0.04	-1.4 ± 0.06	yes	yes	yes
NGC 6093	-1.75	-1.52 ± 0.03	-1.77 ± 0.09	no	no	yes
NGC 6121	-1.16	-0.94 ± 0.04	-1.14 ± 0.04	no	yes	yes
NGC 6218	-1.37	-1.16 ± 0.05	-1.36 ± 0.04	yes	yes	yes
NGC 6254	-1.56	-1.42 ± 0.04	-1.6 ± 0.05	yes	yes	yes
NGC 6266	-1.18	-0.91 ± 0.06	-1.11 ± 0.05	no	yes	yes
NGC 6388	-0.55	-0.52 ± 0.09	-	no	yes	no
NGC 6441	-0.46	-0.48 ± 0.07	-	no	no	no
NGC 6541	-1.81	-1.55 ± 0.03	-1.84 ± 0.12	no	no	yes
NGC 6624	-0.44	-0.62 ± 0.05	-0.76 ± 0.05	no	no	yes
NGC 6656	-1.70	-1.54 ± 0.06	-1.77 ± 0.08	yes	no	yes
NGC 6681	-1.62	-1.36 ± 0.04	-1.54 ± 0.08	no	yes	yes
NGC 6752	-1.54	-1.41 ± 0.03	-1.62 ± 0.06	yes	no	yes
NGC 7078	-2.37	-2.17 ± 0.06	-2.57 ± 0.29	no	no	yes
NGC 7089	-1.65	-1.45 ± 0.03	-1.69 ± 0.15	no	yes	yes
NGC 7099	-2.27	-2.06 ± 0.03	-2.39 ± 0.09	no	no	yes

Table B.4.: Same as Table B.1, but for the fixed size method.

Cluster	Metallicity	RGB	MSTO	MS vis?	RGB inc?	MSTO sep?
NGC 104	-0.72	-0.73 ± 0.03	-0.84 ± 0.03	no	no	yes
NGC 1851	-1.18	-1.08 ± 0.04	-	no	yes	no
NGC 1904	-1.60	-	-	no	no	no
NGC 2808	-1.14	-1.04 ± 0.05	-	no	yes	no
NGC 3201	-1.59	-	-1.5 ± 0.02	no	no	no
NGC 362	-1.26	-1.12 ± 0.05	-	no	yes	no
NGC 5139	-1.53	-1.43 ± 0.1	-1.63 ± 0.15	no	no	no
NGC 5286	-1.69	-1.5 ± 0.06	-	no	yes	no
NGC 5904	-1.29	-1.2 ± 0.04	-1.4 ± 0.05	no	yes	yes
NGC 6093	-1.75	-1.53 ± 0.04	-	no	no	no
NGC 6121	-1.16	-	-	no	no	no
NGC 6218	-1.37	-	-1.36 ± 0.04	no	no	no
NGC 6254	-1.56	-1.44 ± 0.04	-1.61 ± 0.06	yes	yes	yes
NGC 6266	-1.18	-0.94 ± 0.06	-1.11 ± 0.06	no	no	yes
NGC 6388	-0.55	-0.48 ± 0.07	-	no	yes	no
NGC 6441	-0.46	-0.46 ± 0.07	-	no	no	no
NGC 6541	-1.81	-1.57 ± 0.04	-1.81 ± 0.11	no	yes	yes
NGC 6624	-0.44	-0.64 ± 0.05	-	no	no	no
NGC 6656	-1.70	-1.54 ± 0.08	-1.78 ± 0.1	yes	no	yes
NGC 6681	-1.62	-1.36 ± 0.06	-1.53 ± 0.08	no	no	yes
NGC 6752	-1.54	-1.42 ± 0.04	-1.63 ± 0.07	yes	no	yes
NGC 7078	-2.37	-2.17 ± 0.06	-	no	no	no
NGC 7089	-1.65	-1.46 ± 0.03	-	no	yes	no
NGC 7099	-2.27	-2.07 ± 0.07	-2.4 ± 0.09	no	no	yes

Table B.5.: Same as Table B.1, but without SNR cut.

Cluster	Metallicity	RGB	MSTO	MS vis?	RGB inc?	MSTO sep?
NGC 104	-0.72	-0.73 ± 0.04	-0.84 ± 0.09	yes	no	no
NGC 1851	-1.18	-1.08 ± 0.05	-1.3 ± 0.18	yes	yes	no
NGC 1904	-1.60	-1.46 ± 0.06	-1.62 ± 0.19	yes	no	no
NGC 2808	-1.14	-1.05 ± 0.06	-1.27 ± 0.21	yes	yes	no
NGC 3201	-1.59	-1.31 ± 0.06	-1.5 ± 0.02	yes	yes	yes
NGC 362	-1.26	-1.11 ± 0.06	-1.36 ± 0.17	yes	yes	yes
NGC 5139	-1.53	-1.41 ± 0.11	-1.77 ± 0.18	yes	no	yes
NGC 5286	-1.69	-1.51 ± 0.07	-1.84 ± 0.27	yes	no	no
NGC 5904	-1.29	-1.19 ± 0.05	-1.42 ± 0.11	yes	yes	yes
NGC 6093	-1.75	-1.53 ± 0.06	-1.83 ± 0.27	yes	no	no
NGC 6121	-1.16	-0.93 ± 0.05	-1.16 ± 0.06	yes	yes	yes
NGC 6218	-1.37	-1.18 ± 0.05	-1.36 ± 0.04	yes	yes	yes
NGC 6254	-1.56	-1.42 ± 0.04	-1.61 ± 0.07	yes	yes	yes
NGC 6266	-1.18	-0.92 ± 0.07	-1.16 ± 0.12	yes	yes	yes
NGC 6293	-1.99	-1.94 ± 0.13	-2.57 ± 1.06	no	no	no
NGC 6388	-0.55	-0.5 ± 0.08	-0.75 ± 0.18	no	yes	no
NGC 6441	-0.46	-0.47 ± 0.07	-0.63 ± 0.18	yes	no	no
NGC 6541	-1.81	-1.56 ± 0.04	-1.85 ± 0.17	yes	yes	yes
NGC 6624	-0.44	-0.63 ± 0.05	-0.78 ± 0.11	yes	no	no
NGC 6656	-1.70	-1.55 ± 0.07	-1.84 ± 0.13	yes	no	yes
NGC 6681	-1.62	-1.36 ± 0.07	-1.59 ± 0.17	yes	no	no
NGC 6752	-1.54	-1.42 ± 0.04	-1.63 ± 0.08	yes	no	yes
NGC 7078	-2.37	-2.17 ± 0.08	-2.44 ± 0.26	yes	no	no
NGC 7089	-1.65	-1.46 ± 0.06	-1.72 ± 0.26	yes	yes	no
NGC 7099	-2.27	-2.07 ± 0.04	-2.39 ± 0.16	yes	no	yes

Table B.6.: Same as Table B.1, but for the isochrone method and without SNR cut.

Cluster	Metallicity	RGB	MSTO	MS vis?	RGB inc?	MSTO sep?
NGC 104	-0.72	-0.72 ± 0.04	-0.82 ± 0.09	yes	no	no
NGC 1851	-1.18	-1.07 ± 0.05	-1.25 ± 0.15	yes	yes	no
NGC 1904	-1.60	-1.45 ± 0.07	-1.51 ± 0.19	yes	no	no
NGC 2808	-1.14	-1.03 ± 0.06	-1.24 ± 0.18	yes	yes	no
NGC 3201	-1.59	-1.3 ± 0.05	-1.5 ± 0.04	yes	yes	yes
NGC 362	-1.26	-1.1 ± 0.05	-1.33 ± 0.14	yes	yes	yes
NGC 5139	-1.53	-1.43 ± 0.09	-1.74 ± 0.15	yes	no	yes
NGC 5286	-1.69	-1.5 ± 0.05	-1.78 ± 0.25	yes	yes	no
NGC 5904	-1.29	-1.18 ± 0.04	-1.4 ± 0.11	yes	yes	yes
NGC 6093	-1.75	-1.52 ± 0.05	-1.78 ± 0.19	yes	no	yes
NGC 6121	-1.16	-0.93 ± 0.03	-1.13 ± 0.05	yes	yes	yes
NGC 6218	-1.37	-1.16 ± 0.05	-1.36 ± 0.04	yes	yes	yes
NGC 6254	-1.56	-1.41 ± 0.04	-1.6 ± 0.07	yes	yes	yes
NGC 6266	-1.18	-0.9 ± 0.06	-1.15 ± 0.12	yes	yes	yes
NGC 6293	-1.99	-1.95 ± 0.13	-2.46 ± 0.7	yes	no	no
NGC 6388	-0.55	-0.48 ± 0.08	-0.7 ± 0.16	yes	no	no
NGC 6441	-0.46	-0.46 ± 0.08	-0.6 ± 0.16	yes	no	no
NGC 6541	-1.81	-1.56 ± 0.03	-1.82 ± 0.17	yes	yes	yes
NGC 6624	-0.44	-0.62 ± 0.06	-0.77 ± 0.1	yes	no	no
NGC 6656	-1.70	-1.54 ± 0.05	-1.8 ± 0.09	yes	yes	yes
NGC 6681	-1.62	-1.35 ± 0.04	-1.55 ± 0.11	yes	yes	yes
NGC 6752	-1.54	-1.42 ± 0.03	-1.61 ± 0.08	yes	yes	yes
NGC 7078	-2.37	-2.16 ± 0.07	-2.4 ± 0.24	yes	no	no
NGC 7089	-1.65	-1.45 ± 0.04	-1.68 ± 0.23	yes	yes	no
NGC 7099	-2.27	-2.06 ± 0.04	-2.37 ± 0.15	yes	yes	yes

Table B.7.: Same as Table B.1, but for the fixed length method and without SNR cut.

Cluster	Metallicity	RGB	MSTO	MS vis?	RGB inc?	MSTO sep?
NGC 104	-0.72	-0.73 ± 0.04	-0.83 ± 0.09	yes	no	no
NGC 1851	-1.18	-1.07 ± 0.05	-1.26 ± 0.16	yes	yes	no
NGC 1904	-1.60	-1.44 ± 0.06	-1.57 ± 0.18	yes	yes	no
NGC 2808	-1.14	-1.04 ± 0.06	-1.25 ± 0.18	yes	yes	no
NGC 3201	-1.59	-1.3 ± 0.05	-1.5 ± 0.07	yes	yes	yes
NGC 362	-1.26	-1.1 ± 0.05	-1.34 ± 0.17	yes	yes	yes
NGC 5139	-1.53	-1.42 ± 0.09	-1.64 ± 0.18	yes	no	no
NGC 5286	-1.69	-1.5 ± 0.06	-1.76 ± 0.25	yes	no	no
NGC 5904	-1.29	-1.19 ± 0.04	-1.4 ± 0.12	yes	yes	yes
NGC 6093	-1.75	-1.52 ± 0.05	-1.78 ± 0.22	yes	no	no
NGC 6121	-1.16	-0.94 ± 0.04	-1.14 ± 0.05	yes	yes	yes
NGC 6218	-1.37	-1.16 ± 0.05	-1.36 ± 0.04	yes	yes	yes
NGC 6254	-1.56	-1.41 ± 0.04	-1.6 ± 0.07	yes	yes	yes
NGC 6266	-1.18	-0.91 ± 0.06	-1.14 ± 0.11	yes	yes	yes
NGC 6293	-1.99	-1.95 ± 0.11	-2.22 ± 0.43	no	no	no
NGC 6388	-0.55	-0.49 ± 0.08	-0.69 ± 0.16	yes	yes	no
NGC 6441	-0.46	-0.46 ± 0.07	-0.59 ± 0.16	yes	no	no
NGC 6541	-1.81	-1.55 ± 0.04	-1.83 ± 0.18	yes	no	yes
NGC 6624	-0.44	-0.62 ± 0.06	-0.77 ± 0.1	yes	no	no
NGC 6656	-1.70	-1.54 ± 0.06	-1.78 ± 0.12	yes	no	yes
NGC 6681	-1.62	-1.35 ± 0.04	-1.56 ± 0.13	yes	yes	yes
NGC 6752	-1.54	-1.41 ± 0.03	-1.62 ± 0.09	yes	no	yes
NGC 7078	-2.37	-2.17 ± 0.07	-2.41 ± 0.27	yes	no	no
NGC 7089	-1.65	-1.45 ± 0.04	-1.67 ± 0.25	yes	yes	no
NGC 7099	-2.27	-2.06 ± 0.03	-2.38 ± 0.16	yes	no	yes

Table B.8.: Same as Table B.1, but for the fixed size method and without SNR cut.

Cluster	Metallicity	RGB	MSTO	MS vis?	RGB inc?	MSTO sep?
NGC 104	-0.72	-0.73 ± 0.03	-0.86 ± 0.14	yes	no	no
NGC 1851	-1.18	-1.08 ± 0.05	-1.29 ± 0.17	yes	yes	no
NGC 1904	-1.60	-1.47 ± 0.05	-1.6 ± 0.18	yes	no	no
NGC 2808	-1.14	-1.05 ± 0.06	-1.31 ± 0.23	yes	yes	no
NGC 3201	-1.59	-	-1.5 ± 0.07	no	no	no
NGC 362	-1.26	-1.12 ± 0.06	-1.37 ± 0.17	yes	yes	yes
NGC 5139	-1.53	-1.42 ± 0.1	-1.7 ± 0.19	yes	no	no
NGC 5286	-1.69	-1.51 ± 0.08	-1.81 ± 0.29	yes	yes	no
NGC 5904	-1.29	-1.2 ± 0.04	-1.43 ± 0.13	yes	yes	yes
NGC 6093	-1.75	-1.53 ± 0.07	-1.82 ± 0.25	yes	no	no
NGC 6121	-1.16	-	-	no	no	no
NGC 6218	-1.37	-	-1.36 ± 0.05	no	no	no
NGC 6254	-1.56	-1.44 ± 0.04	-1.62 ± 0.07	yes	yes	yes
NGC 6266	-1.18	-0.94 ± 0.07	-1.17 ± 0.16	yes	no	yes
NGC 6293	-1.99	-1.94 ± 0.15	-2.13 ± 0.38	no	no	no
NGC 6388	-0.55	-0.5 ± 0.07	-0.74 ± 0.18	no	yes	no
NGC 6441	-0.46	-0.48 ± 0.07	-0.63 ± 0.16	no	no	no
NGC 6541	-1.81	-1.57 ± 0.04	-1.87 ± 0.21	yes	yes	yes
NGC 6624	-0.44	-0.64 ± 0.06	-0.78 ± 0.1	yes	no	no
NGC 6656	-1.70	-1.54 ± 0.08	-1.8 ± 0.13	yes	no	yes
NGC 6681	-1.62	-1.35 ± 0.06	-1.57 ± 0.13	yes	no	yes
NGC 6752	-1.54	-1.42 ± 0.05	-1.63 ± 0.09	yes	no	yes
NGC 7078	-2.37	-2.18 ± 0.1	-2.49 ± 0.26	yes	no	no
NGC 7089	-1.65	-1.45 ± 0.05	-1.78 ± 0.3	yes	yes	no
NGC 7099	-2.27	-2.06 ± 0.06	-2.39 ± 0.17	yes	no	yes

Bibliography

Académie des sciences (France). Histoire de l'Académie royale des sciences ... avec les mémoires de mathématique & de physique... tirez des registres de cette Académie. 1771.

Anderson, J.; Sarajedini, A.; Bedin, L. R.; et al. The Acs Survey of Globular Clusters. V. Generating a Comprehensive Star Catalog for each Cluster. *The Astronomical Journal*, 2008. 135(6):2055. doi:10.1088/0004-6256/135/6/2055.

Ashman, K. M. and Zepf, S. E. *Globular Cluster Systems*. Cambridge University Press, 2008. ISBN 978-0-521-08783-4. Google-Books-ID: sXwXfSH6g90C.

Bacon, R.; Accardo, M.; Adjali, L.; et al. The MUSE second-generation VLT instrument. volume 7735. Proceedings of the SPIE, 2010 page 773508. doi: 10.1117/12.856027.

Bastian, N. and Lardo, C. Multiple Stellar Populations in Globular Clusters. *Annual Review of Astronomy and Astrophysics*, 2018. 56:83–136. ISSN 0066-4146. doi: 10.1146/annurev-astro-081817-051839.

Bertelli Motta, C.; Pasquali, A.; Richer, J.; et al. The Gaia-ESO Survey: Evidence of atomic diffusion in M67? *Monthly Notices of the Royal Astronomical Society*, 2018. 478(1):425–438. ISSN 0035-8711, 1365-2966. doi:10.1093/mnras/sty1011. ArXiv: 1804.06293.

Boesgaard, A. M.; Deliyannis, C. P.; Stephens, A.; et al. Primordial Lithium: Keck Observations in M92 Turnoff Stars. *The Astrophysical Journal*, 1998. 493:206–216. ISSN 0004-637X. doi:10.1086/305089.

Carroll, B. W. and Ostlie, D. A. *Introduction to modern astrophysics*. Cambridge University Press, Cambridge, 2nd edition edition, 2014.

Chapman, S. Thermal Diffusion and the Stars. *Monthly Notices of the Royal Astronomical Society*, 1917. 77(7):539–540. ISSN 0035-8711. doi:10.1093/mnras/77.7.539.

Choi, J.; Dotter, A.; Conroy, C.; et al. Mesa Isochrones and Stellar Tracks (MIST). I. Solar-scaled Models. *The Astrophysical Journal*, 2016. 823:102. ISSN 0004-637X. doi:10.3847/0004-637X/823/2/102.

Dotter, A. MESA Isochrones and Stellar Tracks (MIST) 0: Methods for the Construction of Stellar Isochrones. *The Astrophysical Journal Supplement Series*, 2016. 222:8. ISSN 0067-0049. doi:10.3847/0067-0049/222/1/8.

Dotter, A.; Conroy, C.; Cargile, P.; et al. The Influence of Atomic Diffusion on Stellar Ages and Chemical Tagging. *The Astrophysical Journal*, 2017. 840:99. ISSN 0004-637X. doi:10.3847/1538-4357/aa6d10.

Eisenhauer, F. and Raab, W. Visible/Infrared Imaging Spectroscopy and Energy-Resolving Detectors. *Annual Review of Astronomy and Astrophysics*, 2015. 53(1):155–197. ISSN 0066-4146. doi:10.1146/annurev-astro-082214-122442.

Fitzpatrick, E. L. Correcting for the Effects of Interstellar Extinction. *Publications of the Astronomical Society of the Pacific*, 1999. 111:63–75. ISSN 0004-6280. doi:10.1086/316293.

Fontana, A.; Dunlop, J. S.; Paris, D.; et al. The Hawk-I UDS and GOODS Survey (HUGS): Survey design and deep K-band number counts. *Astronomy and Astrophysics*, 2014. 570:A11. ISSN 0004-6361. doi:10.1051/0004-6361/201423543.

Freeman, K. C. and Norris, J. The chemical composition, structure, and dynamics of globular clusters. *Annual Review of Astronomy and Astrophysics*, 1981. 19:319. doi:10.1146/annurev.aa.19.090181.001535.

Gao, X.; Lind, K.; Amarsi, A. M.; et al. The GALAH survey: verifying abundance trends in the open cluster M67 using non-LTE modelling. *Monthly Notices of the Royal Astronomical Society*, 2018. 481(2):2666–2684. ISSN 0035-8711. doi:10.1093/mnras/sty2414.

Giesers, B.; Dreizler, S.; Husser, T.-O.; et al. A detached stellar-mass black hole candidate in the globular cluster NGC 3201. *Monthly Notices of the Royal Astronomical Society*, 2018. 475:L15–L19. ISSN 0035-8711. doi:10.1093/mnrasl/slx203.

Gratton, R.; Sneden, C.; and Carretta, E. Abundance Variations Within Globular Clusters. *Annual Review of Astronomy and Astrophysics*, 2004. 42(1):385. doi: 10.1146/annurev.astro.42.053102.133945.

Gratton, R. G.; Carretta, E.; and Bragaglia, A. Multiple populations in globular clusters. *The Astronomy and Astrophysics Review*, 2012. 20(1):50. ISSN 1432-0754. doi:10.1007/s00159-012-0050-3.

Gruyters, P.; Korn, A. J.; Richard, O.; et al. Atomic diffusion and mixing in old stars - IV. Weak abundance trends in the globular cluster NGC 6752. *Astronomy & Astrophysics*, 2013. 555:A31. ISSN 0004-6361, 1432-0746. doi:10.1051/0004-6361/201220821.

Gruyters, P.; Nordlander, T.; and Korn, A. J. Atomic diffusion and mixing in old stars. V. A deeper look into the globular cluster NGC 6752. *Astronomy and Astrophysics*, 2014. 567:A72. ISSN 0004-6361. doi:10.1051/0004-6361/201423590.

Gruyters, P.; Lind, K.; Richard, O.; et al. Atomic diffusion and mixing in old stars. VI. The lithium content of M30. *Astronomy and Astrophysics*, 2016. 589:A61. doi:10.1051/0004-6361/201527948.

Göttgens, F. *Analysis of the relation between spectral type and metallicty in NGC 3201 using MUSE data.* Bachelor Thesis, University of Göttingen, Göttingen, 2015.

Göttgens, F.; Weilbacher, P. M.; Roth, M. M.; et al. Discovery of an old nova remnant in the Galactic globular cluster M 22. *Astronomy & Astrophysics*, 2019. 626:A69. ISSN 0004-6361, 1432-0746. doi:10.1051/0004-6361/201935221.

Harris, W. E. A New Catalog of Globular Clusters in the Milky Way. *arXiv e-prints*, 2010. 1012:arXiv:1012.3224.

Herschel, W. Catalogue of a Second Thousand of New Nebulae and Clusters of Stars; With a Few Introductory Remarks on the Construction of the Heavens. By William Herschel, L L. D. F. R. S. *Philosophical Transactions of the Royal Society of London Series I*, 1789. 79:212–255.

Husser, T.-O. *3D-spectroscopy of dense stellar populations.* Univ.-Verl., Göttingen, 2012. ISBN 978-3-86395-092-7.

Husser, T.-O.; Kamann, S.; Dreizler, S.; et al. A new extensive library of synthetic stellar spectra from PHOENIX atmospheres and its application to fitting VLT MUSE spectra. volume 6. eprint: arXiv:1203.1941, 2012 page 71.

Husser, T.-O.; Kamann, S.; Dreizler, S.; et al. MUSE crowded field 3d spectroscopy of over 12 000 stars in the globular cluster NGC 6397. I. The first comprehensive HRD of a globular cluster. *Astronomy and Astrophysics*, 2016. 588:A148. ISSN 0004-6361. doi:10.1051/0004-6361/201526949.

Kamann, S.; Wisotzki, L.; and Roth, M. M. Resolving stellar populations with crowded field 3d spectroscopy. *Astronomy and Astrophysics*, 2013. 549:A71. ISSN 0004-6361. doi:10.1051/0004-6361/201220476.

Kamann, S.; Husser, T.-O.; Dreizler, S.; et al. A stellar census in globular clusters with MUSE: The contribution of rotation to cluster dynamics studied with 200 000 stars. *Monthly Notices of the Royal Astronomical Society*, 2018. 473:5591–5616. ISSN 0035-8711. doi:10.1093/mnras/stx2719.

King, J. R.; Stephens, A.; Boesgaard, A. M.; et al. Keck HIRES spectroscopy of M92 subgiants - Surprising abundances near the turnoff. *The Astronomical Journal*, 1998. 115:666. ISSN 0004-6256. doi:10.1086/300209.

Kippenhahn, R. *Stellar Structure and Evolution*. Astronomy and Astrophysics Library. Springer, Berlin, 2nd ed. 2013. edition, 2013. ISBN 978-3-642-30304-3.

Korn, A. J.; Grundahl, F.; Richard, O.; et al. Atomic Diffusion and Mixing in Old Stars. I. Very Large Telescope FLAMES-UVES Observations of Stars in NGC 6397. *The Astrophysical Journal*, 2007. 671:402–419. ISSN 0004-637X. doi: 10.1086/523098.

Lind, K.; Korn, A. J.; Barklem, P. S.; et al. Atomic diffusion and mixing in old stars. II. Observations of stars in the globular cluster NGC 6397 with VLT/FLAMES-GIRAFFE. *Astronomy and Astrophysics*, 2008. 490:777–786. ISSN 0004-6361. doi:10.1051/0004-6361:200810051.

MacKay, D. J. C. An Example Inference Task: Clustering. In *Information Theory, Inference and Learning Algorithms*. Cambridge University Press. ISBN 978-0-521-64298-9, 2003. Http://www.inference.org.uk/mackay/itprnn/ps/284.292.pdf.

Michaud, G.; Alecian, G.; and Richer, J. *Atomic diffusion in stars*. Astronomy and astrophysics library. Springer, Cham, 2015. ISBN 978-3-319-19853-8.

Mucciarelli, A.; Salaris, M.; Lovisi, L.; et al. Lithium abundance in the globular cluster M4: from the turn-off to the red giant branch bump. *Monthly Notices of the Royal Astronomical Society*, 2011. 412:81–94. ISSN 0035-8711. doi:10.1111/j.1365-2966.2010.17884.x.

Nordlander, T.; Korn, A. J.; Richard, O.; et al. Atomic Diffusion and Mixing in Old Stars. III. Analysis of NGC 6397 Stars under New Constraints. *The Astrophysical Journal*, 2012. 753:48. ISSN 0004-637X. doi:10.1088/0004-637X/753/1/48.

Paxton, B.; Bildsten, L.; Dotter, A.; et al. Modules for Experiments in Stellar Astrophysics (MESA). *The Astrophysical Journal Supplement Series*, 2011. 192:3. ISSN 0067-0049. doi:10.1088/0067-0049/192/1/3.

Paxton, B.; Cantiello, M.; Arras, P.; et al. Modules for Experiments in Stellar Astrophysics (MESA): Planets, Oscillations, Rotation, and Massive Stars. *The Astrophysical Journal Supplement Series*, 2013. 208:4. ISSN 0067-0049. doi:10.1088/0067-0049/208/1/4.

Paxton, B.; Marchant, P.; Schwab, J.; et al. Modules for Experiments in Stellar Astrophysics (MESA): Binaries, Pulsations, and Explosions. *The Astrophysical Journal Supplement Series*, 2015. 220:15. ISSN 0067-0049. doi:10.1088/0067-0049/220/1/15.

Paxton, B.; Schwab, J.; Bauer, E. B.; et al. Modules for Experiments in Stellar Astrophysics (MESA): Convective Boundaries, Element Diffusion, and Massive Star Explosions. *The Astrophysical Journal Supplement Series*, 2018. 234:34. ISSN 0067-0049. doi:10.3847/1538-4365/aaa5a8.

Reiners, A. and Basri, G. On the magnetic topology of partially and fully convective stars. *Astronomy and Astrophysics*, 2009. 496:787–790. ISSN 0004-6361. doi:10.1051/0004-6361:200811450.

Richard, J.; Bacon, R.; Blaizot, J.; et al. BlueMUSE: Project Overview and Science Cases. *arXiv:1906.01657 [astro-ph]*, 2019. ArXiv: 1906.01657.

Salaris, M. and Cassisi, S. Chemical element transport in stellar evolution models. *Royal Society Open Science*, 2017. 4(8):170192. doi:10.1098/rsos.170192.

Sandage, A. R. The color-magnitude diagram for the globular cluster M 3. *The Astronomical Journal*, 1953. 58:61–75. ISSN 0004-6256. doi:10.1086/106822.

Schultz, H. Historische Notizen über Nebelflecke. Von Herrn Dr. Hermann Schultz. *Astronomische Nachrichten*, 1866. 67:1. ISSN 0004-6337. doi:10.1002/asna.18660670102.

Shapley, H. Globular Clusters and the Structure of the Galactic System. *Publications of the Astronomical Society of the Pacific*, 1918. 30:42. ISSN 0004-6280. doi:10.1086/122686.

Souto, D.; Cunha, K.; Smith, V. V.; et al. Chemical Abundances of Main-sequence, Turnoff, Subgiant, and Red Giant Stars from APOGEE Spectra. I. Signatures of Diffusion in the Open Cluster M67. *The Astrophysical Journal*, 2018. 857:14. ISSN 0004-637X. doi:10.3847/1538-4357/aab612.

Stryker, L. L. Blue stragglers. *Publications of the Astronomical Society of the Pacific*, 1993. 105:1081–1100. ISSN 0004-6280. doi:10.1086/133286.

Tutukov, A. V. Binarity and Abundance Anomalies in Stars. *Symposium - International Astronomical Union*, 1991. 145:351–362. ISSN 0074-1809. doi:10.1017/S0074180900227496.

Weilbacher, P. M.; Streicher, O.; Urrutia, T.; et al. Design and capabilities of the MUSE data reduction software and pipeline. volume 8451. 2012 page 84510B. doi:10.1117/12.925114.

Acknowledgements

I wish to thank Prof. Dr. Stefan Dreizler for giving me the opportunity to work on this exciting project and for being the best professor one could possibly imagine. I thank Dr. Tim-Oliver Husser, Fabian Göttgens Benjamin Giesers and Dr. Marilyn Latour for their helpful comments and remarks throughout the time of working on this thesis and for them patiently proofreading at least parts of it. Special thanks go out to my office mate Fabian as he had to bear my – sometimes a little bit stupid – questions for the most of the time. I also want to thank Dr. Frederic V. Hessman for him agreeing to be second referee to my thesis.

Erklärung nach §12(9) der Prüfungs- und Studienordnung für den konsekutiven Master-Studiengang „Physics“ der Georg-August-Universität Göttingen:

Hiermit erkläre ich, dass ich diese Abschlussarbeit selbständig verfasst habe, keine anderen als die angegebenen Quellen und Hilfsmittel benutzt habe und alle Stellen, die wörtlich oder sinngemäß aus veröffentlichten Schriften entnommen wurden, als solche kenntlich gemacht habe.
Darüberhinaus erkläre ich, dass diese Abschlussarbeit nicht, auch nicht auszugsweise, im Rahmen einer nichtbestandenen Prüfung an dieser oder einer anderen Hochschule eingereicht wurde.

Göttingen, den 09. August 2019

(Merten Nikolay Dahlkemper)